

Optimization of signal and background separation for di-Higgs production search in the $b\bar{b}\tau^+\tau^-$ channel



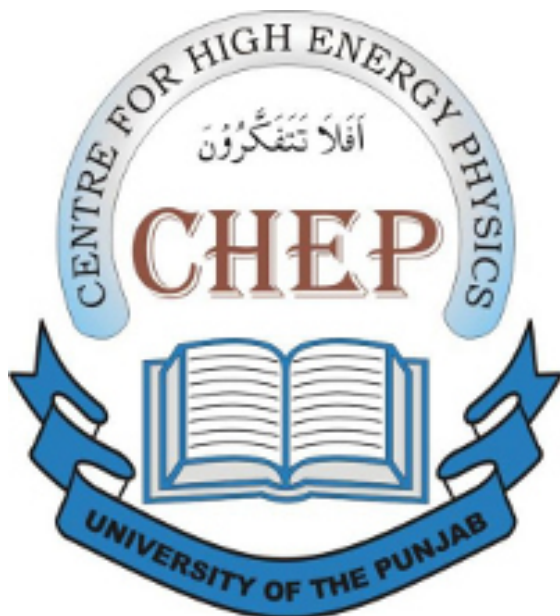
Submitted By
MUHAMMAD FAROOQ
ROLL No. M.PHIL-HEP20F18
SESSION 2018-2020

SUPERVISORS
DR. TALAB HUSSAIN
DR. ASHFAQ AHMAD

CENTRE FOR HIGH ENERGY PHYSICS
UNIVERSITY OF THE PUNJAB
LAHORE-PAKISTAN

*Optimization of signal and background
separation for di-Higgs production search in
the $b\bar{b}\tau^+\tau^-$ channel*

Author:
MUHAMMAD FAROOQ



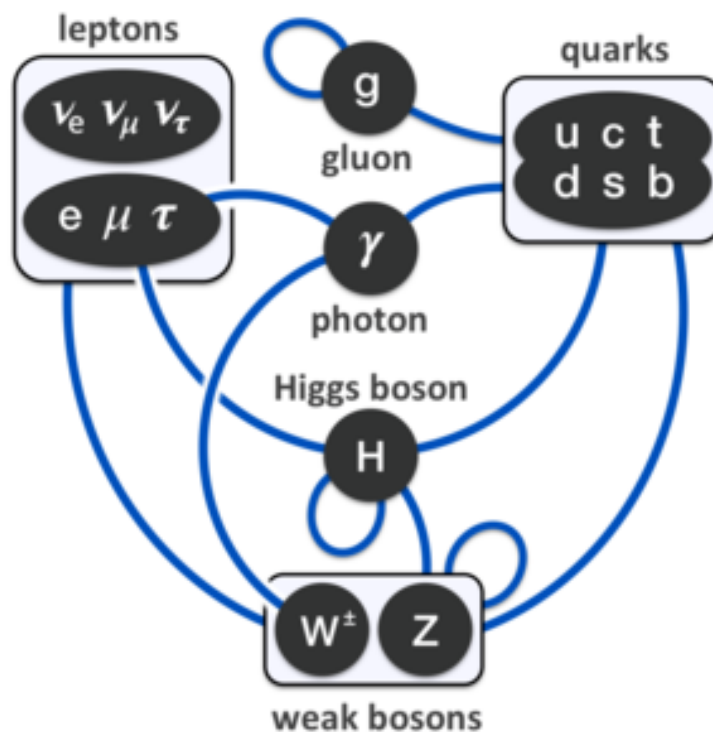
*"A DISSERTATION SUBMITTED IN THE PARTIAL
FULFILLMENT OF THE REQUIREMENT FOR THE DEGREE
OF MASTER OF PHILOSOPHY"*

Center For High Energy Physics
University Of The Punjab, Lahore, Pakistan

(2018-2020)

*Optimization of signal and background
separation for di-Higgs production search in
the $b\bar{b}\tau^+\tau^-$ channel*

BY
MUHAMMAD FAROOQ



Centre For High Energy Physics,
University Of The Punjab, Lahore, Pakistan

(2018-2020)

List of Figures

2.1	Fundamental particles of the Standard Model [4]	6
2.2	Higgs Potential [5]	9
2.3	Main Leading Order (LO) Feynman diagrams contributing to the Higgs production in (a) gluon-gluon fusion (ggF), (b) vector-boson fusion (VBF), (c) Higgs-strahlung (or associated production with a gauge boson, VH), (d) associated production with a pair of top quarks (ttH)	13
2.4	Standard Model Higgs boson decay branching ratios as a function of the Higgs mass m_H [14].	14
2.5	Standard Model Higgs boson decay branching ratios as a function of the Higgs mass m_H	14
3.1	The Layout for LHC and CERN accelerator as injector chain for the LHC [16]	18
3.2	In Run 2, Integrated Luminosity delivered by the LHC and recorded by ATLAS experiment [23]	19
3.3	LHC operation schedule [24].	20
3.4	ATLAS detector with sub-systmes are labelled [26]	21
3.5	ATLAS detector coordinate system [17]	21
3.6	ATLAS magnet system (layout).	23
3.7	(a) ATLAS Inner detector (layout). (b) A zoomed view of inner detector [30].	23
3.8	ATLAS calorimeter system [32].	25
3.9	ATLAS muon-spectrometer [33].	26
3.10	ATLAS trigger and DAQ system [34].	27
4.1	(a) τ -jets and (b) b-jets	31
4.2	(a) Signal and (b) Background	31
5.1	(Left) Flow-chart of TMVA training application & (Right) Flowchart of TMVA analysis application [39].	34
5.2	BDT apply different cuts on each branch with “S” is signal and “B” is background [39].	34
5.3	(a) Significance of 1_var and (b) Significance of 2_vars	35
5.4	(a) Significance of 3_vars and (b) Significance of 4_vars	36
5.5	(a) Significance of 5_vars and (b) Significance of 6_vars	36
5.6	(a) Significance of 15_vars and (b) Significance of all vars up-to 15_vars	37
5.7	(a) MC-Input Variables (2016) and (b) DATA-Input Variables (2016)	38

5.8 (a) MC-Input Variables (2016) and (b) DATA-Input Variables (2016)	39
5.9 (a) MC-Input Variables (2016) and (b) DATA-Input Variables (2016)	40
5.10 (a) Correlation matrix MC (2016) and (b) Correlation matrix DATA (2016)	40
5.11 (a) MC Classifier (2016) and (b) DATA Classifier (2016)	41
5.12 (a) ROC curve (2016) and (b) ROC curve (2016)	41
5.13 (a) MC-Input Variables (2017) and (b) DATA-Input Variables (2017)	42
5.14 (a) MC-Input Variables (2017) and (b) DATA-Input Variables (2017)	43
5.15 (a) Correlation matrix MC and (b) Correlation matrix DATA . . .	44
5.16 (a) MC Classifier (2017) and (b) DATA Classifier (2017)	44
5.17 (a) ROC curve (2017) and (b) ROC curve (2017)	45
5.18 (a) MC-Input Variables (2018) and (b) DATA-Input Variables (2018)	45
5.19 (a) MC-Input Variables (2018) and (b) DATA-Input Variables (2018)	46
5.20 (a) MC-Input Variables (2018) and (b) DATA-Input Variables (2018)	47
5.21 (a) Correlation matrix MC and (b) Correlation matrix DATA . . .	47
5.22 (a) Correlation matrix MC and (b) Correlation matrix DATA . . .	48
5.23 (a) MC Classifier (2017) and (b) DATA Classifier (2017)	48
5.24 (a) ROC curve (2017) and (b) ROC curve (2017)	48
5.25 (a) MC-Input Variables (2016-17) and (b) DATA-Input Variables (2016-17)	49
5.26 (a) MC-Input Variables (2016-17) and (b) DATA-Input Variables (2016-17)	50
5.27 (a) Correlation matrix MC (2016-17) and (b) Correlation matrix DATA (2016-17)	51
5.28 (a) MC Classifier (2016-17) and (b) DATA Classifier (2016-17) . .	51
5.29 (a) ROC curve (2016-17) and (b) ROC curve (2016-17)	52
5.30 (a) MC-Input Variables (2016-18) and (b) DATA-Input Variables (2016-18)	52
5.31 (a) MC-Input Variables (2016-18) and (b) DATA-Input Variables (2016-18)	53
5.32 (a) MC-Input Variables (2016-18) and (b) DATA-Input Variables (2016-18)	54
5.33 (a) Correlation matrix MC (2016-18) and (b) Correlation matrix DATA (2016-18)	54
5.34 (a) Correlation matrix MC (2016-18) and (b) Correlation matrix DATA (2016-18)	55
5.35 (a) MC Classifier (2016-18) and (b) DATA Classifier (2016-18) . .	55
5.36 (a) ROC curve (2016-18) and (b) ROC curve (2016-18)	55
5.37 (a) MC-Input Variables (2017-18) and (b) DATA-Input Variables (2017-18)	56
5.38 (a) MC-Input Variables (2017-18) and (b) DATA-Input Variables (2017-18)	57
5.39 (a) Correlation matrix MC (2017-18) and (b) Correlation matrix DATA (2017-18)	58
5.40 (a) MC Classifier (2017-18) and (b) DATA Classifier (2017-18) . .	58
5.41 (a) ROC curve (2017-18) and (b) ROC curve (2017-18)	59

5.42 (a) MC-Input Variables (2016-17-18) and (b) DATA-Input Variables (2016-17-18)	59
5.43 (a) MC-Input Variables (2016-17-18) and (b) DATA-Input Variables (2016-17-18)	60
5.44 (a) MC-Input Variables (2016-17-18) and (b) DATA-Input Variables (2016-17-18)	61
5.45 (a) Correlation matrix MC (2016-17-18) and (b) Correlation matrix DATA (2016-17-18)	61
5.46 (a) Correlation matrix MC (2016-17-18) and (b) Correlation matrix DATA (2016-17-18)	62
5.47 (a) MC Classifier (2016-17-18) and (b) DATA Classifier (2016-17-18)	62
5.48 (a) ROC curve (2016-17-18) and (b) ROC curve (2016-17-18)	62
5.49 Data and MC comparison	63
5.50 Ratio-Difference b/w Data & MC	63
5.51 Integrated Luminosity	64
6.1	65
6.2	66
6.4	67
6.5 This table shows about the samples, entries, yield and error for the plots	67

List of Tables

2.1	Higgs boson decay branching ratios for $m_H = 125.09\text{GeV}$ [15]	12
2.2	Di-Higgs boson decay branching ratios for $m_H = 125.09\text{GeV}$	13
3.1	Performance goals of ATLAS detector. Units of p_T and E are GeV .	22
4.1	τ_{lep} decay modes [36].	30
4.2	τ_{had} decay modes [36].	30
5.1	Yearly based Integrated Luminosity.	37
5.2	Sensitivity for old variables.	38
5.3	Sensitivity for MC-variables.	38
5.4	Sensitivity for DATA-variables.	38

Contents

1	Introduction	3
2	The Standard Model and the Higgs boson	4
2.1	Basic concepts	4
2.2	The SM gauge theory	5
2.2.1	Quantum electrodynamics (QED)	6
2.2.2	Quantum Chromodynamics (QCD)	7
2.2.3	Electroweak theory	7
2.2.4	Brout-Englert-Higgs mechanism	8
2.2.5	Yukawa coupling and fermion masses	11
2.3	The Higgs boson and Higgs pair production	12
2.3.1	Higgs production and decay	12
2.3.2	Higgs pair production and decay	13
3	The ATLAS experiment at LHC	16
3.1	The Large Hadron Collider	16
3.1.1	Machine design	17
3.1.2	The LHC operation schedule	18
3.2	The ATLAS detector	19
3.2.1	Coordinate system	20
3.2.2	Magnets	22
3.2.3	Inner detector	22
3.3	Calorimeter system	24
3.3.1	Muon spectrometer	26
3.3.2	Trigger system	27
4	Decays of di-Higgs boson to $b\bar{b}\tau_{lep}\tau_{had}$	28
4.1	$b\bar{b}\tau_{had}\tau_{had}$	28
4.2	$b\bar{b}\tau_{lep}\tau_{had}$	28
4.2.1	Combination 1	29
4.2.2	Combination 2	29
4.3	Object reconstruction in the ATLAS detector	29
4.3.1	Bottom-quark	29
4.3.2	b-tagging	29
4.3.3	tau-lepton	29
4.3.4	Missing transverse energy	29
4.4	Monte Carlo and Data Samples	30

4.5	Event Selection	30
5	Multivariate Analysis in HEP	32
5.1	Multivariate Technique	32
5.1.1	Training phase	32
5.1.2	Application phase	33
5.2	Boosted Decision Trees	33
5.3	Input variables	35
5.3.1	BDT training for $b\bar{b}\tau_{lep}\tau_{had}$ channel	35
5.4	Comparison with MC and DATA Samples	36
5.4.1	Period 2016	37
5.4.2	Period 2017	41
5.4.3	Period 2018	45
5.4.4	Period 2016-17	49
5.4.5	Period 2016-18	52
5.4.6	Period 2017-18	56
5.4.7	Period 2016-17-18	59
5.5	Data and MC Comparison	63
6	Appendix $hh \rightarrow b\bar{b}\tau^+\tau^-$	65
7	Conclusion	68

Acknowledgments

I take this opportunity to thank everyone who has contributed directly or indirectly to the production of this work. I express my deep gratitude to my supervisor and my true inspiration to the field, Dr. Ashfaq Ahmad. My special thanks to Prof. Song-Ming Wang about my research project with ATLAS collaboration. Both have been the best mentor I could ever hope for. Not only is his scientific genius remarkable but his overall knowledge and understanding of things always impress me to the maximum. I also want to thank Mr. Shahzad Ali for his constant and detailed support and help throughout this work.

I am also thankful to my parent university faculty like Dr. Bilal Masud, Dr. Faisal Akram and my supervisor Dr. Talab Hussain.

I would like to express my deepest regard to my loving mother, late father, brothers and sister for their emotional and moral support throughout my academic career and also for their love, encouragement and prayers.

I want to thank my group fellows Sajid, Hammad, Rabiya, Saba, Jamshid, Shaheryar, and Umar Farooq. for their contribution to friendly and pleasant working environment.

Muhammad Farooq

CERTIFICATE

The undersigned hereby certify that the work in this thesis entitled "*Optimization of signal and background separation for di-Higgs production search in the $b\bar{b}\tau^+\tau^-$ channel*" has been done by **Mr. Muhammad Farooq**, Roll No. M.PHIL-HEP20F18 Session 2018-2020, during his enrollment of M.Phil (High Energy Physics) in Center for High Energy Physics under my supervision at National Centre for Physics.

Dr. Ashfaq Ahmad
Supervisor
Director of Experimental
High Energy Physics
National Centre for
Physics
Quaid-e-Azam University,
Islamabad, Pakistan

Dr. Talab Hussain
Supervisor
Assistant Professor
Centre for High Energy
Physics,
University of the Punjab,
Quaid-e-Azam Campus,
Lahore, Pakistan

Dr. Bilal Masud

Director of Centre for
High Energy Physics,
University of the Punjab,
Quaid-e-Azam Campus,
Lahore, Pakistan

DECLARATION

I, Muhammad Farooq, the undersigned, hereby certify that this work in this thesis entitled "*Optimization of signal and background separation for di-Higgs production search in the $b\bar{b}\tau^+\tau^-$ channel*" has been done by me, and all that the sources I have used quoted have been indicated or acknowledged by means of complete references.

Signature of Author

Abstract

This thesis explores the most dominant di-Higgs production mode gluon-gluon Fusion (ggF) in the decay channel of the $hh \rightarrow b\bar{b}\tau^+\tau^-$. $b\bar{b}\tau^+\tau^-$ is one of the most promising channel having relatively large branching fraction (7.3%) and less multi-jet background compare to 4b channel. In this thesis the sub-channel $hh \rightarrow b\bar{b}\tau_{lep}\tau_{had}$ (where one of the tau decays hadronically and other decay leptonically) is investigated for the optimization of signal and background kinematics. The background sample that is chosen for the optimisation is ttbar which is the major background for the $b\bar{b}\tau_{lep}\tau_{had}$. The optimisation is performed through multivariate analysis by using BDT algorithm. Start training with using mhh, one of the most discriminating variable, as the first variable perform separate training by adding a second variable and evaluate the significance and pick the variable that gives the highest significance. Repeat the procedure to select the 3rd, 4th, ... variables. We stop the training when we do not observe significant improve by adding more variables. The significance is obtained by transforming BDT output distributions and compute the log-likelihood ratio (LLR) based on the transformed bins. After getting the optimized variables applied on MC and Data samples which gives us better results. The final results are agreement between the MC and Data samples which shows approximately same behaviour.

Chapter 1

Introduction

The standard model (SM) theory capture our best understanding of the fundamental particles and their interactions. It's developed in the 1970s, it's a compatible theory which confirms huge success to provide experimental predictions which have been validated by experimental observations over time. The discovery of a new particle whose properties consistent with the SM Higgs-boson by the ATLAS and CMS experiment at large hadron collider (LHC) in 2012 was a break-through for the experimental tests of the SM. Now, the Higgs-boson coupling measurements are very important to test the validity of Brout-Englert-Higgs (BEH) mechanism, electroweak theory and the SM theory, all these couplings predicted by SM theory, given the measured values of the masses of particles and vacuum expectation value. The triple Higgs self-coupling, λ_{HHH} present in the SM and it's value corresponds to this $m_H^2/2v$ controls the shape of Higgs potential. To measure these couplings we have to look for a Higgs-boson pair production process. In SM, the Higgs-boson pairs can be produced at LHC via the gluon-gluon-fusion (ggF) at a centre-of-mass energy of 13TeV with the cross-section of 33.41 fb. Gluon-gluon-fusion includes the top-quark loops and triple Higgs self-interaction λ_{HHH} . The observation of this process and Higgs self-couplings are challenging due to its small cross-section and its central goal for the high luminosity (HL-LHC).

This thesis work presents a search for the SM di-Higgs pair-production in the $b\bar{b}\tau_{lep}^+\tau_{had}^-$ final state. Exploring the di-Higgs decay channel where one of the Higgs-boson decays to b-quark pairs and other Higgs-boson decays to a pair of tau-lepton with one lepton decays leptonically and other higgs-boson decays hadronically. The search is performed using the MC and Data samples collected by the ATLAS detector for periods of 2016,2017 and 2018 with the integrated luminosity of $137fb^{-1}$.

The thesis is structured below. Chapter 1 gives description about standard model including Brout-Englert-Higgs mechanism, Higgs-boson discovery, di-Higgs production and decay channels. Chapter 3 describes detailed view about LHC and ATLAS detector. Chapter 4 describes about decays of di-Higgs boson to $b\bar{b}\tau_{lep}^+\tau_{had}^-$, it's branching ratios, object reconstruction at ATLAS, Monte-Carlo samples, and Event Selection. Chapter 5 discuss about Multivariate analysis in HEP which includes MVA technique, Boosted-decision trees (BDTs) and input variables. Chapter 6 describes final summary of the analysis and discussion on results.

Chapter 2

The Standard Model and the Higgs boson

The Standard Model (SM) [1] of the particle physics that describes the fundamental structure of the matter: everything in the universe is found to be made from some fundamental building blocks say fundamental particles, governed by four fundamental forces. Our best understanding of three of the four fundamental forces (electromagnetic, weak, and strong forces) in the universe and also about the elementary particles are encapsulated in the SM theory of particle physics. Developed early in the 1970s, and over time through many experiments, it becomes well established as well as well tested physics theory that explains almost all experimental results. One of the huge successes of SM is discovery of the Higgs-boson in 2012 [2, 3], addressed by the ATLAS and CMS experiments at Large hadron Collider (LHC), whose properties compatible with SM Higgs-boson.

This chapter introduces the introduction to basic concept of SM gauge theory, Quantum Electrodynamics (QED), Quantum Chromodynamics (QCD), Electroweak theory, Yukawa Coupling, Brout-Englert-Higgs mechanism, and one of the most topic about the Higgs-boson decay and its couplings.

2.1 Basic concepts

Basic building blocks of matter are categorized into two types “quarks” and “leptons”, each type consist of 6-particles which are organized into three generations having the same properties except their mass. First-generation form the “up-quark” and “down-quark”, second-generation form the “charm-quark” and “strange-quark”, and third-generation form the “top-quark” and “bottom-quark”. The up-types quarks carry the $+2/3$ electric charge and down-type quarks carry the $-1/3$ electric charge and also with colour charge (R, G, B). Similarly for leptons, first-generation form the “electron” and “electron neutrino”, second-generation form the “muon” and “muon neutrino”, and the third-generation form the “tau” and “tau-neutrino”. The electron, muon, and tau carry the -1 electric charge and their corresponding neutrinos are electrically neutral. Quarks and leptons are fermions with spin $1/2$. Also, there are corresponding anti-particles with the same properties mass, spin, lifetime but differ with an electric charge.

The EM force acts between the electrically charged particles. The weak interaction is involved in β -decay, absorption, and emission of neutrinos and ~ 1000 times weaker than the EM force. The strong interaction is responsible to hold the nuclei and acts between coloured particles, and 100 times stronger than the EM force. The Gravitational force acts between all types of massive particles and its 10^{38} times weaker than the EM force. Each fundamental force has its force-carrier bosons with spin 1: electromagnetic force carried by photon γ , the weak force carried by W^\pm and Z bosons, and the strong force is carried by gluon.

There is one additional candidate of the SM say Higgs-boson with spin 0, which is responsible for giving the mass to fermions and force-carrier bosons. Figure 2.1

2.2 The SM gauge theory

The SM is a relativistic quantum field theory, where particles are described with excitation of quantum fields, and interactions are related to the local gauge symmetries of the Lagrangian. Its a gauge theory based on the symmetry:

$$SU(3) \otimes SU(2) \otimes U(1), \quad (2.1)$$

where $SU(3)$ is the symmetry group of strong interaction and $SU(2) \otimes U(1)$ is the symmetry group of the electroweak interactions.

Matter particles are described by fermionic field with spin 1/2 and the gauge-bosons by bosonic field with spin 1. The dynamics of system is described by the action in terms of the Lagrangian density $\mathcal{L}(x)$ which contains the field $\Phi(x)$, which accounts for their propagation, symmetries and account for their interactions:

$$S = \int d^4x \mathcal{L}(x) \quad (2.2)$$

For the evolution of system action should be stationary:

$$\delta S = \delta \int d^4x \mathcal{L}(\Phi(x), \partial_\mu \Phi(x)) = 0, \quad (2.3)$$

Euler-Lagrange equation correspond to equation of the motion of system:

$$\partial_\mu \left(\frac{\partial \mathcal{L}}{\partial (\partial_\mu \Phi)} \right) - \frac{\partial \mathcal{L}}{\partial \Phi} = 0. \quad (2.4)$$

A gauge symmetry is any continuous transformation of the field

$$\Phi(x) \rightarrow \Phi'(x) = \Phi(x) + \delta\Phi \quad (2.5)$$

According to Noether's theorem, corresponding to any continuous symmetry of the Lagrangian there is a conservation law:

$$\partial_\mu \frac{\partial \mathcal{L}}{\partial (\partial_\mu \Phi)} \delta\Phi = \partial_\mu J^\mu = 0, \quad (2.6)$$

where J^μ is the conserved current and

$$Q = \int dx J^0 = \text{constant} \quad (2.7)$$

is the conserved charge associated to the symmetry.

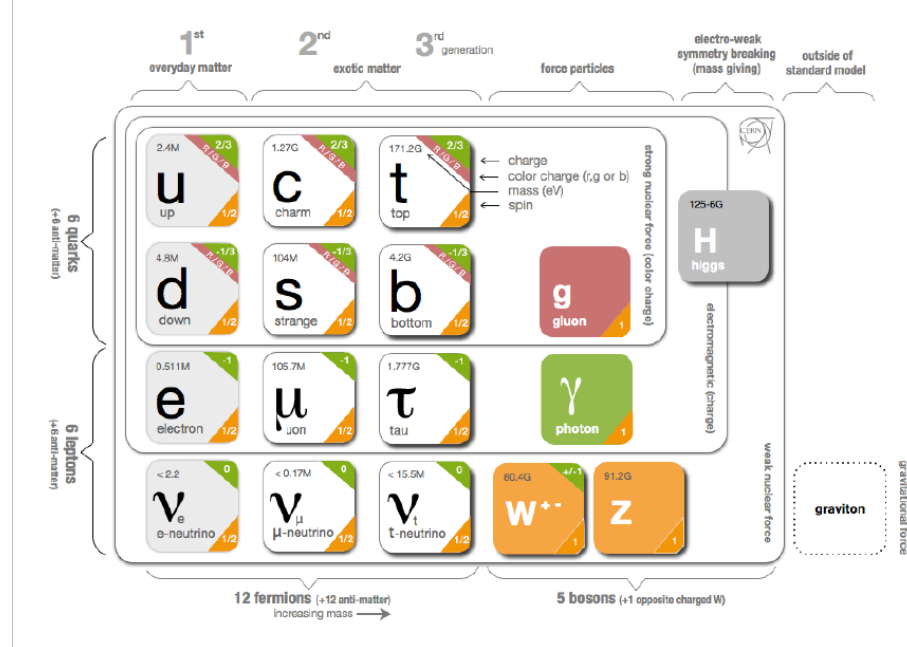


Figure 2.1: Fundamental particles of the Standard Model [4].

2.2.1 Quantum electrodynamics (QED)

QED is an abelian gauge theory which describes dynamics of interactions of the fermions with electromagnetic field.

The \mathcal{L} of a free massive fermion is given by:

$$\mathcal{L}_{Dirac}(x) = \bar{\psi}(x)(i\gamma^\mu\partial_\mu - m)\psi(x), \quad (2.8)$$

where ψ_x is fermionic field, γ^μ are the Dirac matrices, and m is the mass of fermions. This lagrangian needs to be invariant under the local gauge transformation.

$$\psi(x) \rightarrow \psi'(x) = e^{-ie\alpha(x)}\psi(x), \quad (2.9)$$

where $\alpha(x)$ defines the local phase transformation. For the invariant of lagrangian under the given transformation, it's necessary to introduce a gauge field $A_\mu(x)$, say the photon field, which transforms as:

$$A_\mu(x) \rightarrow A'_\mu(x) = A_\mu(x) + \frac{1}{e}\partial_\mu\alpha(x). \quad (2.10)$$

The ∂_μ replaced by covariant derivative D_μ

$$D_\mu = \partial_\mu + ieA_\mu, \quad (2.11)$$

where e is the electric charge of the fermion, and \mathcal{L} can be written as:

$$\mathcal{L}_{QED}(x) = \bar{\psi}(x)(i\gamma^\mu D_\mu - m)\psi(x) - \frac{1}{4}F_{\mu\nu}(x)F^{\mu\nu}(x), \quad (2.12)$$

where $F_{\mu\nu} = \partial_\mu A_\nu(x) - \partial_\nu A_\mu(x)$ is the electromagnetic field tensor.

2.2.2 Quantum Chromodynamics (QCD)

QCD describes the strong interactions between quarks and gluons. It's a non-abelian gauge theory based on the $SU(3)$ symmetry group. Quarks carry a colour charge and gluons carry colour and anti-colour charge. The free $\mathcal{L}(x)$ for the quarks is:

$$\mathcal{L}(x) = \bar{q}(x)(i\gamma^\mu \partial_\mu - m)q(x). \quad (2.13)$$

This $\mathcal{L}(x)$ needs to be invariant under local transformation.

$$q(x) \rightarrow q'(x) = e^{i\alpha^a(x)T_a}q(x) \quad (2.14)$$

where $\alpha_a(x)$ is the arbitrary local parameter of the transformation and $T_a = \frac{\lambda_a}{2}$, with $a=1,\dots,8$ and λ_a being the Gell-Mann matrices, are the generators of non-abelian symmetry group $SU(3)$. $SU(3)$ is non-abelian, and the algebra of this group is given by $[T_a, T_b] = if_{abc}T_c$, where f_{abc} are the structure constant of this group $SU(3)$. In order to have this lagrangian invariant under this transformation it's necessary to introduce a gauge field, say gluon field G_a^μ , transform as:

$$G_\mu^a(x) \rightarrow G'_\mu^a(x) = G_\mu^a(x) - \frac{1}{g_s}\partial_\mu\alpha_a(x) - f^{abc}\alpha_b(x)G_{c\mu}(x). \quad (2.15)$$

The ∂_μ replaced by covariant derivative D_μ

$$D_\mu = \partial_\mu + g_s T^a G_\mu^a, \quad (2.16)$$

where g_s being the strong interaction coupling constant, and $\mathcal{L}(x)$ can be written as:

$$\mathcal{L}_{QCD}(x) = \bar{q}(x)(i\gamma^\mu D_\mu - m)q(x) - \frac{1}{4}G_{\mu\nu}^a(x)G_a^{\mu\nu}(x), \quad (2.17)$$

where $G_{\mu\nu}^a = \partial_\mu G_\nu^a(x) - \partial_\nu G_\mu^a(x) - g_s f^{abc}G_{b\mu}G_{c\nu}(x)$ is the gluon-field tensor.

2.2.3 Electroweak theory

Electroweak theory was developed by Glashow, Weinberg and Salam in order to combine the electromagnetic and weak theory under the manifestation of gauge symmetry group $SU(2)_L \otimes U(1)_Y$, where L and Y represents the left-handed weak iso-spin and weak hyper-charge. Where Q is the electric charge and T are weak iso-spin $Q = T_3 + Y/2$, which are the generators of symmetry group. For left-handed states Fermions are organized in doublets with weak iso-spin $T=1/2$ and for right-handed states Fermions are organized in singlets with weak iso-spin $T=0$:

$$\chi_L = \begin{pmatrix} v_l \\ l \end{pmatrix}_L \cdot \begin{pmatrix} q^u \\ q^d \end{pmatrix}_L \quad (2.18)$$

$$\psi_R = l_R, q_R^u, q_R^d, \quad (2.19)$$

where l shows the charged leptons, v_l their corresponding neutrinos, and $q^{u,d}$ are the up and down-type quarks. Now, the Lagrangian for these fermions should be invariant under the local transformations of $SU(2)_L \otimes U(1)_Y$:

$$\chi_L(x) \rightarrow \chi'_L(x) = e^{i\beta(x)Y + i\alpha^a(x)\tau_a}\chi_L(x) \quad (2.20)$$

$$\psi_R(x) \rightarrow \psi'_R(x) = e^{i\beta(x)Y} \psi_R(x) \quad (2.21)$$

where $\alpha(x)$ and $\beta(x)$ are the phase transformation factors of the local gauge $SU(2)_L$ and $U(1)_L$, $a=1,2,3$ and $\tau_a = \frac{\sigma_a}{2}$ with σ_a being the Pauli matrices, are the generators of $SU(2)$. Now, using the covariant derivative:

$$D_\mu = \partial_\mu + igW_\mu^a \tau_a + ig'B_\mu Y \quad (2.22)$$

where W_μ^a with $a=1,2,3$ are the fields associated to $SU(2)_L$ symmetry, and B_μ are the field associated to $U(1)_L$ symmetry, where g,g' are their corresponding coupling-constants. The field strength tensor are:

$$W_{\mu\nu}^a = \partial_\mu W_\nu^a - \partial_\nu W_\mu^a + g\epsilon^{abc}W_{b\mu}W_{c\nu} \quad (2.23)$$

$$W_{\mu\nu} = \partial_\mu B_\nu - \partial_\nu B_\mu \quad (2.24)$$

The electroweak Lagrangian is:

$$\begin{aligned} \mathcal{L}_{EW}(x) = & \bar{X}_L(x)\gamma^\mu \left(i\partial_\mu - g\frac{\tau_a}{2}W_\mu^a + \frac{g'}{2}B_\mu \right) X_L(x) + \bar{\psi}_R(x)\gamma^\mu(i\partial_\mu + g'B_\mu)\psi_R(x) \\ & - \frac{1}{4}W_{\mu\nu}^a(x) - \frac{1}{4}B_{\mu\nu}B^\mu, \end{aligned} \quad (2.25)$$

The physical gauge bosons γ, Z, W^\pm are given by:

$$A_\mu = W_\mu^3 \sin \theta_W + B_\mu \cos \theta_W \quad (2.26)$$

$$Z_\mu = W_\mu^3 \cos \theta_W - B_\mu \sin \theta_W \quad (2.27)$$

$$W_\mu^\pm = \frac{1}{2}(W_\mu^1 \mp W_\mu^2), \quad (2.28)$$

where θ_W is the Weinberg angle defined in terms of the coupling constants:

$$\sin \theta_W = \frac{g'}{\sqrt{g^2 + g'^2}} \quad \cos \theta_W = \frac{g}{\sqrt{g^2 + g'^2}} \quad (2.29)$$

where electric charge can be written as:

$$e = g \sin \theta_W = g' \cos \theta_W. \quad (2.30)$$

This Lagrangian describes the interaction between massless fermions fields and massless gauge fields, but by adding the mass terms would violate the gauge invariance. The solution to this problem is to introduce Brout-Englert-Higgs mechanism of electroweak symmetry breaking which gives rise to massive gauge bosons.

2.2.4 Brout-Englert-Higgs mechanism

To solve the mass problem for bosons and fermions by preserving the gauge invariance, Brout, Englert, and Higgs provided a model named as Brout-Englert-Higgs

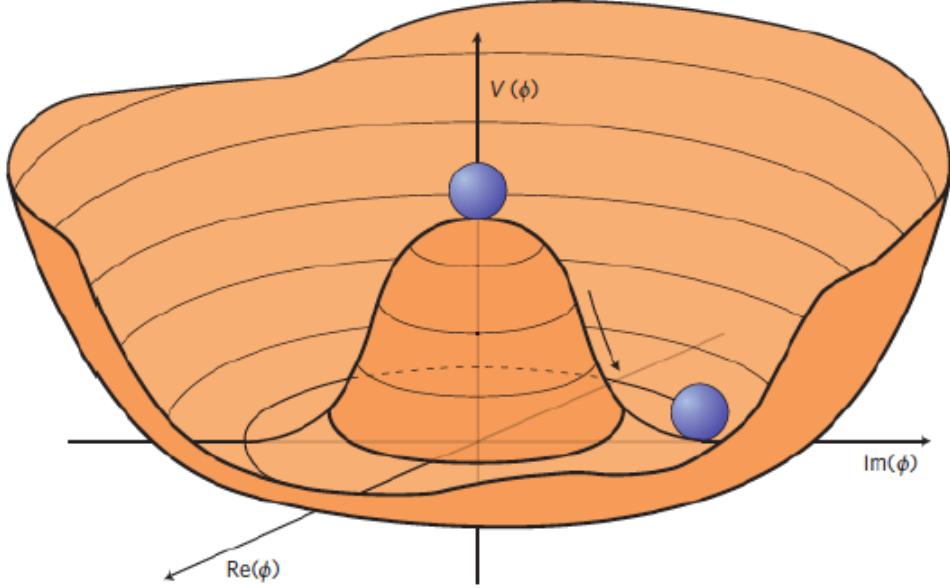


Figure 2.2: Higgs Potential [5] .

mechanism in 1964. In this model a complex scalar field in the form of a doublet of $SU(2)$ with $Y=1$ is introduced:

$$\Phi = \begin{pmatrix} \Phi^+ \\ \Phi^0 \end{pmatrix} = \frac{1}{\sqrt{2}} \begin{pmatrix} \Phi_1 + i\Phi_2 \\ \Phi_3 + i\Phi_4 \end{pmatrix}. \quad (2.31)$$

It's lagrangian can be written in terms of kinematic and potential terms are:

$$\mathcal{L}_{Higgs}(x) = (D_\mu \Phi)^\dagger D^\mu \Phi - V(\Phi) \quad (2.32)$$

where covariant-derivative D_μ is:

$$D_\mu = \partial_\mu + igW_\mu^a \tau_a + ig'B_\mu Y, \quad (2.33)$$

where $V(\Phi)$ is the potential term is given by:

$$V(\Phi) = \mu^2 \Phi \Phi^\dagger + \lambda (\Phi \Phi^\dagger)^2 = \mu^2 \Phi^2 + \lambda \Phi^4, \quad (2.34)$$

with μ and λ being the free parameters. This potential is symmetric under $SU(2) \otimes U(1)$ so the symmetry of Lagrangian remains preserved.

For a stable theory, the potential has to be inferiorly bounded so it has to have $\lambda > 0$, while the sign of μ^2 is not determined. The minimum potential represents the vacuum state and the value of the field gives the vacuum-expectation value (vev) of the Higgs-field:

- $\mu^2 \geq 0$: with a single minimum at $\Phi_0 = \langle \Phi \rangle \equiv v = 0$, the potential has a parabolic shape and the ground-state is symmetric under transformation of $SU(2) \otimes U(1)$;

- $\mu^2 < 0$: at $\Phi=0$ corresponds to a local maximum where the potential has the shape shown in Figure 2.2 and there are degenerate minima corresponding to a circumference with radius:

where

$$|\Phi_0| = \langle \Phi \rangle \equiv v = \sqrt{\frac{-\mu^2}{2\lambda}}. \quad (2.35)$$

For $\mu^2 < 0$, there are multiple states with the same vacuum-energy. Although, the potential is symmetric, the ground-state is asymmetric: so the transformation of $SU(2) \otimes U(1)$ applied to one of the vacuum-state will rotate it to a different orientation which describes a different physical state, so the symmetry is spontaneously broken. Now, a particular ground-state can be chosen with $\phi_1 = \phi_2 = \phi_4 = 0$ and $\phi_3 = v$, we get:

$$\Phi_0 = \frac{1}{\sqrt{2}} \begin{pmatrix} 0 \\ v \end{pmatrix}. \quad (2.36)$$

The τ_1, τ_2 are the generators of $SU(2)$. The vacuum is invariant under the both $SU(2)$ τ_3 -rotation θ and $U(1)$ rotation of $\theta/2$. Now, this combination of the generators is $Q = \tau_3 + Y/2$, where Q is the electric-charge, corresponding to the unbroken part of the gauge group, say $U(1)_{em}$ symmetry-group. After the spontaneous-symmetry-breaking (SSB), three of the four degrees of freedom of the symmetry-group broken and give masses to three gauge-bosons say Z, W^\pm , one degree of freedom is unbroken and leaves one massless gauge-boson to say photon. So, the electro-weak symmetry group is broken with the pattern:

$$SU(2)_L \otimes U(1)_Y \rightarrow U(1)_{em}. \quad (2.37)$$

The field can be written in terms of $SU(2)$ transformation adding four scalar field say $\theta_1, \theta_2, \theta_3, h$, which parameterize the fluctuations around the minimum:

$$\Phi(x) = e^{i\tau^a \theta_a/v} \begin{pmatrix} 0 \\ \frac{v+h}{\sqrt{2}} \end{pmatrix} \simeq \frac{1}{\sqrt{2}} \begin{pmatrix} \theta_2 + i\theta_1 \\ v + h - i\theta_3 \end{pmatrix}. \quad (2.38)$$

The fields $\theta_1, \theta_2, \theta_3$ are the massless Goldstone-bosons generated by the electro-weak symmetry breaking and they can be removed from the Lagrangian by performing the $SU(2)$ gauge-transformation, so the resulting field is called unitary-gauge can be written as:

$$\Phi(x) = \frac{1}{\sqrt{2}} \begin{pmatrix} 0 \\ v + h(x) \end{pmatrix}, \quad (2.39)$$

where $h(x)$ is called the Higgs scalar-field. The Lagrangian can be written as:

$$\mathcal{L}_{Higgs}(x) = \frac{1}{2} (\partial_\mu h)^2 [m_W^2 W_\mu^+ W^{-\mu} + m_Z^2 Z_\mu Z^\mu] \left(1 + \frac{h}{v}\right)^2 - \lambda v^2 h^2 - \lambda v h^3 - \frac{1}{4} \lambda h^4. \quad (2.40)$$

The degree of freedom carried by the massless Goldstone-bosons now transferred to the massive W^\pm and Z bosons. Now, all the bosons can be identified by looking into its field:

$$m_h = \sqrt{2\lambda v} \quad (2.41)$$

$$m_W = \frac{gv}{2} \quad (2.42)$$

$$m_z = \frac{1}{2}v\sqrt{g+g'^2} = \frac{m_W}{\cos\theta_W} \quad (2.43)$$

The Lagrangian contains triple and quartic coupling terms of the field h with the heavy gauge-bosons W^\pm and Z, which are proportional to the masses of the gauge-bosons, $\lambda_{VWH} = \frac{2m_v^2}{v}$ and $\lambda_{VVHH} = \frac{m_v^2}{v^2}$ respectively, and there also triple and quartic Higgs-boson self-couplings, which proportional to the mass of the squared of the Higgs-boson:

$$\lambda_{HHH} = \lambda v = \frac{m_h^2}{2v} \quad (2.44)$$

$$\lambda_{HHHH} = \frac{\lambda}{4} = \frac{m_h^2}{8v^2} \quad (2.45)$$

2.2.5 Yukawa coupling and fermion masses

The Higgs-mechanism explain the masses of the vector-bosons, but it cannot explain the masses of the fermions. By adding the mass term for the fermions would violate the gauge invariance of the Lagrangian. Now, by adding the gauge-invariant interaction term between the fermions and the Higgs-field, called Yukawa term, by assuming that the fermions acquire their masses from interactions with Higgs-field like the Vector-bosons do.

$$\mathcal{L}_{Leptons}(x) = -y_l(\bar{X}_L\phi\psi_R + \bar{\psi}_R\phi^*X_L) \quad (2.46)$$

where y_l are free parameters for $l = e, \mu, \tau$. By using the parameterization of the Higgs-field the term becomes:

$$\mathcal{L}_{Leptons}(x) = \frac{-y_lv}{\sqrt{2}}(\bar{l}_Ll_R + \bar{l}_Rl_L) - \frac{y_l}{\sqrt{2}}(\bar{l}_Ll_R + \bar{l}_Rl_L)h = -m_l\bar{l}l - \frac{m_l}{v}\bar{l}lh \quad (2.47)$$

where $m_l = \frac{-y_lv}{\sqrt{2}}$ is the fermion masses, and the $\mathcal{L}_{Leptons}(x)$ contains the kinetic term of the massive leptons and the interaction term of the leptons with the Higgs-field. Where the Yukawa coupling is proportional to the $y_l = \frac{m_l\sqrt{2}}{v}$ mass of the fermion. Since there are no left-handed neutrinos in the SM, while right-handed ones needs to be massless. Similarly, Lagrangian for the quarks is:

$$\mathcal{L}_{Quarks}(x) = -y_d^{ij}(\bar{u}_i, \bar{d}_i)_L\Phi d_{jR} - y_u^{ij}(\bar{u}_i, \bar{d}_i)_L\Phi_C u_{jR} + h.c., \quad (2.48)$$

where y_d^{ij} are matrices for the quark families up and down-type quarks q. The Yukawa-coupling matrices can be diagonalized if the left-handed quark filed are rotated by a unitary-transformation, $u_L^i \rightarrow u_L^{i'} = U_u^{ij}u_L^j$ and $d_L^i \rightarrow d_L^{i'} = U_d^{ij}d_L^j$, where $V_{CKM} = U_u^\dagger U_d$ is the Cabibbo-Kobayashi-Maskava (CKM) matrix. Now, we can express the Lagrangian in the diagonal form and in the unitary gauge:

$$\mathcal{L}_{Quarks}(x) = -m_d^i\bar{d}_id_i\left(1 + \frac{h}{v}\right) - m_u^i\bar{u}_iu_i\left(1 + \frac{h}{v}\right) \quad (2.49)$$

Decay	BR	Observed
bb	58%	✓
WW	22%	✓
gg	8.6%	
$\tau\tau$	6.3%	✓
cc	2.9%	
ZZ	2.6%	✓
$\gamma\gamma$	0.23%	✓
Z γ	0.15%	
$\mu\mu$	0.02%	

Table 2.1: Higgs boson decay branching ratios for $m_H = 125.09\text{GeV}$ [15]

2.3 The Higgs boson and Higgs pair production

On 4 July 2012, ATLAS and CMS both have announced that they observed a new particle whose properties is compatible with the SM Higgs-boson in the mass region of 125GeV [2,3] at the CERN’s Large Hadron Collider(LHC) with pp collisions data at $\sqrt{s} = 7\text{TeV}$ in 2011 and with $\sqrt{s} = 8\text{TeV}$ in 2012. ATLAS experiment observation was given by the combination of decay channels $H \rightarrow ZZ^* \rightarrow 4l$, $H \rightarrow \gamma\gamma$ and $H \rightarrow WW^* \rightarrow l l v l$ with a significance of 5.9σ , while CMS experiment observation was given by the combination of decay channels of $H \rightarrow ZZ^* \rightarrow 4l$, $H \rightarrow \gamma\gamma$ and $H \rightarrow WW^* \rightarrow l l v l$, $H \rightarrow b\bar{b}$ and $H \rightarrow \tau^+\tau^-$ with a significance of 5.0σ . The mass of the Higgs-boson has been measured [6] from the combination of the results by ATLAS and CMS in the final state of four-leptons to be:

$$m_H = 125.09 \pm 0.24(0.21_{\text{stat}} \pm 0.11_{\text{syst}})\text{GeV}, \quad (2.50)$$

and the studies about its spin and parity quantum numbers reveal that particle which properties compatible with the SM neutral spin-0 boson with $J^P = 0^+$ [7]. After the discovery, it was also proven that it couples to gauge bosons and fermions of the third generation [8–13], these couplings consistent with the SM prediction. Moreover, not all couplings are predicted by the SM like couplings with first and second generation and Higgs-boson self-couplings still unobserved.

2.3.1 Higgs production and decay

All the Higgs-boson production and decay modes, with their cross-section and branching ratios (BRs), can be predicted given mass of the Higgs-boson. The main leading order (LO) Feynman diagrams that contributes to the production of Higgs-boson in Figure 2.3.

The ggF is the production mode with largest $\sigma = 48.58\text{pb}$ at a $\sqrt{s} = 13\text{TeV}$. We know Higgs-boson does not interact with massless particles like photons and gluons, it can decay into a pair of such particles only through quark triangle-loops, like happens in ggF production, it’s decays through top-quark loops because of their high mass and the large top-quark Yukawa coupling. Higgs-boson decay

	bb	WW	$\tau\tau$	ZZ	$\gamma\gamma$
bb	33%				
WW	25%	4.6%			
$\tau\tau$	7.4%	2.5%	0.39%		
ZZ	3.1%	1.2%	0.34%	0.076%	
$\gamma\gamma$	0.26%	0.10%	0.029%	0.013%	0.0005%

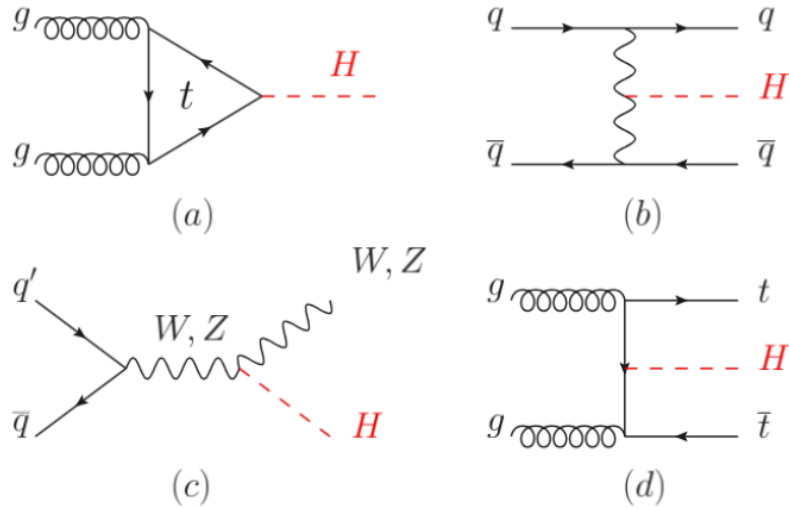
Table 2.2: Di-Higgs boson decay branching ratios for $m_H = 125.09\text{GeV}$.

Figure 2.3: Main Leading Order (LO) Feynman diagrams contributing to the Higgs production in (a) gluon-gluon fusion (ggF), (b) vector-boson fusion (VBF), (c) Higgs-strahlung (or associated production with a gauge boson, VH), (d) associated production with a pair of top quarks (ttH)

branching ratios for $m_H = 125.09\text{GeV}$ in Table 2.1 and Figure 6.5 .

2.3.2 Higgs pair production and decay

In this thesis work, I have to study about the Higgs-boson pair production and final signature of its decay mode. The most dominant Higgs-boson pair production mode is ggF through the destructive interference of two LO diagrams in Figure 2.5. These diagrams involve the top-quark loops and triple Higgs-self coupling. The SM cross-section for Higgs-boson pair production via ggF at $\sqrt{s} = 13\text{TeV}$ at NLO is $\sigma = 33.41\text{fb}$.

The di-Higgs system decay has different final states resulting from all of the combinations of the decays of the two Higgs-boson. Table 2.2, shows the branching ratios for all of the combinations by assuming SM Higgs-boson mass $m_H = 125.09\text{GeV}$. This research is about the $b\bar{b}\tau^+\tau^-$ final state. In this final state, one Higgs decays to b-quark pair and the other decays to tau pair with tau decay

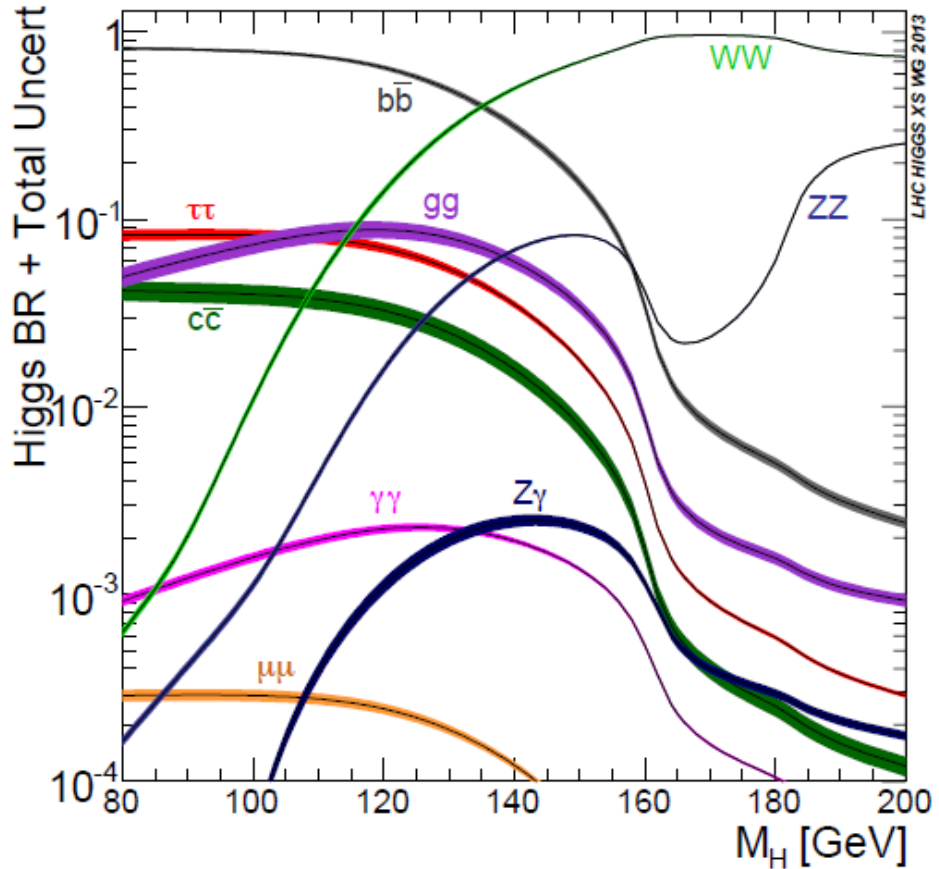


Figure 2.4: Standard Model Higgs boson decay branching ratios as a function of the Higgs mass m_H [14].

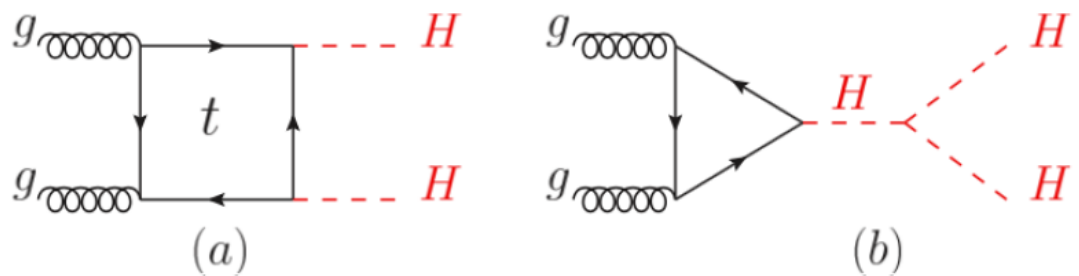


Figure 2.5: Standard Model Higgs boson decay branching ratios as a function of the Higgs mass m_H .

leptonically and other tau decay hadronically. In the final signature of $b\bar{b}\tau_{lep}\tau_{had}$, we get two b-jet, isolated electron or muon, and hadronic tau with the branching ratio of 45.8%.

Chapter 3

The ATLAS experiment at LHC

The CERN Acronym for the (European Organization for Nuclear Research) is one of the largest scientific research centers over the world, where the world's largest and complex instruments are employed to study the basic constituents of matter and fundamental structure of the universe. The CERN sit's at the French-Swiss border near Geneva. European scientific center of Excellence was founded in 1954, it's a Joint venture collaboration with 22 member states.

Particle accelerators and detectors are instruments which we use at CERN, to boost beams of particles (proton and ions) to high energies before to collide each other in the Large Hadron Collider (LHC). Detectors are used to observe and record the garbage of these collisions. One of these detectors is the ATLAS (A Toroidal LHC Apparatus) experiment.

This chapter introduces the accelerators, Then, ATLAS detectors and it's components that allow trigger on and collects data events during the Collision for physics analyses.

3.1 The Large Hadron Collider

The LHC [16] at CERN is the highest energy collider ever organized for accelerating and colliding protons and ions up-to designed energy scale. It produces proton-proton (pp) collisions at a center-of-mass-energy of 14 TeV and an instantaneous luminosity of $10^{34} \text{ cm}^{-2} \text{ s}^{-1}$, and lead-ion collision at a center-of-mass-energy of 2.76 TeV per nucleon and an instantaneous luminosity of $10^{27} \text{ cm}^{-2} \text{ s}^{-1}$.

To obtain such an energy scale we have installed numerous accelerators used as injectors to the LHC. For proton sources, we use a hydrogen bottle to extract them by applying electric fields and then injected to the first accelerator. Each boosts the proton up-to certain energy scale and then injects them to the next one until they reach the LHC with an initial energy of 450 GeV. When proton beams obtain the certain energy scale then they collide to four interaction points say four particle detectors, which built to collect data events for physics analyses named ATLAS [17], CMS (Compact Muon Solenoid) [18], ALICE (A Large Ion Collider Experiment) [19] and LHCb (Large hadron Collider beauty) [20] Figure 3.1.

ATLAS and CMS dedicated to general-purpose detectors which ever built for the search of SM Higgs boson and its properties, SM precision measurements, and

to look for viable new physics BSM. ALICE detector is dedicated to studying the products of the heavy-ion collision to study the phenomenology of strong interaction. LHCb detector is dedicated to studying the B-meson physics and flavour physics in general, investigating CP violation, lepton universality, and lepton flavour violation. Also, there are two more small experiments, such as TOTEM [21] and LHCf [22], installed some distance from the interaction points to study the production of particles along the beam direction in the forward region.

3.1.1 Machine design

The LHC is a long circular collide with 27km diameter sited in the tunnel built between 1984 and 1989 for LEP (Large Electron positron) collider. This tunnel is located between the Jura mountains and the Geneva airport, under the ground surface of 45m and 170m. Proton beams are injected from the CERN injectors (accelerator systems) to LHC with a series of bunches containing 1.15×10^{11} protons, and each beam designed to have 2808 circulating bunches. There are 72 trains of bunches, with 25ns spacing within the train, and 12 empty bunches between the two trains. In the LHC, we use radio frequency (RF) cavities for accelerated beams, and correct use and focus into small areas where collisions take place, we use large magnetic filed (8.33T) with addition to dipoles, quadrupoles, and higher-order.

We got a peak collision rate of 40MHz, as a result of collisions between circulating beams that occur at every 'bunch crossing'. To maximize the pp collision rate near the interaction point (IP) we squeeze the beam up-to transverse size of $\sim 17\mu\text{m}$. We kept two beams together in a single beam pipe, for approximately 140m in each direction near the IP. To avoid unwanted collision we kept beams on parallel orbits when these are ready to collide at IP we just removed the separation between them.

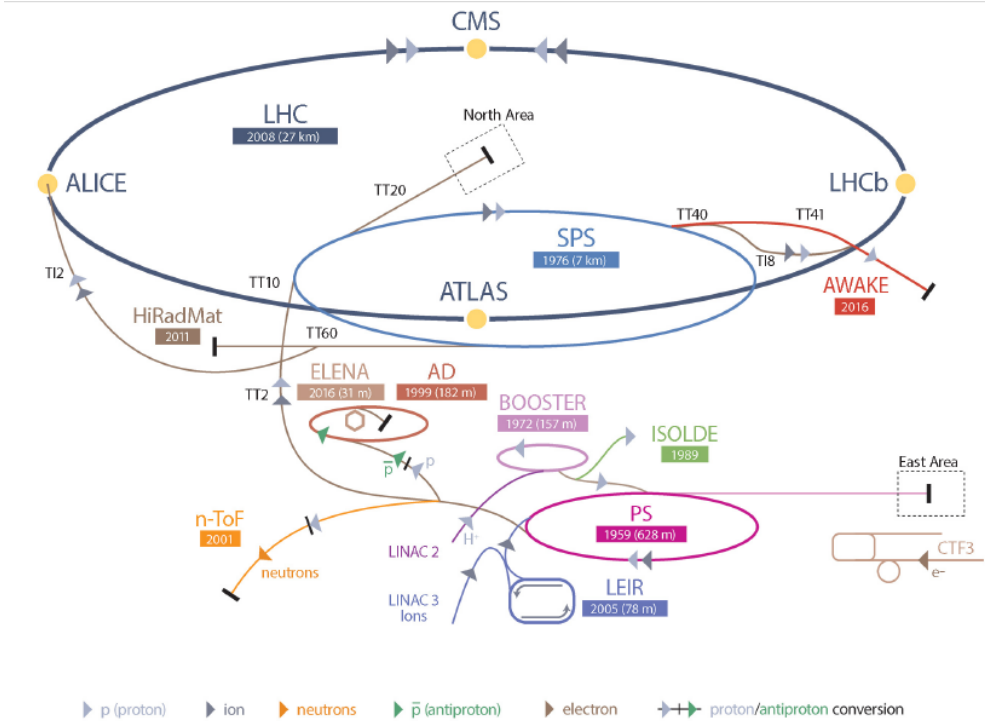


Figure 3.1: The Layout for LHC and CERN accelerator as injector chain for the LHC [16].

Collision rate depends upon instantaneous luminosity and collision cross-section σ :

$$\frac{dN}{dt} = \mathcal{L} \cdot \sigma. \quad (3.1)$$

The instantaneous luminosity is:

$$\mathcal{L} = \frac{N_b^2 n_b f_{rev} F \gamma}{4\pi \epsilon \beta^*} \quad (3.2)$$

where N_b is the number of particles per bunch, n_b number of bunches per beam, f_{rev} revolution frequency, F is a geometric function to account for crossing angle between the beams, γ stands for relativistic Lorentz factor, ϵ is beam emittance (a measure of the uniformity of momentum of particles in the beam) and β^* is a measure how narrow the beam is at the IP. The integrated luminosity $L = \int \mathcal{L} dt$ used to measure how many collisions occurred. The desired number of events associated with a given process with the given cross-section $\sigma_{process}$. So, many of LHC physics processes have a small cross-section, we have to maximize the luminosity as much as possible.

3.1.2 The LHC operation schedule

First, pp collision at a center-of-mass-energy of 900 GeV operated at LHC in November 2009. That was increased in 2010 up-to 7 TeV. For 2010 and 2011 it's using $\sqrt{s}=7$ TeV and in 2012 it increased up-to 8 TeV. Run 1, end of the first

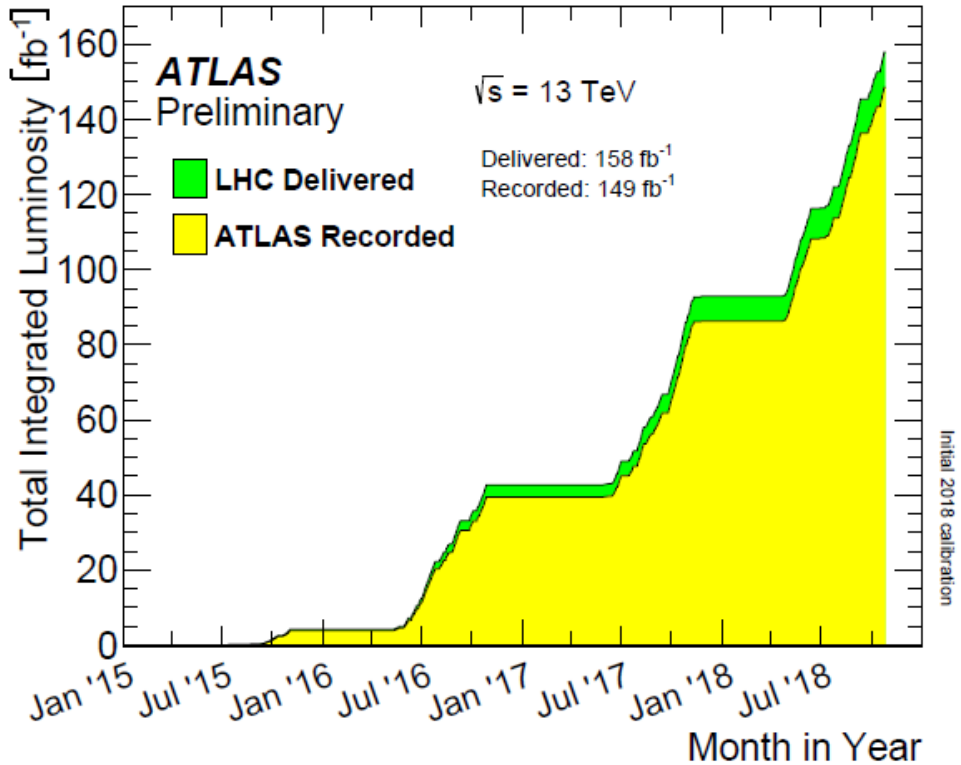


Figure 3.2: In Run 2, Integrated Luminosity delivered by the LHC and recorded by ATLAS experiment [23].

phase of operation , the LHC delivered 5.5 fb^{-1} and 22.8 fb^{-1} at 7 TeV and 8 TeV respectively.

Run 2, started with collisions at $\sqrt{s}=13$ TeV in 2015, with instantaneous luminosity achieved was 1.38×10^{34} , with bunch crossing of 25 ns. At the end of Run 2 on December 2018, total delivered luminosity was 158 fb^{-1} and the ATLAS experiment recorded 149 fb^{-1} . The Figure 3.2 shows the integrated luminosity delivered by the LHC and recorded by ATLAS in Run 2.

There a second long shut down phase and will operate again in 2021 with Run 3 is expected to deliver integrated luminosity of 300 fb^{-1} at $\sqrt{s}=14$ TeV. There should be a third long shutdown called High-Luminosity-LHC (HL-LHC) to obtain the instantaneous luminosity of $5-7 \times 10^{34} \text{ cm}^{-2} \text{ s}^{-1}$ with an expected integrated luminosity at the end of the HL-LHC is 3000 fb^{-1} Figure 3.3.

3.2 The ATLAS detector

The high luminosity and center-of-mass-energy of the Large Hadron Collider (LHC) at CERN allows us to study the physics of pp collisions at the TeV scale. For high interaction rates, particle multiplicities, energies, and radiation dose, as well as for precision measurements we have to design particle detectors. ATLAS is one of the two general-purpose detector at LHC. It is designed to study the PP and ion-ion

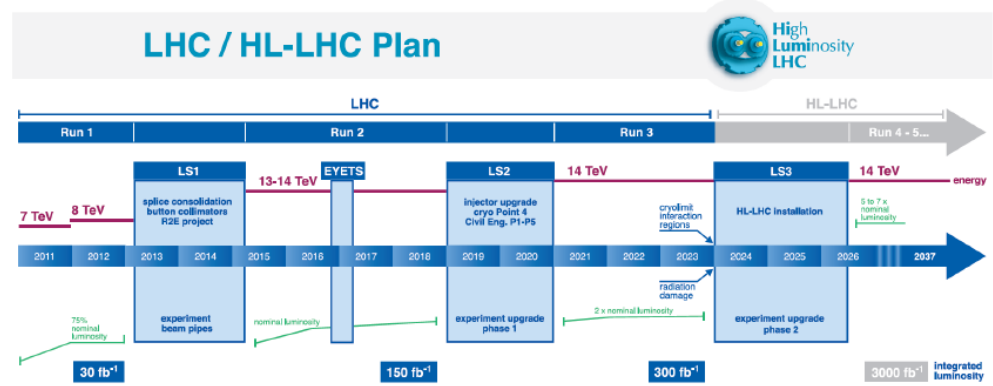


Figure 3.3: LHC operation schedule [24].

collision. The detector has been designed to allow for several types of research:

- the search for a standard model Higgs boson and the measurement of its properties;
- supersymmetry searches;
- precision tests of electroweak interactions, flavour physics, and QCD;
- measurements of the properties of the top quark;
- measurements of the properties of top quark;

To deal with these challenges, ATLAS was designed to have in Table 3.1.

3.2.1 Coordinate system

The ATLAS detector in Figure 3.5 is designed according to the right-handed Cartesian coordinate system with origin lies at interaction point. In this system, the beam-line along z-axis and an x-y plane are transverse to the beam-line, where the center of LHC ring pointing to the positive x-axis and y-axis pointing upward. For referring to physics objects in the detector we used cylindrical coordinates, with (r, θ, ϕ) named as radius, polar, and azimuthal angle. Both angles θ and ϕ are measured from positive z-axis and positive x-axis respectively.

To account for the energy and momentum of the outgoing particles in the transverse plane where conservation of energy and momentum are considered:

to be known as an initial state while the initial component along the z-axis is not known. We define transverse momentum as $P_T = \sqrt{P_x^2 + P_y^2}$, and transverse energy as $E_T = E \sin \theta$.

The θ angle is usually converted to pseudo-rapidity:

$$\eta = -\ln \tan \left(\frac{\theta}{2} \right) \quad (3.3)$$

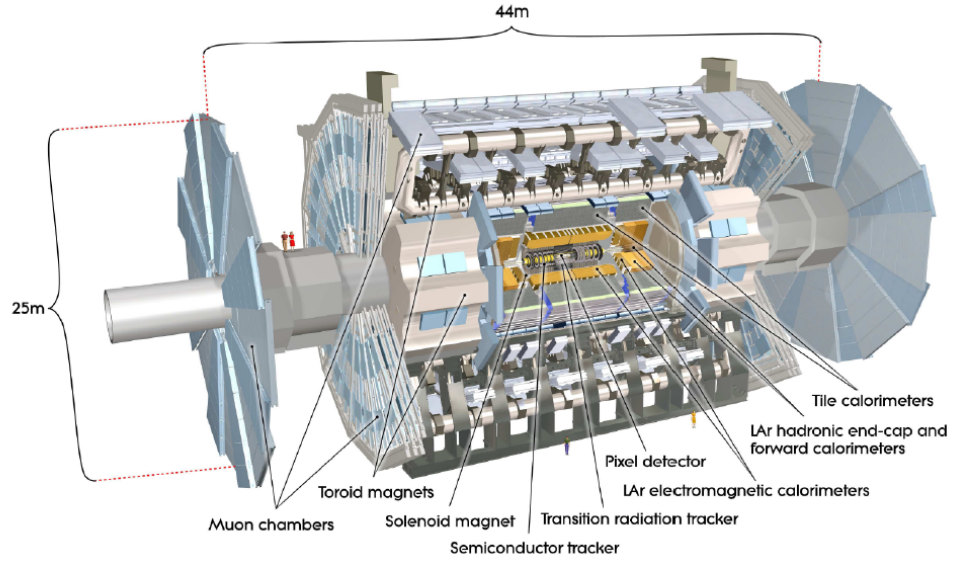


Figure 3.4: ATLAS detector with sub-systmes are labelled [26] .

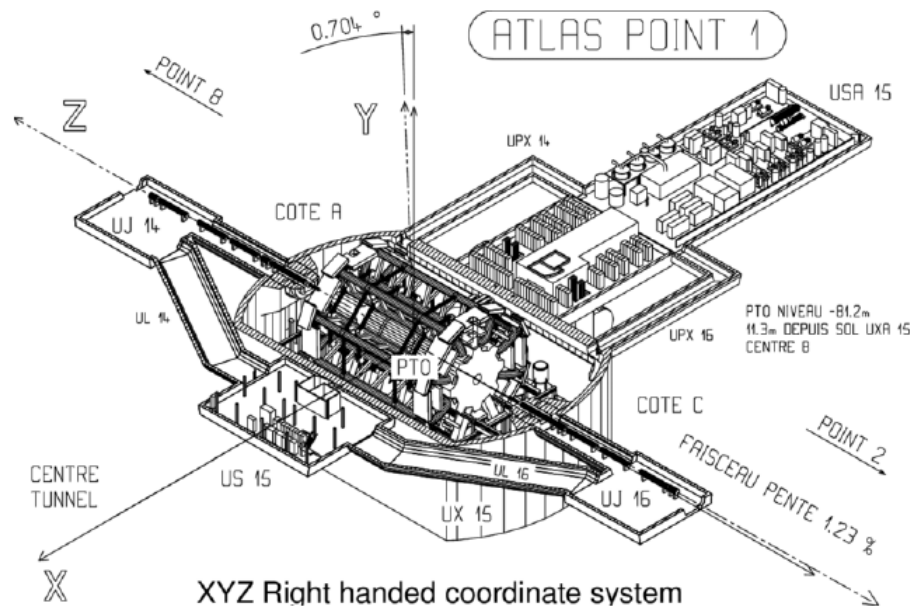


Figure 3.5: ATLAS detector coordinate system [17] .

Detector Component	Design Resolution	η Coverage	
		Measurement	Level 1 Trigger
Tracking	$\sigma_{P_T}/P_T = 0.05\% P_T \oplus 1\%$	± 2.5	None
EM Calorimetry	$\sigma_E/E = 10\%/\sqrt{E} \oplus 0.7\%$	± 3.2	± 2.5
Hadronic Calorimetry	$\sigma_E/E = 50\%/\sqrt{E} \oplus 3\%$	± 3.2	± 3.2
Barrel and End-Cap			
Forward	$\sigma_E/E = 100\%/\sqrt{E} \oplus 10\%$	$3.1 < \eta < 4.9$	$3.1 < \eta < 4.9$
Muon Spectrometer	$\sigma_{P_T}/P_T = 10\% \text{ at } P_T = 1 \text{ TeV}$	± 2.7	± 2.4

Table 3.1: Performance goals of ATLAS detector. Units of p_T and E are GeV [25].

which approaches the rapidity:

$$y = \frac{1}{2} \ln \frac{E + p_z}{E - p_z} \quad (3.4)$$

The η is 0 in transverse plane and infinite along the z-axis, with $\eta = 1$ at 45° from the axis. The η is 0 in transverse plane and infinite along the z-axis, with $\eta = 1$ at 45° from the axis. To describe the angular distance between the objects in the $\eta - \phi$ plane is $\Delta R = \sqrt{\Delta\eta^2 + \Delta\phi^2}$.

3.2.2 Magnets

To measure the momentum for charged particles as the momentum component of the charged track which is perpendicular to a uniform magnetic field can be estimated from its bending radius R in the magnetic field B: $p[\text{GeV}] = 0.3B[\text{T}]R[\text{m}]$. The ATLAS magnet system [27] consisted of three different kinds of superconducting magnets in Figure 3.6.

In the inner detector magnetic field supplied by a central solenoid with a magnetic field of 2T in the z-direction. For muon-spectrometer, three air-core toroid magnets (the barrel toroid and two end-cap toroids) provided the magnetic field with an intensity of 0.5T and 4T. The barrel toroid generates the magnetic field in the central zone of muon-spectrometer in the tangential direction of the (ϕ -direction), where the end-cap toroid generates the magnetic field in the forward areas of the muon-spectrometer.

3.2.3 Inner detector

The inner detector (ID) [28, 29] is the ATLAS apparatus element which lies closest to the interaction point. It's designed for the reconstruction of tracks, primary vertices for the interactions of particles, and possible secondary-vertices from the decaying of long-lived particles. The inner-detector has a cylindrical shape which sites around the interaction-point with radius of 1.1 m and length of 6.2 m, which is immersed in the magnetic field of 2T provided by the barrel solenoid, which one allows to measure the charge and momentum of the particles from curvature of

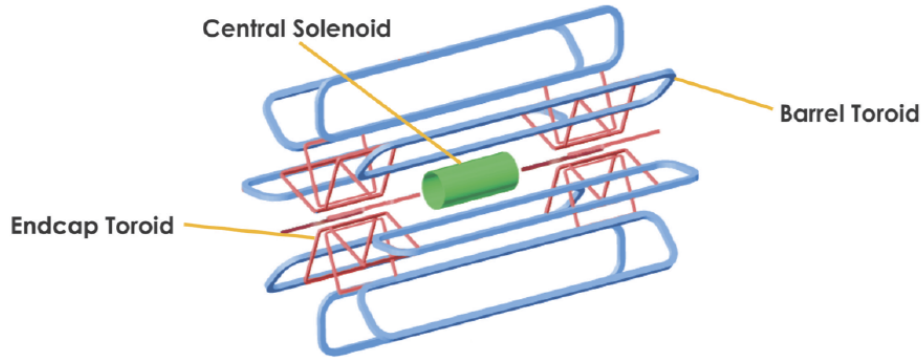


Figure 3.6: ATLAS magnet system (layout).

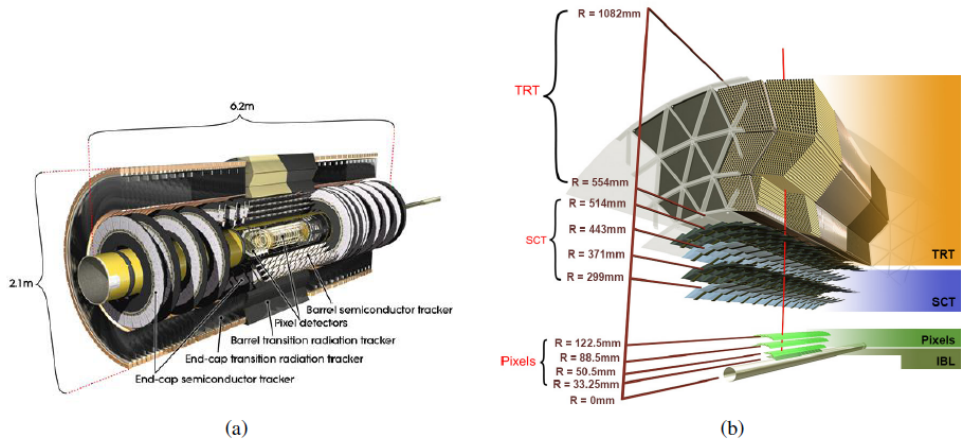


Figure 3.7: (a) ATLAS Inner detector (layout). (b) A zoomed view of inner detector [30].

the trajectories.

The ID gives accurate and efficient tracking for charged particles with $p_T > 0.5\text{GeV}$ within $|\eta| < 2.5$, with the transverse-momentum resolution of:

$$\frac{\sigma_{p_T}}{p_T} = 0.05\% p_T \bigoplus 1\% \quad (3.5)$$

The layout for ID is in Figure 3.7.

Silicon-pixel tracker and the insertable B-Layer (IBL)

The silicon-pixel detector is the closest component to the beam. Its made of silicon-pixels that designed to have a high granularity for the resolving of primary and secondary interaction vertices. It contains three cylindrical layers in the barrel section, that positioned at the radial distances of 50.5, 88.5, and 122.5 mm and on the other hand disks perpendicular to the beams in the end-caps about the longitudinal distances of 49.5, 58.0, and 65.0 mm. Where the B-layer placed at the radius of 50.5 mm, which imparts an important part for the detecting of secondary

vertices for the identification of the jets coming from the b-quark hadronization. During the first LHC long shutdown in 2014, there was installed a fourth-pixel layer inside the existing detector, name insertable B-Layer (IBL) with a radius of 33 mm from the beam axis. Which provides an additional space point near to the interaction point (IP), which significantly improves the b-jet identification. The detector layers are made up of silicon sensor modules and there are approximately 92 million pixels (consequently, readout channels) in the system.

Semiconductor tracker (SCT)

The SCT is a silicon strip detector consists of four layers strips axially placed concerning the beam-pipe in barrel and on the R-direction end-caps. To form a two-sided module, other identical silicon-strip sensors are glued to back-to-back with the first one, by creating a stereo angle of 40 mrad. So the entire SCT with covering the barrel region and end-caps is outlined to more than 6 million channels.

The spatial resolution of the detector is $\sigma_\phi = 17\mu\text{m}$ in the bending region ($R - \phi$), and $\sigma_{z,R} = 580\mu\text{m}$ in the z (barrel) or R (end-cap) region.

Transition radiation tracker (TRT)

The transition radiation tracker (TRT) sits at the most external part of ATLAS inner detector. It's a straw drift tube tracker, which is formed of modules formed from the bundles of 4 mm diameter straws, supplied with a gas mixture consisting of 70% Xe, 27% CO_2 and 3% O_2 which are employed in a propylene radiator.

The spatial resolution of TRT is $\sigma_\phi = 130\mu\text{m}$ in the bending direction ($R - \phi$). The TRT contributes to momentum resolution and pattern recognition. When charged-particles cross the border within straw and the propylene foils into the barrel (end-caps) they emit transition radiation photons, which then grasped by the Xe gas mixture.

3.3 Calorimeter system

Outside the inner detector and its magnetic field, there placed an ATLAS calorimeter system [31]. The calorimeter system plans to measure the energy and position of the particles by using the sampling calorimeter with different materials sandwiched together in layers. Calorimeter covers the range of $|\eta| < 4.9$ and divided into two types: Electro-magnetic calorimeter (EM-Cal) used to measure the energy of electrons and photons, while Hadronic calorimeter (H-Cal) used to measure the energy of hadrons.

Electromagnetic calorimeter (EM)

EM calorimeter is used to measure the energy of electron and photon. Its sampling calorimeter with lead used as absorber and lead-argon (LAr) used as the active material.

There are two half barrels for EM calorimeter (named EMB) with the coverage of $|\eta| < 1.475$ (with 4mm gap at $z=0$), and with two wheels at both sides in the end-cap (named EMEC), first covering the $1.375 < |\eta| < 2.5$ and second covering the $2.5 < |\eta| < 3.2$.

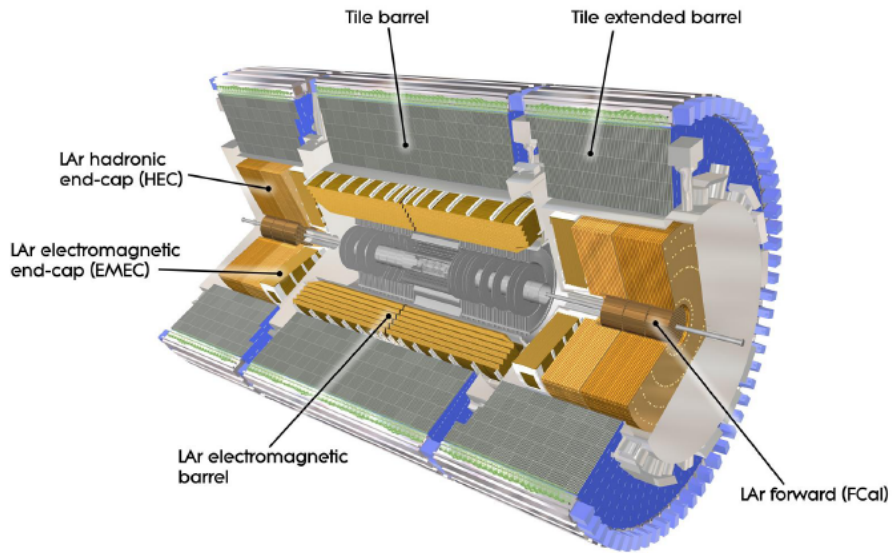


Figure 3.8: ATLAS calorimeter system [32].

The EM calorimeter has the energy resolution of:

$$\frac{\sigma_E}{E} = \frac{10\%}{\sqrt{E}} \bigoplus 0.7\% \quad (3.6)$$

Hadronic calorimeter (HCal)

The hadronic calorimeter is used to measure the energy and direction of hadrons produced by the hadronization of quarks and gluons, HCal surrounds the EM calorimeter. HCal have three different parts:

Hadronic tile calorimeter

This covers the range of $|\eta| < 1.7$ and it builds with steel as an absorber and plastic scintillator as an active material. It consists of a barrel with coverage of $|\eta| < 0.8$ and two extended barrel with coverage of $0.8 < |\eta| < 1.7$, which located behind the EM calorimeter.

Hadronic LAr end-caps calorimeter (HEC)

It consists of two-wheels per end-cap with coverage of $1.5 < |\eta| < 3.2$, which located behind the EMEC. It builds with copper as absorber and LAr as an active material.

Forward calorimeter (FCal)

It covers the range of $3.1 < |\eta| < 4.9$. In the forwarding region there a high particle fluxes and energies, that's why they're long showers in the small volume by the design constraints and thus must be very dense. FCal divided into three partitions. The first partition is designed for electromagnetic measurements that use copper as passive material and LAr as an active material. The other two partitions used for hadronic measurements used tungsten as passive material.

Energy resolution for the Hadronic-Calorimeter is:

$$\frac{\sigma_E}{E} = \frac{50\%}{\sqrt{E}} \bigoplus 3\% \quad (3.7)$$

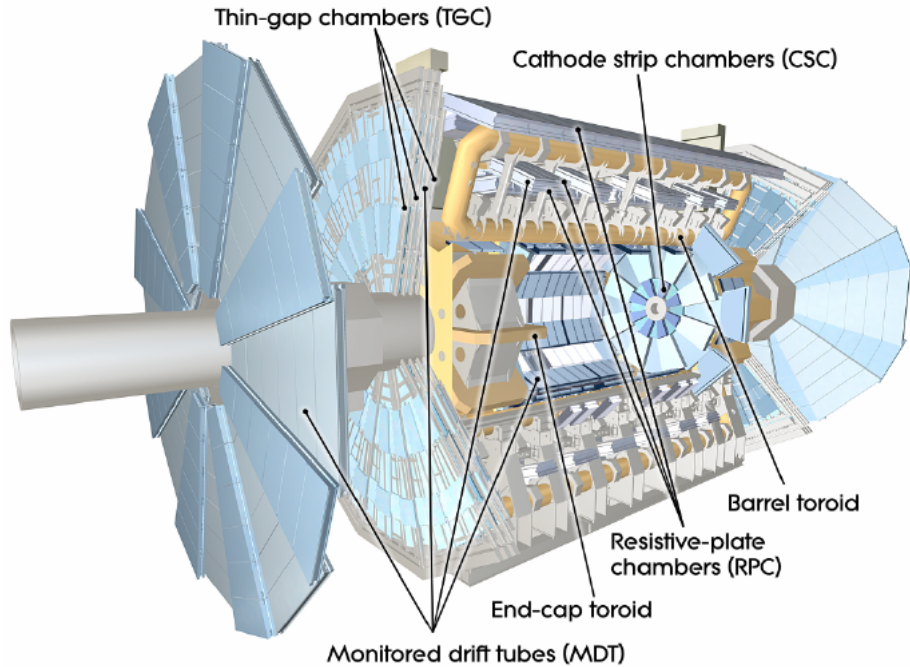


Figure 3.9: ATLAS muon-spectrometer [33].

for the barrel and end-caps, its:

$$\frac{\sigma_E}{E} = \frac{100\%}{\sqrt{E}} \bigoplus 10\% \quad (3.8)$$

in the forward region.

3.3.1 Muon spectrometer

Muon-Spectrometer [33] is the largest outermost detector of ATLAS, which fully covers the calorimeter system. It's designed to identify muons and measure their momentum in the p_T range from 10 GeV up-to-the order of 1 TeV.

Muon-Spectrometer covers the range of $|\eta| < 2.7$, and the design benchmark is 10% transverse momentum resolution for 1 TeV muon track. The Muon-Spectrometer relies on the four different gas detector technologies. Two resistive-plate-chambers (RPC) in the barrel region and thin gas chambers (TGC) in the end-cap region, provide the trigger signal. While the other two gas detectors monitored drift tubes (MDT) and the cathode strip chambers (CSC) provide the momentum measurement. The muon-chambers are placed in the barrel ($|\eta| < 1.05$) in three cylindrical layers around the beam-axis, while in the end-cap region with $1.05 < |\eta| < 2.7$, which placed in three wheels. The complete layout for muon-spectrometer is in Figure 3.9.

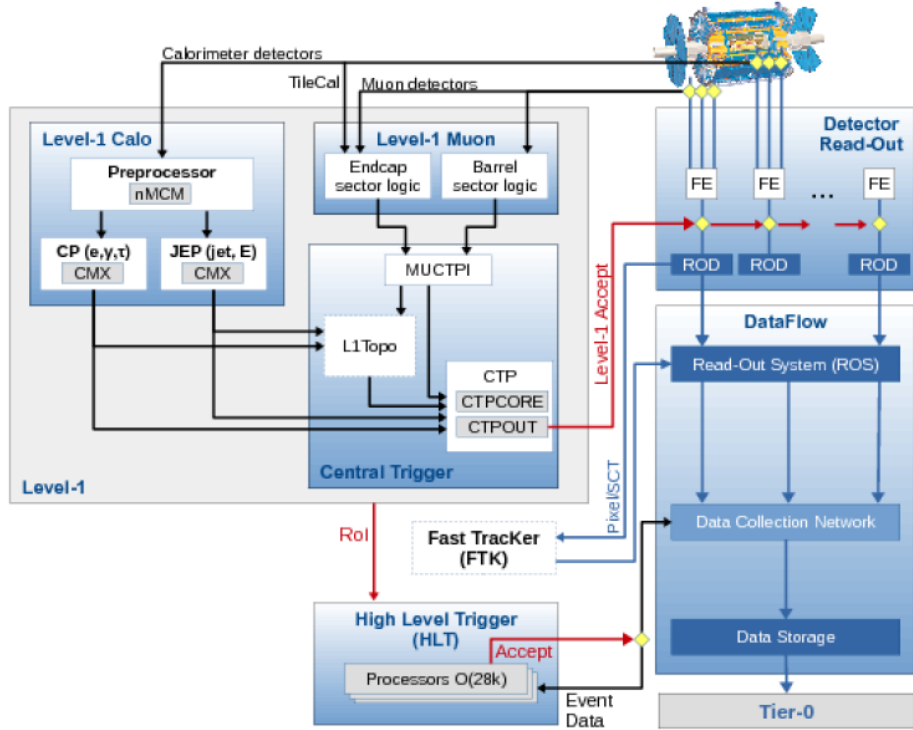


Figure 3.10: ATLAS trigger and DAQ system [34].

3.3.2 Trigger system

To identify and record the interesting events ATLAS uses the trigger and data acquisition (TDAQ) system [34]. In Figure 3.10, it analyses online events at two successive levels with increasing complexity, which allows reducing the event rate through the hardware level-1 (L1) and software-based high-level trigger (HLT). Using fast and dedicated hardware, the L1 trigger determines the regions of interest (RoIs) in the calorimeters and the muon-spectrometer, with reducing the rate from 40MHz to 100kHz with about $2.5\mu s$ of total latency. The HLT was born from the merging of L2 and Event Filter levels which one used in Run 1. It consists of a fast algorithm that accesses data from RoI or using the full event information. It has full access to the full-precision information and high-granularity from the muon-spectrometer, calorimeters, and the inner-detector, and its software-based. Data-Acquisition (DAQ) system monitors the data recording on the storage disks. If the L1 triggers data event, the DAQ system moves the event data from detector electronics to specific detector Read-Out Drivers (ROD), and if the data events passed the HLT, then the data-events are merged and recorded to disk.

Chapter 4

Decays of di-Higgs boson to $b\bar{b}\tau_{lep}\tau_{had}$

In the published analysis [35], searching for the Higgs-boson pair production with a final state of two b-quarks and two τ -leptons by considering the two sub-channels say $\tau_{lep}\tau_{had}$ and $\tau_{had}\tau_{had}$. Where the subscript lep=lepton and had=hadron are the decay mode of τ -leptons. Here, In this thesis, I will focus on the $\tau_{lep}\tau_{had}$ channel, where one Higgs-boson decays to a pair of b-quarks and other Higgs-boson decays to a pair of τ -leptons with one lepton decays leptonically and other lepton decays to hadronically.

Above mentioned di-Higgs decay sub-channels are list below with branching ratio:

1. $b\bar{b}\tau_{lep}\tau_{had}(BR : 45.8\%)$
2. $b\bar{b}\tau_{had}\tau_{had}(BR : 41.9\%)$

These branching ratios can be calculated as:

4.1 $b\bar{b}\tau_{had}\tau_{had}$

In this sub-channel $H \rightarrow \tau_{had}\tau_{had}$, the probability of one Higgs goes to τ_{had} is 64.79%.

$$P(\tau_{had}) * P(\tau_{had}) = \frac{(64.79) * (64.79)}{100} = 41.9\% \quad (4.1)$$

Total Branching Ratio for $H \rightarrow \tau_{had}\tau_{had}$ =41.9%.

4.2 $b\bar{b}\tau_{lep}\tau_{had}$

In this sub-channel $H \rightarrow \tau_{lep}\tau_{had}$, the probability of one Higgs goes to τ_{lep} is 35.24%.

4.2.1 Combination 1

For first combination, probability of Higgs (1) goes to τ_{lep} and the Higgs (2) goes to τ_{had} .

$$P(\tau_{lep}) * P(\tau_{had}) = \frac{(35.24) * (64.79)}{100} = 22.83\% \quad (4.2)$$

4.2.2 Combination 2

For second combination, probability of Higgs (1) goes to τ_{had} and the Higgs (2) goes to τ_{lep} .

$$P(\tau_{lep}) * P(\tau_{had}) = \frac{(64.79) * (35.24)}{100} = 22.83\% \quad (4.3)$$

For both combinations total Branching Ratio for $H \rightarrow \tau_{lep}\tau_{had}$ and $H \rightarrow \tau_{had}\tau_{lep}$ which is $(22.87\% + 22.87\%)$ is 45.7%.

4.3 Object reconstruction in the ATLAS detector

4.3.1 Bottom-quark

The bottom quark says b-quark is the third-generation quark with a charge of $-1/3$ and mass of 4.18 GeV [36]. It's notable due to a product of all top-quark decays and also decay product of Higgs-boson. B-hadrons have a long lifetime to travel some distances before decaying but on the other hand, its short enough to reach inside the inner detector.

4.3.2 b-tagging

For the identification of jets originates from the b-quark (bottom-quark) hadronization is termed as b-tagging, which we use in this thesis in the final state of $hh \rightarrow b\bar{b}\tau^+\tau^-$. Life-time of b-hadrons Figure 4.1b of the order of $\tau \sim 1.6$ ps. For multivariate analysis in boosted-decision trees (BDTs) we use b-tagging as input variables to identify in the final state of $b\bar{b}\tau^+\tau^-$.

4.3.3 tau-lepton

Tau-leptons are the heaviest leptons other than electron and muon in the SM with the mass of 1776.86 ± 0.12 MeV, and decay with the mean life-time of $\tau = 290.3 \pm 0.5$ fs [36]. tau-lepton are the only leptons which decays into light leptons and hadrons Figure 4.1a. Tau-leptonic (τ_{lep}) decay mode with branching ratio of $\sim 35\%$ Table 4.1 and hadronic tau (τ_{had}) decay mode with branching ratio of $\sim 65\%$ Table 4.2.

4.3.4 Missing transverse energy

The missing transverse energy corresponds to that momentum which was not reconstructed in the transverse plane of the detector, that corresponds to particles

Leptonic modes $\sim 35\%$

$\tau^\pm \rightarrow e^\pm v_e v_\tau$	17.83%
$\tau^\pm \rightarrow \mu^\pm v_\mu v_\tau$	17.41%

Table 4.1: τ_{lep} decay modes [36].

Hadronic modes $\sim 65\%$

$\tau^\pm \rightarrow \pi^\pm v_\tau$	11%
$\tau^\pm \rightarrow \pi^\pm \pi^0 v_\tau$	26%
$\tau^\pm \rightarrow \pi^\pm \pi^0 \pi^0 v_\tau$	9%
$\tau^\pm \rightarrow \pi^\pm \pi^\pm \pi^\mp v_\tau$	9%
$\tau^\pm \rightarrow \pi^\pm \pi^\pm \pi^\mp \pi^0 v_\tau$	5%

Table 4.2: τ_{had} decay modes [36].

which did not interact with detector material like neutrinos. The missing transverse momentum can be defined as:

$$\vec{p_T}^{miss} = \vec{p_T}^{initial} - \vec{p_T}^{final} = -\vec{p_T}^{final} \quad (4.4)$$

In the final state, It's equal to the negative of visible momentum vector. The quantity used at ATLAS [37] is missing transverse energy (E_{miss}^T), whose calorimeter energy measurements take calculations for all particles except the muon. For muon missing transverse energy is measured from the muon-spectrometer.

$$\vec{E}_T^{miss} = - \sum_{electrons} \vec{E}_T^e - \sum_{photons} \vec{E}_T^\gamma - \sum_{jets} \vec{E}_T^{jet} - \sum_{muons} \vec{E}_T^\mu \quad (4.5)$$

In $b\bar{b}\tau^+\tau^-$ analysis, E_{miss}^T in the final state is due to the neutrinos coming from the tau-lepton decay.

4.4 Monte Carlo and Data Samples

Monte-Carlo and Data samples of the year of 2015_2018 at a centre-of-mass energy of $\sqrt{s} = 13$ TeV corresponding to an integrated luminosity of $137fb^{-1}$. We use $hh \rightarrow b\bar{b}\tau_{lep}^+\tau_{had}^-$ Figure 4.2a as a signal and $t\bar{t}$ Figure 4.2b set as a major dominated background.

4.5 Event Selection

An event selection is applied to select events which contain the $b\bar{b}\tau_{lep}^+\tau_{had}^-$ in the final state. Trigger algorithms are applied to test the events pass the single- τ trigger (STT). The invariant mass of the di-tau system, $m_{\tau\tau}^{MMC}$ calculated by missing-mass calculator (MMC) higher than 60 GeV. In the final state, signal-region (SR) contains the above requirement and two b-tagged jets.

- An electron or muon+ τ -object $\tau_{had-vis}$
- Two b-tagged jets
- E_T^{miss} from neutrino produced in the τ -lepton decay

Offline Triggers for $b\bar{b}\tau_{lep}\tau_{had}$:

- Single-Lepton (e or μ) Trigger (SLT)
- $p_T^{\text{lepton}} > 25\text{-}27\text{GeV}$, $p_T^\tau > 20\text{GeV}$
- Signal region (SR) has 1 τ , 1e or 1 μ central b-tagged jets and $m_{\tau\tau}^{\text{MMC}} > 60\text{GeV}$

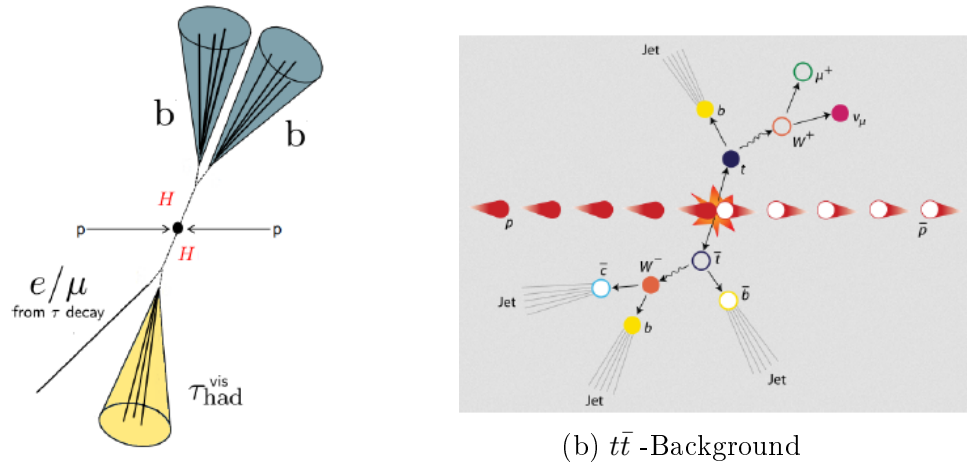
Figure 4.1: (a) τ -jets and (b) b-jets

Figure 4.2: (a) Signal and (b) Background

Chapter 5

Multivariate Analysis in HEP

In high-energy physics experiments, there is a large amount of data recorded during the particle collisions and interactions, which are analyzed by advanced analysis techniques to extract useful information from the data. These multiple variables are like transverse momentum, energy deposit in the calorimeters, kinematic variables which are used to characterize the final state. To find a correlation between the variables we can use multivariate analysis for such correlations [38]. These multivariate (MVA) analysis based on machine learning, widely used for signal and background classification in HEP. Like that signature of Higgs overlap with other backgrounds. For this purpose, a multivariate analysis toolkit (TMVA) [39] has been developed and integrated into the Root framework [40]. TMVA introduces different algorithms for multivariate analysis, but we will look into boosted-decision trees.

5.1 Multivariate Technique

TMVA software package provides root integration environment for processing, evolution and application of multivariate classification. MVA methods depend upon “supervised learning” algorithms. This means we have to provide the training events with desired and known outputs. The TMVA depend on two phases:

- Training phase
- Application phase

5.1.1 Training phase

For the training phase, we need to train, test and analyze the multivariate method. For these users need to interact with dataset and multivariate methods. A factory class is a source of interaction between the user and the multivariate method. For this purpose, we define a factory class object named factory object with the following parameters:

- For classification purpose we need to specify the signal and background dataset.

- To select the input variables, we need to specify those variables as input which can best optimize the signal and background.
- we choose efficient method for multivariate analysis.

Training, testing and evolution are done by factory object. After this, we create a ROOT file where we store the results from MVA outputs with signal and background and efficiency plots. The performance of the MVA method depends upon the input variables which can best discriminate between signal and background.

5.1.2 Application phase

In this phase, the Reader object communicates between the user and MVA-methods and read the encoded information in weight files created during the training phase. There are the following parameters for this phase:

- ROOT or text files.
- Weight files created during the training phase.
- Input variables.
- method trained during the training phase.

The Application phase flow-chart is in Figure 5.1.

5.2 Boosted Decision Trees

BDT is mostly used in HEP to classify events with different categories like Signal & Background Figure 5.2. It takes several variables as input training samples, where decision-trees consists of recursive (yes no) or (left right) decisions, based on sequential cuts applied on a single variable at a time. This splitting mode is repeated until the impurity cannot be further reduced. To measure the impurity, we use the Gini-index defined as:

$$Gini = (s + b)P(1 - P) = \frac{sb}{s + b}, \quad (5.1)$$

signal purity is $P=s/(s+b)$, “s” is signal and “b”. All events are scored between the range of -1 and +1, background-like events gets a score near -1 and signal-like events get a score near +1.

Performance of a single decision tree drops rapidly. If the dataset contains a complex structure, the best solution for the classification is boosting where many single trees are created to classify the signal and background. In BDT training there a multiply decision trees and formed a forest of trees to give a combined score. That's why BDT gives better performance and discriminate between signal and background rather than DTs. For each tree, a cut is found on each variable and this procedure is repeated for each node.

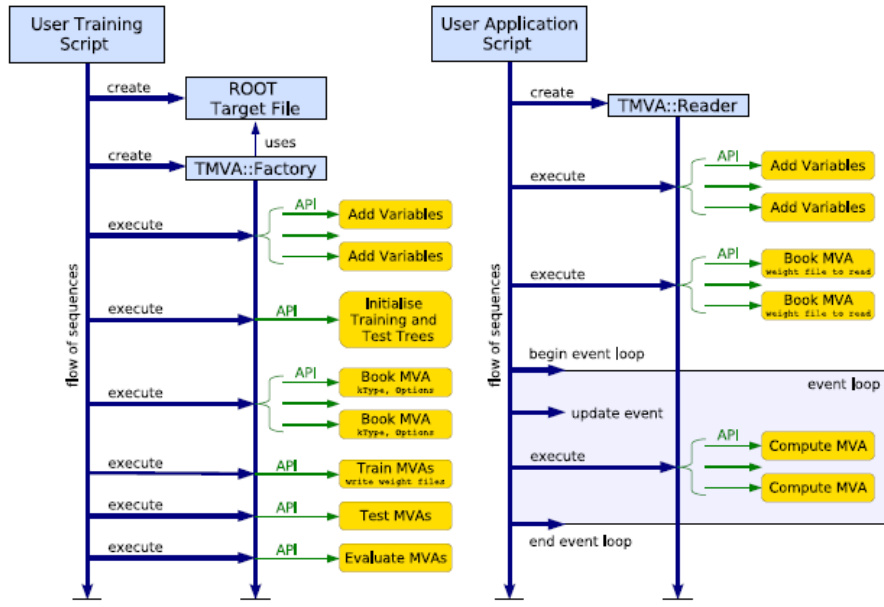


Figure 5.1: (Left) Flow-chart of TMVA training application & (Right) Flow-chart of TMVA analysis application [39].

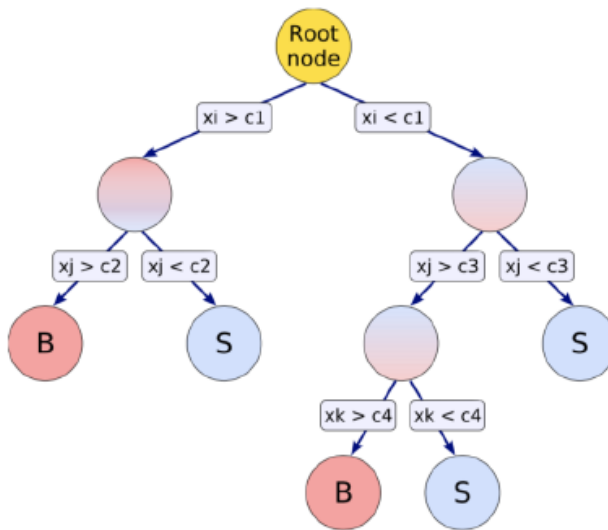


Figure 5.2: BDT apply different cuts on each branch with "S" is signal and "B" is background [39].

5.3 Input variables

To improve the separation of signal from background BDTs are used. To discriminate between “S” & “B”, we take 33 variables as input. To optimize the kinematics, we use TMVA with boosted decision trees. The significance for kinematics is calculate by Log-Likelihood-Ratio:

$$LLR = \sqrt{2\left((s+b)\ln\left(1 + \frac{s}{b}\right) - s\right)} \quad (5.2)$$

5.3.1 BDT training for $b\bar{b}\tau_{lep}\tau_{had}$ channel

To optimize signal from background $t\bar{t}$ for the MC and Data samples, BDT training carried out for $b\bar{b}\tau_{lep}\tau_{had}$ non-resonant channel. For training phase, we choose 50% events for kfold=0 & kfold=1. For kfold=0 even events for training and odd events for testing and for kfold=1 odd events for training and even events for testing. Then, the sensitivity is calculated for kinematic variables. At first, we get the most sensitive variable from 33-variables named mhh Figure 5.3a. After getting one variable with high-sensitivity then I combine mhh with a list of 32-variables and calculate the sensitivity of 2-vars with mhh and other variables. Now, mBB has a high sensitivity with the combination of mhh Figure 6.1b. Then calculate sensitivity for 3-vars by the combination of mhh, mBB with a list of 31-variables and repeat this procedure up-to 15-variables Figure 5.6a.

After 12-vars the sensitivity going to decrease. This plot shows significance of the highest sensitive variable combination while training in each round and adding 13th variable the sensitivity get decreases Figure 5.6b.

After, the optimization we take first six-variables which can best discriminate signal from dominated background Figure 5.3a,6.1b,5.4a,6.1d,5.5a,6.2a. Now, there are six-variables for BDT which optimize the signal from background.

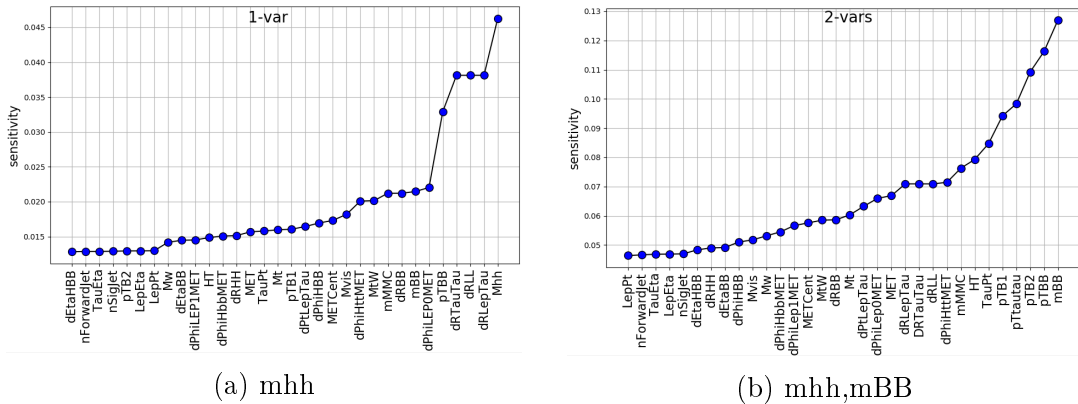


Figure 5.3: (a) Significance of 1_var and (b) Significance of 2_vars

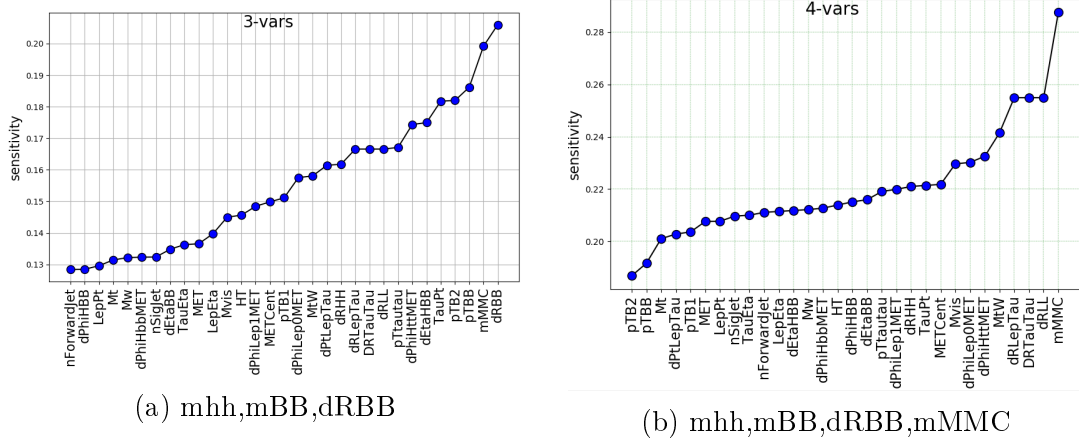


Figure 5.4: (a) Significance of 3_vars and (b) Significance of 4_vars

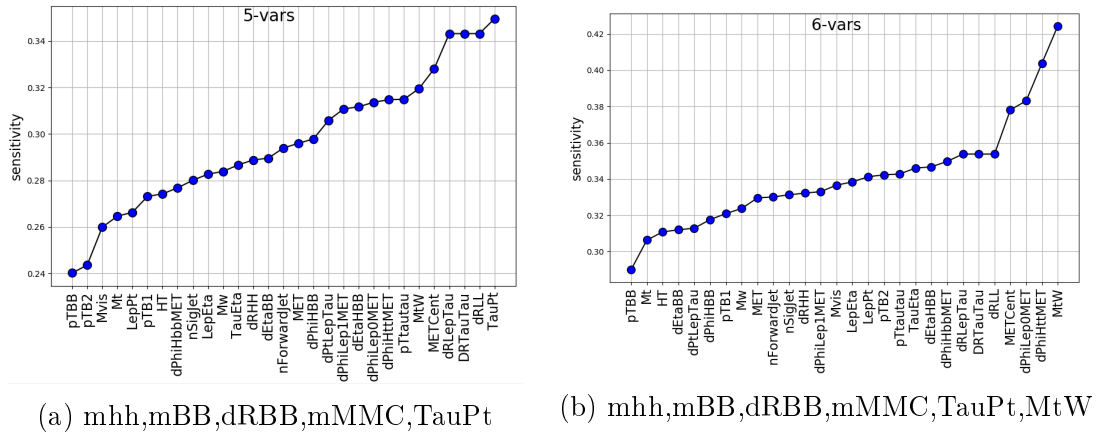


Figure 5.5: (a) Significance of 5_vars and (b) Significance of 6_vars

- invariant mass of Higgs pair → reconstructed from pair of taus and pair of b-jet;
- invariant mass of pair of b-jet;
- dRBB: angular distance between pair of b-jets;
- mMMC: $m_{\tau\tau}^{MMC}$ pair of taus invariant mass, find by (MMC);
- TauPt: P_T^τ transverse momentum of tau;
- MtW: transverse mass between the lepton and E_T^{miss} which is $m_T^W = \sqrt{2p_T^l E_T^{miss}(1 - \cos \Delta\phi)}$;

5.4 Comparison with MC and DATA Samples

In order to carried out the comparison 6-vars for SLT, I take our 6-vars measured on the basis of their best sensitivity these are Mhh, mBB, dRBB, mMMC, TauPt, MtW and compared with 6-vars which are listed in ATLAS Notes Mhh , mMMC,

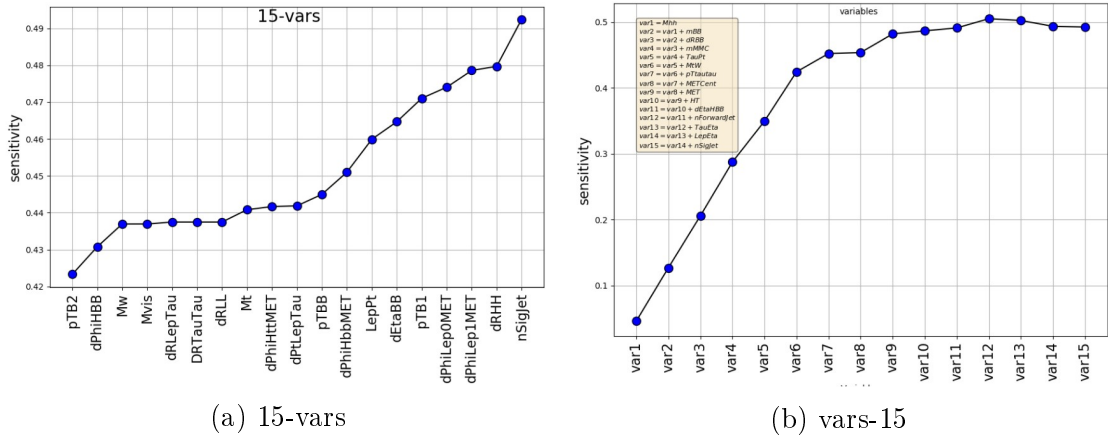


Figure 5.6: (a) Significance of 15_vars and (b) Significance of all vars up-to 15_vars

Year	2016	2017	2018	2016+17	2016+18	2017+18	2016+17+18
\mathcal{L}_{int}	36	40	60	76	96	100	137

Table 5.1: Yearly based Integrated Luminosity.

mBB, dRLepTau, dRBB, MtW. This comparison is carried out independently for different periods 2016, 2017 and 2018 with increasing luminosity Table ??.

5.4.1 Period 2016

For the period of 2016, I've to make comparison plots for MC and DATA at integrated luminosity of 36 fb^{-1} and their overlap plots Figure 5.7, 5.8 and 5.9. Correlation between variables for signal and background in the respective of MC and DATA Figure 5.10. BDT classification for MC and DATA in Figure 5.11 and ROC curve Figure 5.12.

Year	2016	2017	2018	2016+17	2016+18	2017+18	2016+17+18
	0.17	0.19	0.22	0.28	0.30	0.31	0.35

Table 5.2: Sensitivity for old variables.

Year	2016	2017	2018	2016+17	2016+18	2017+18	2016+17+18
	0.18	0.20	0.25	0.30	0.33	0.35	0.42

Table 5.3: Sensitivity for MC-variables.

Year	2016	2017	2018	2016+17	2016+18	2017+18	2016+17+18
	0.25	0.24	0.22	0.38	0.36	0.36	0.44

Table 5.4: Sensitivity for DATA-variables.

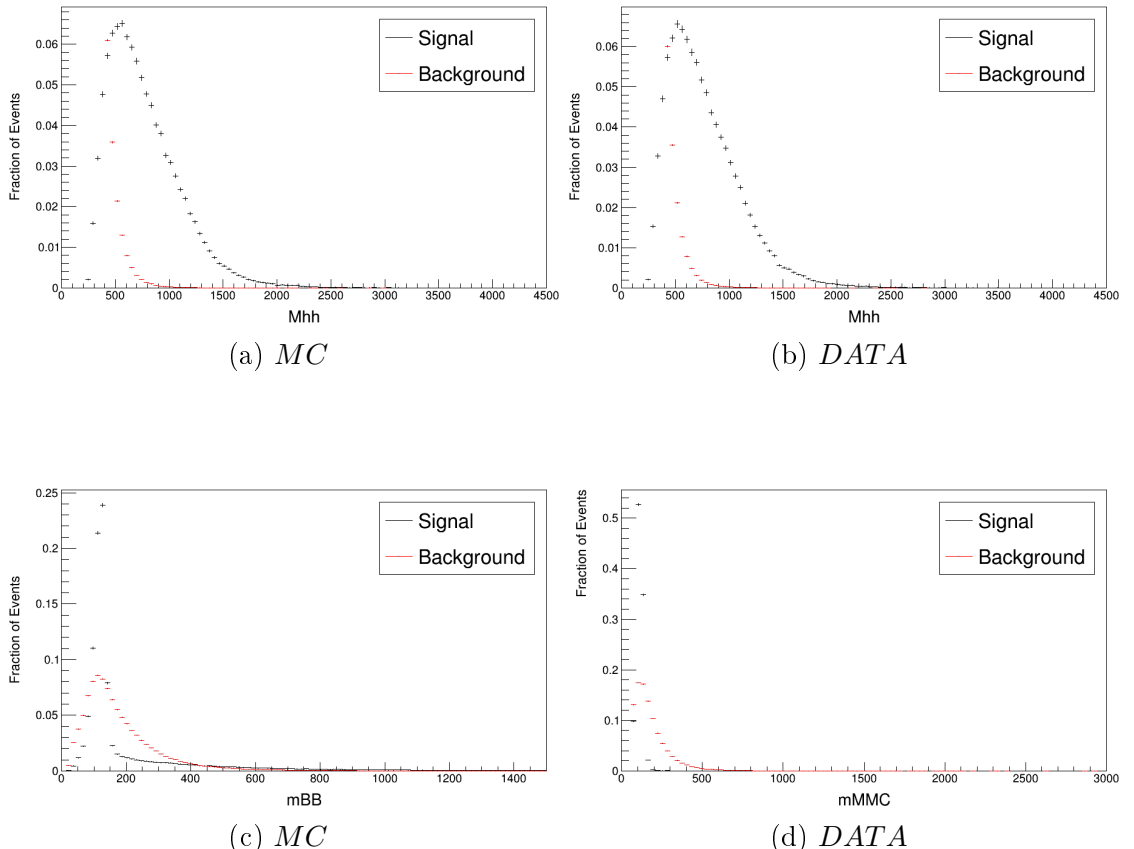


Figure 5.7: (a) MC-Input Variables (2016) and (b) DATA-Input Variables (2016)

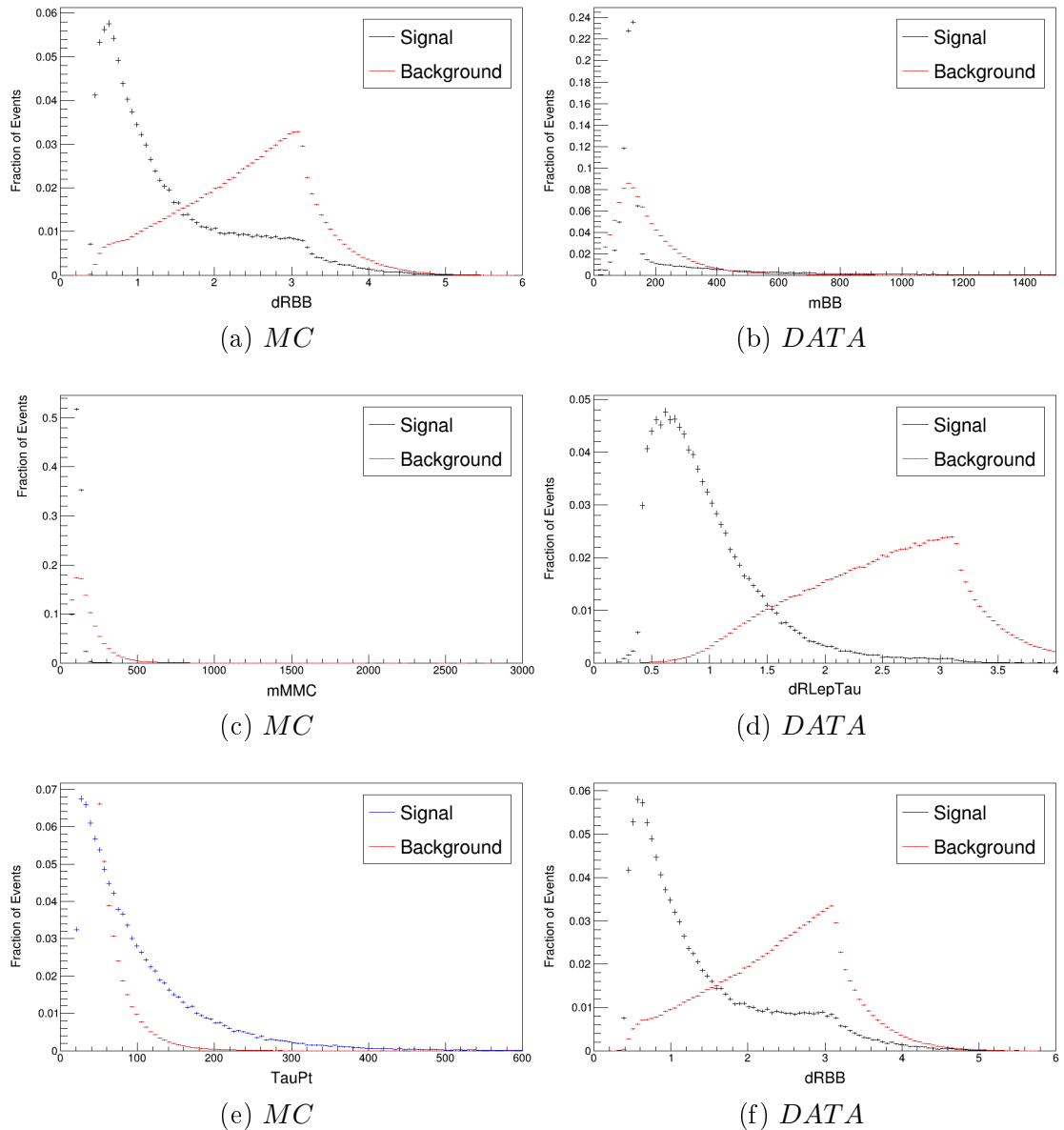


Figure 5.8: (a) MC-Input Variables (2016) and (b) DATA-Input Variables (2016)

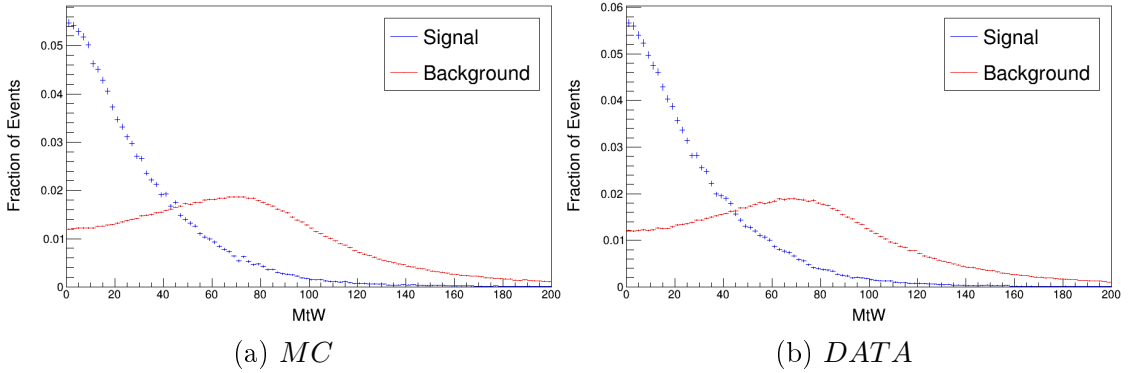


Figure 5.9: (a) MC-Input Variables (2016) and (b) DATA-Input Variables (2016)

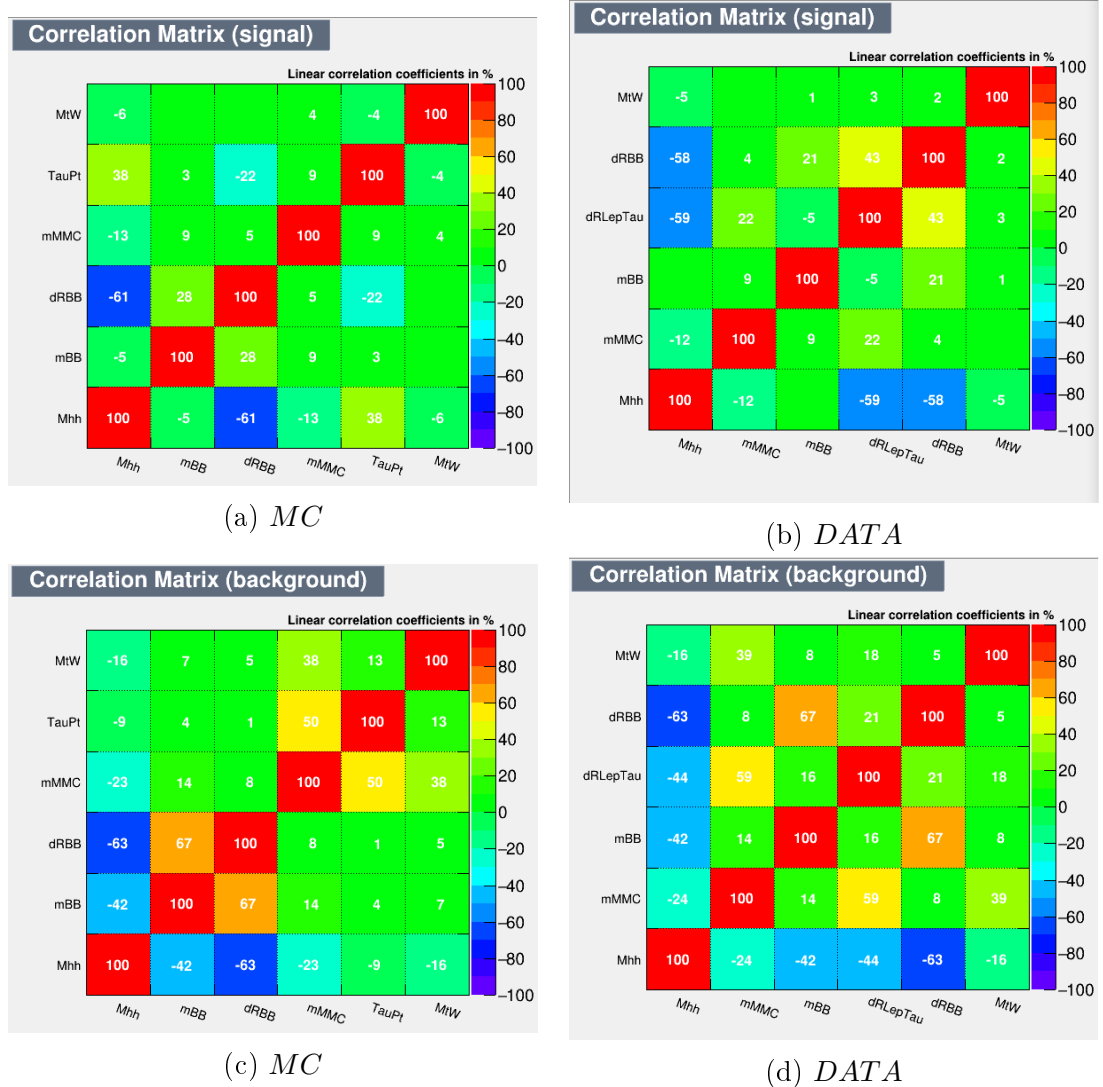


Figure 5.10: (a) Correlation matrix MC (2016) and (b) Correlation matrix DATA (2016)

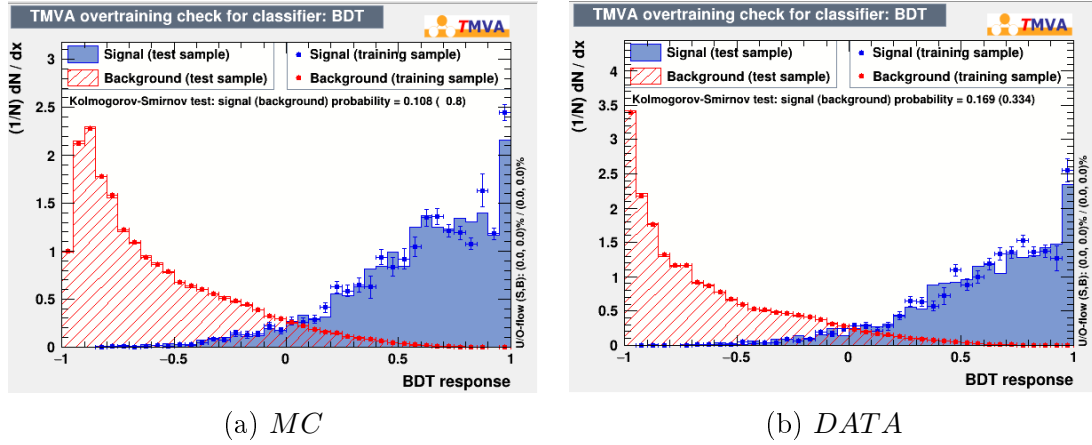


Figure 5.11: (a) MC Classifier (2016) and (b) DATA Classifier (2016)

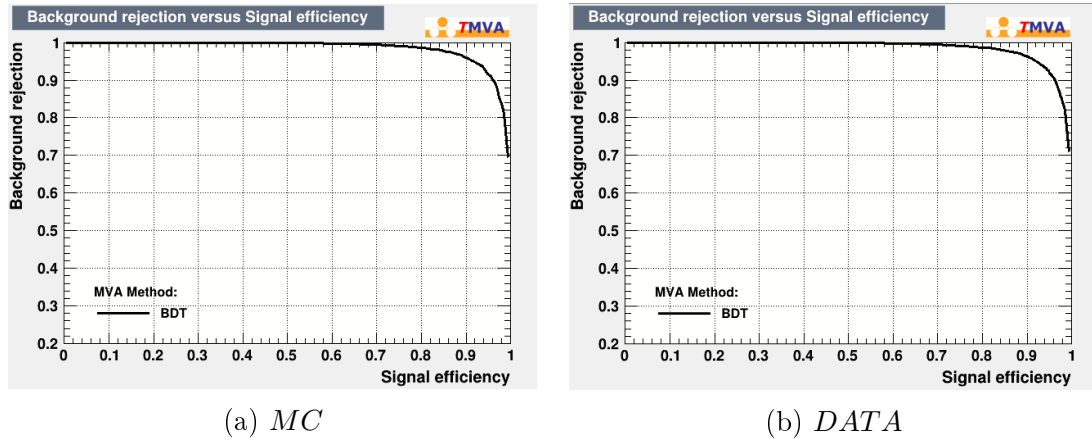


Figure 5.12: (a) ROC curve (2016) and (b) ROC curve (2016)

5.4.2 Period 2017

For the period of 2017, I've to make comparison plots for MC and DATA at integrated luminosity of 40 fb^{-1} and their overlap plots Figure 5.13, and 5.14. Correlation between variables for signal and background in the respective of MC and DATA Figure 5.15. BDT classification for MC and DATA in Figure 5.16 and ROC curve Figure 5.17.

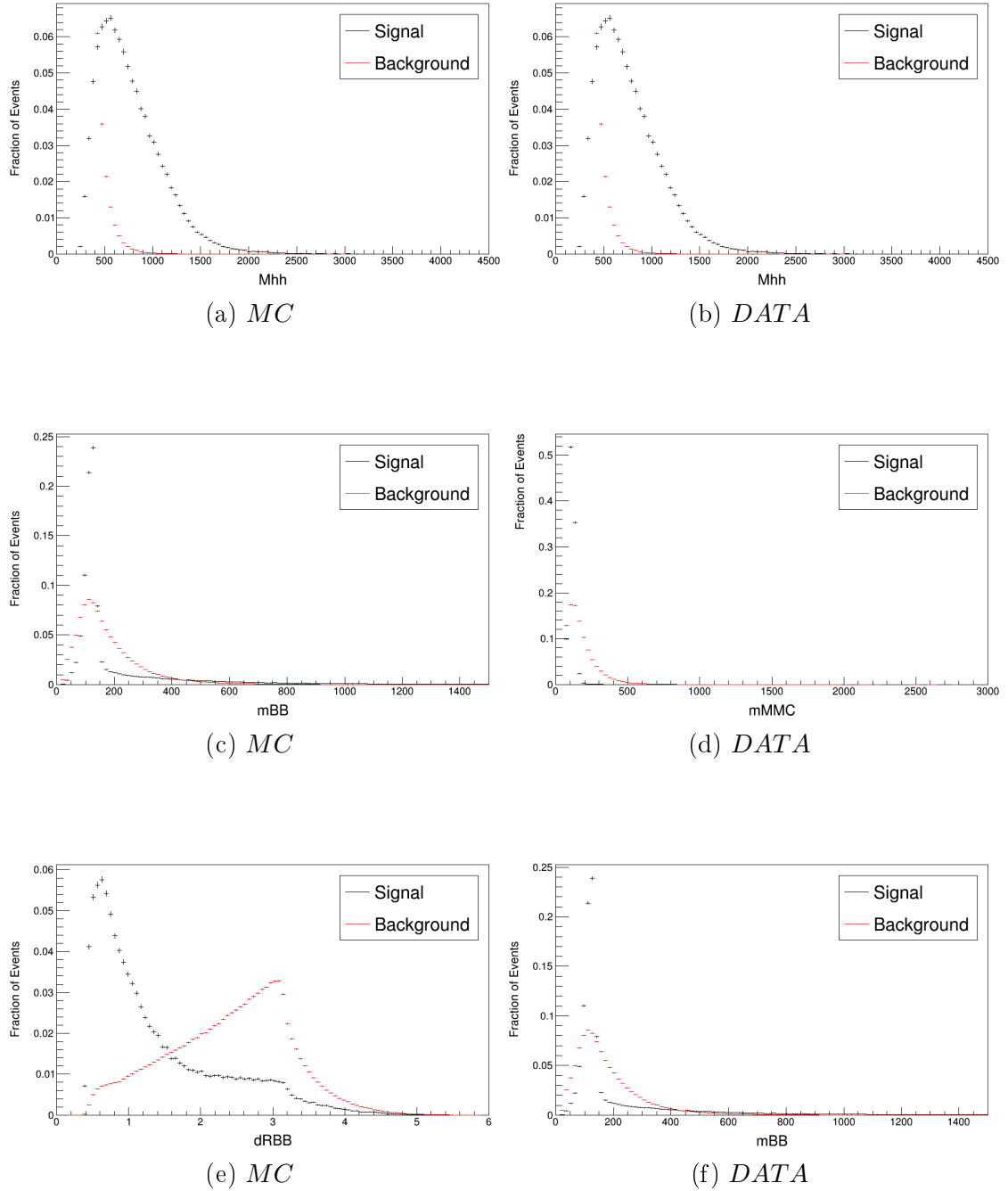


Figure 5.13: (a) MC-Input Variables (2017) and (b) DATA-Input Variables (2017)

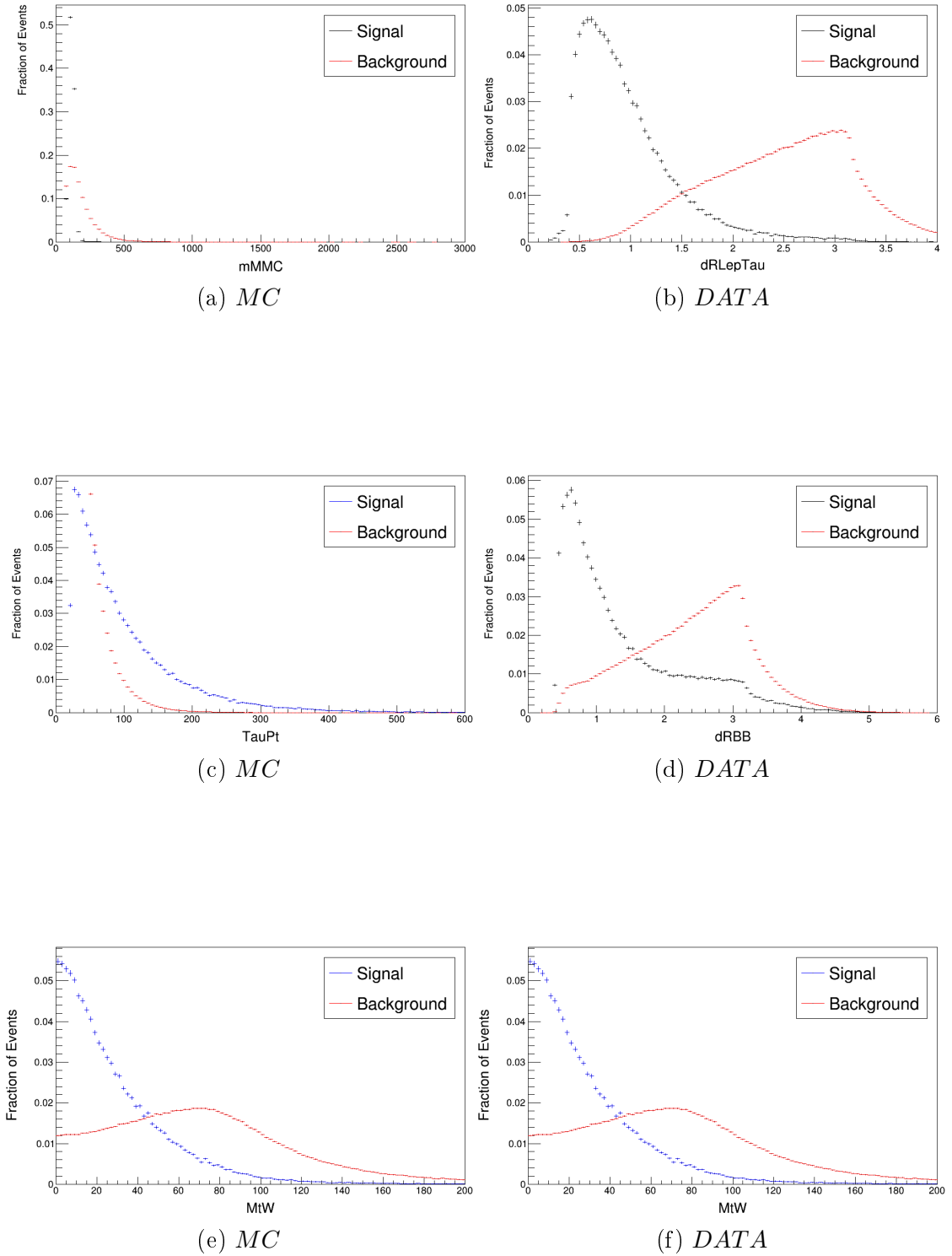


Figure 5.14: (a) MC-Input Variables (2017) and (b) DATA-Input Variables (2017)

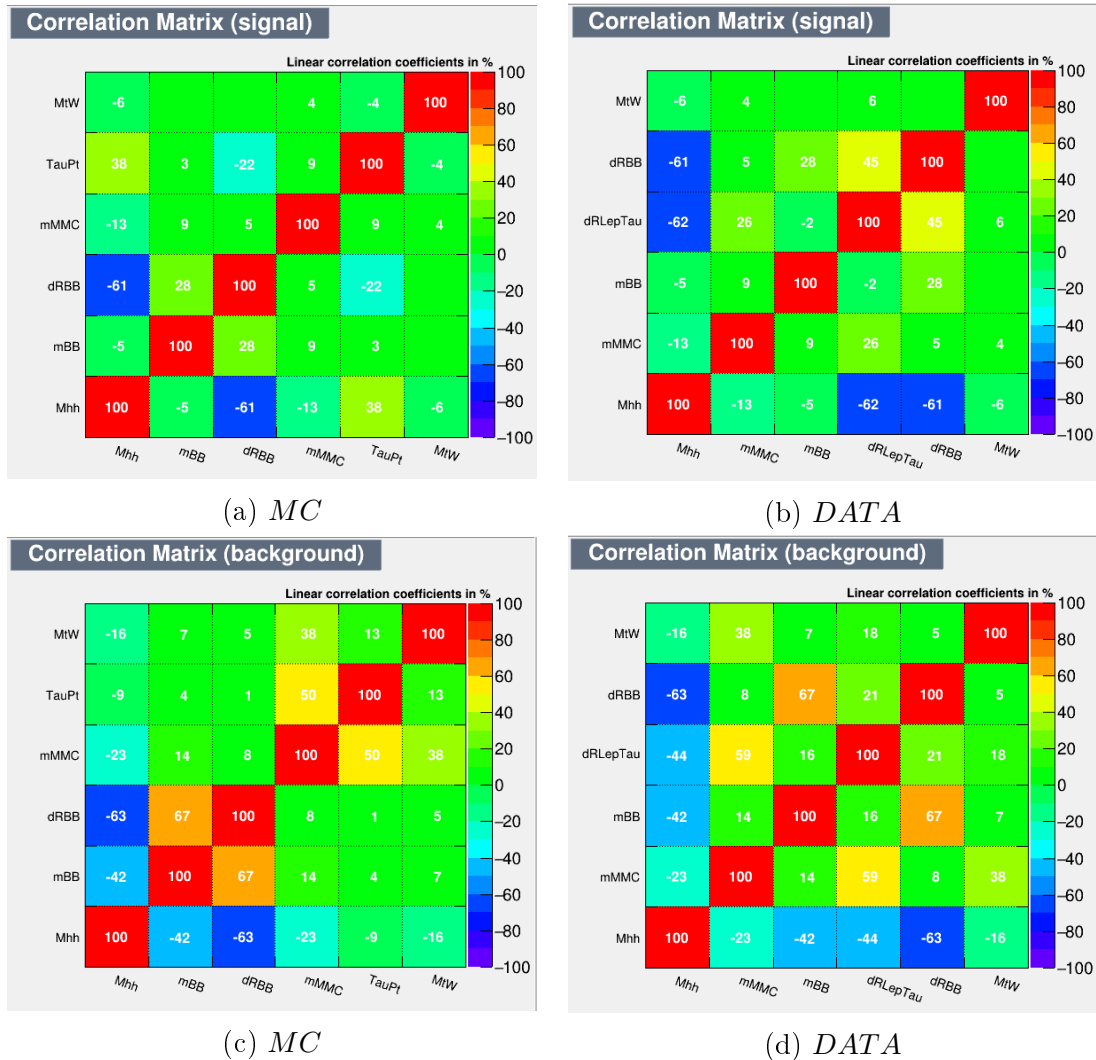


Figure 5.15: (a) Correlation matrix MC and (b) Correlation matrix DATA

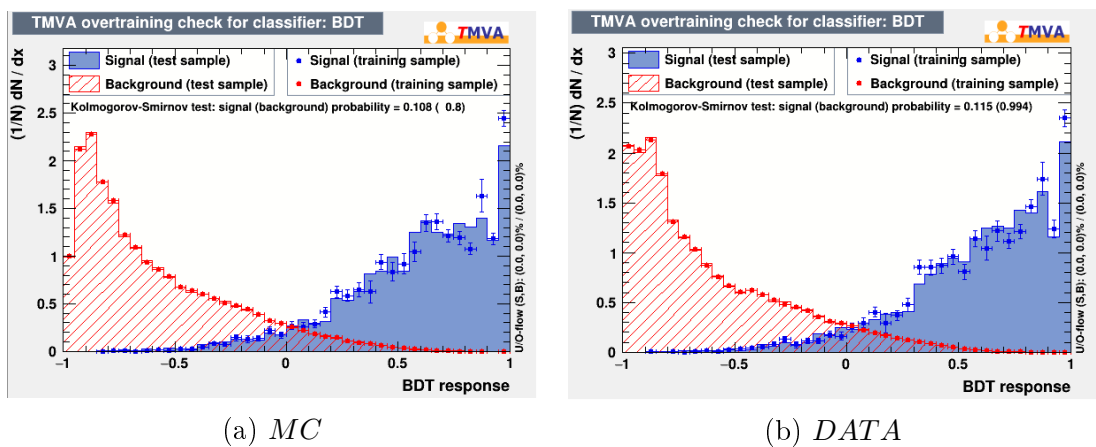


Figure 5.16: (a) MC Classifier (2017) and (b) DATA Classifier (2017)

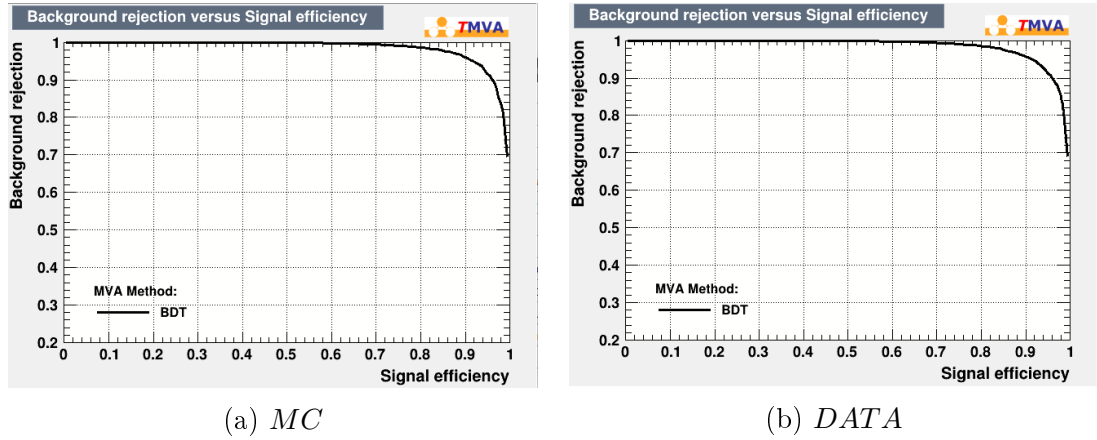


Figure 5.17: (a) ROC curve (2017) and (b) ROC curve (2017)

5.4.3 Period 2018

For the period of 2018, I've to make comparison plots for MC and DATA at integrated luminosity of 60 fb^{-1} and their overlap plots Figure 5.18, 5.19 and 5.20. Correlation between variables for signal and background in the respective of MC and DATA Figure 5.21, and 5.22. BDT classification for MC and DATA in Figure 5.23 and ROC curve Figure 5.24.

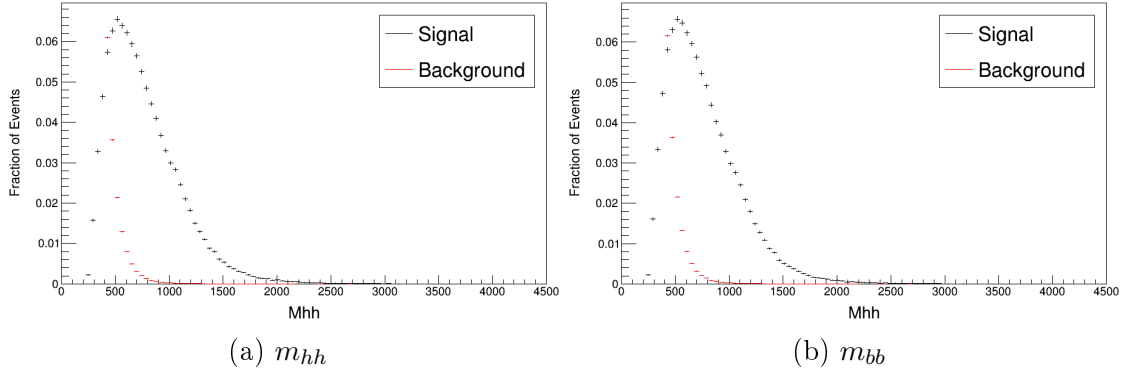


Figure 5.18: (a) MC-Input Variables (2018) and (b) DATA-Input Variables (2018)

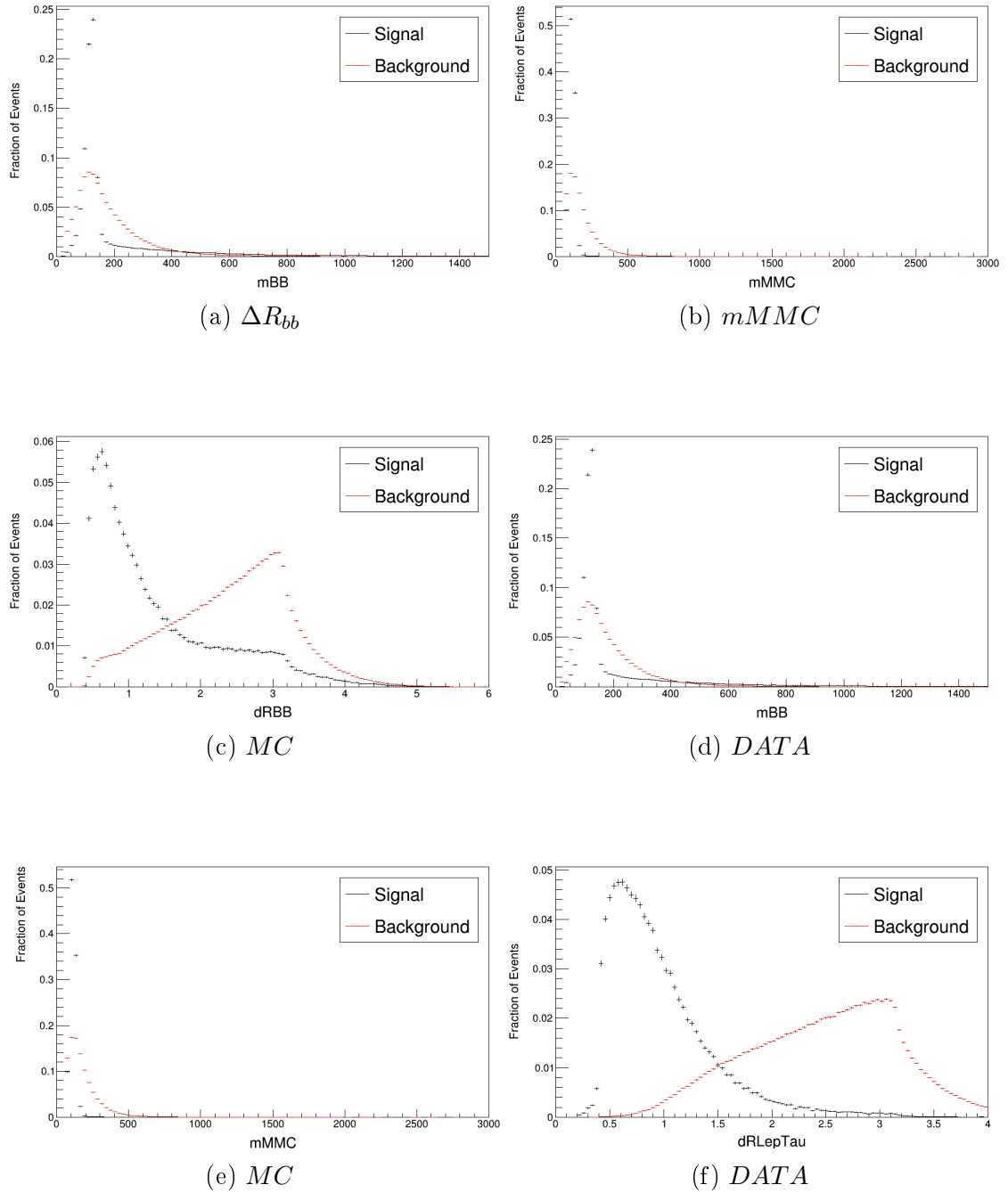


Figure 5.19: (a) MC-Input Variables (2018) and (b) DATA-Input Variables (2018)

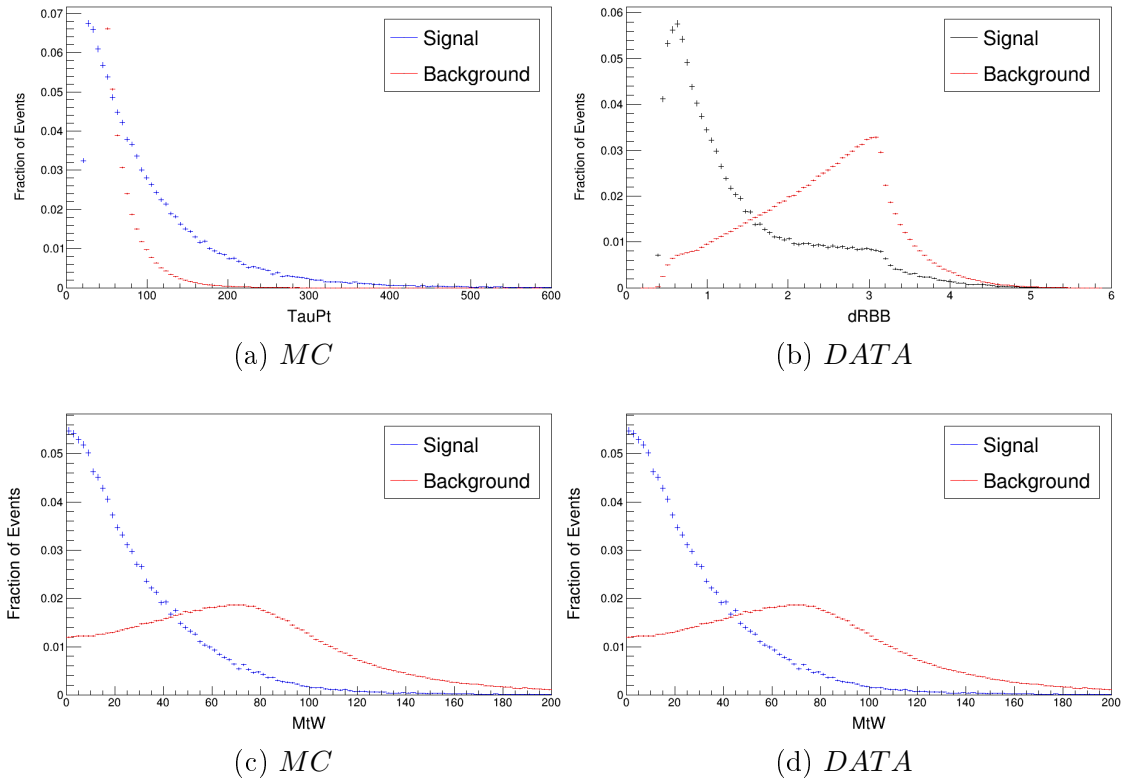


Figure 5.20: (a) MC-Input Variables (2018) and (b) DATA-Input Variables (2018)

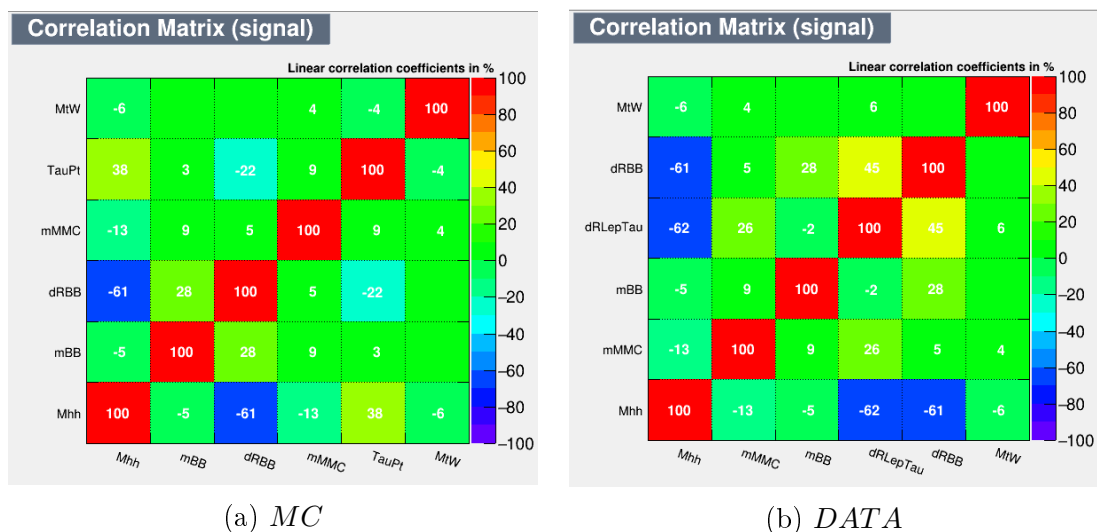


Figure 5.21: (a) Correlation matrix MC and (b) Correlation matrix DATA

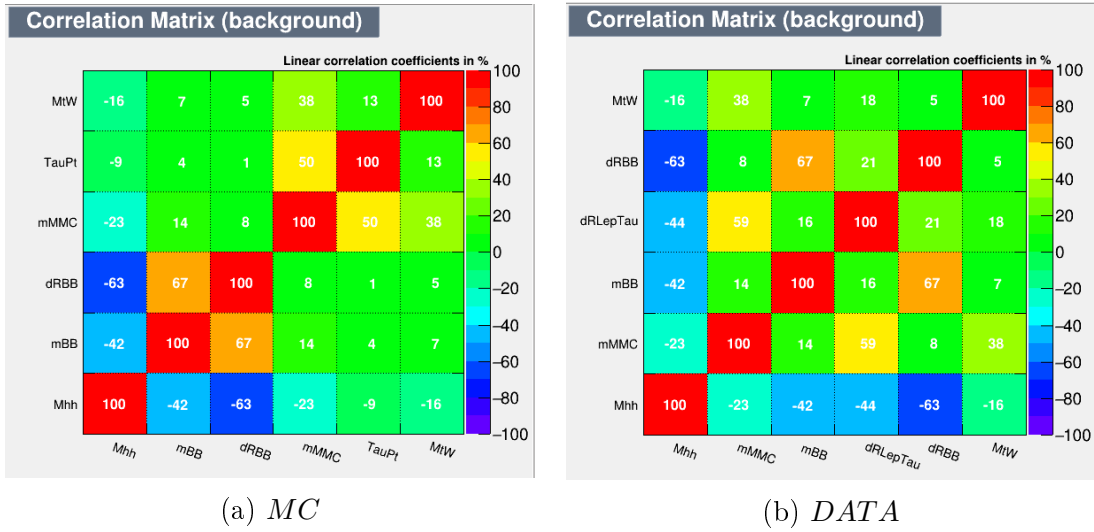


Figure 5.22: (a) Correlation matrix MC and (b) Correlation matrix DATA

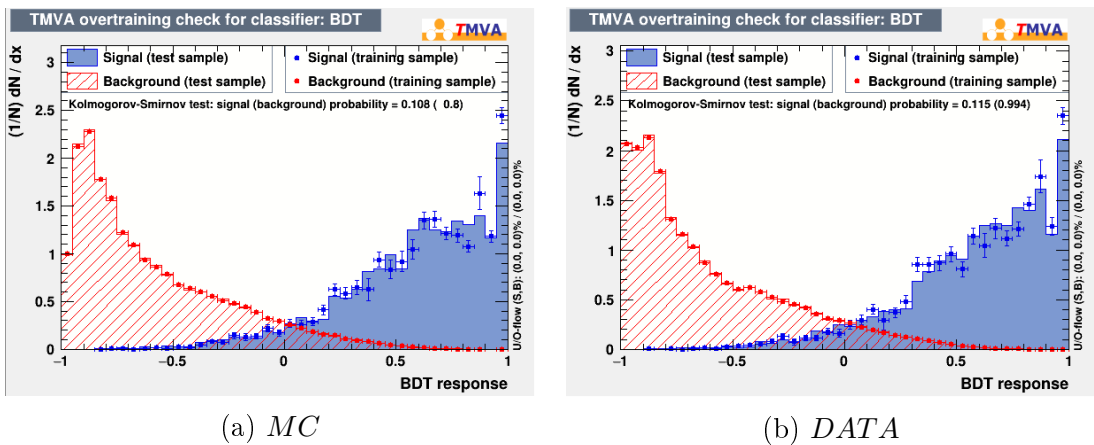


Figure 5.23: (a) MC Classifier (2017) and (b) DATA Classifier (2017)

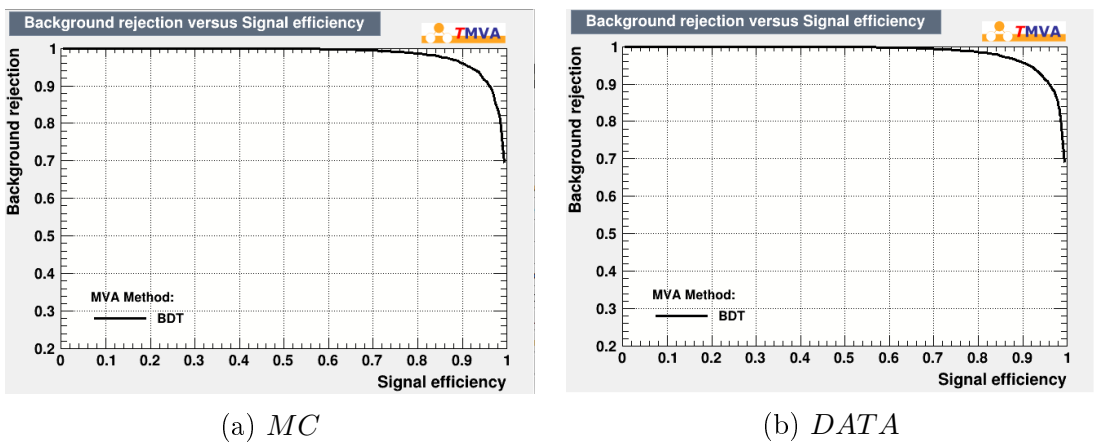


Figure 5.24: (a) ROC curve (2017) and (b) ROC curve (2017)

5.4.4 Period 2016-17

For the period of 2016-17, I've to make comparison plots for MC and DATA at integrated luminosity of 76 fb^{-1} and their overlap plots Figure 5.25, and 5.26. Correlation between variables for signal and background in the respective of MC and DATA Figure 5.27. BDT classification for MC and DATA in Figure 5.28 and ROC curve Figure 5.29.

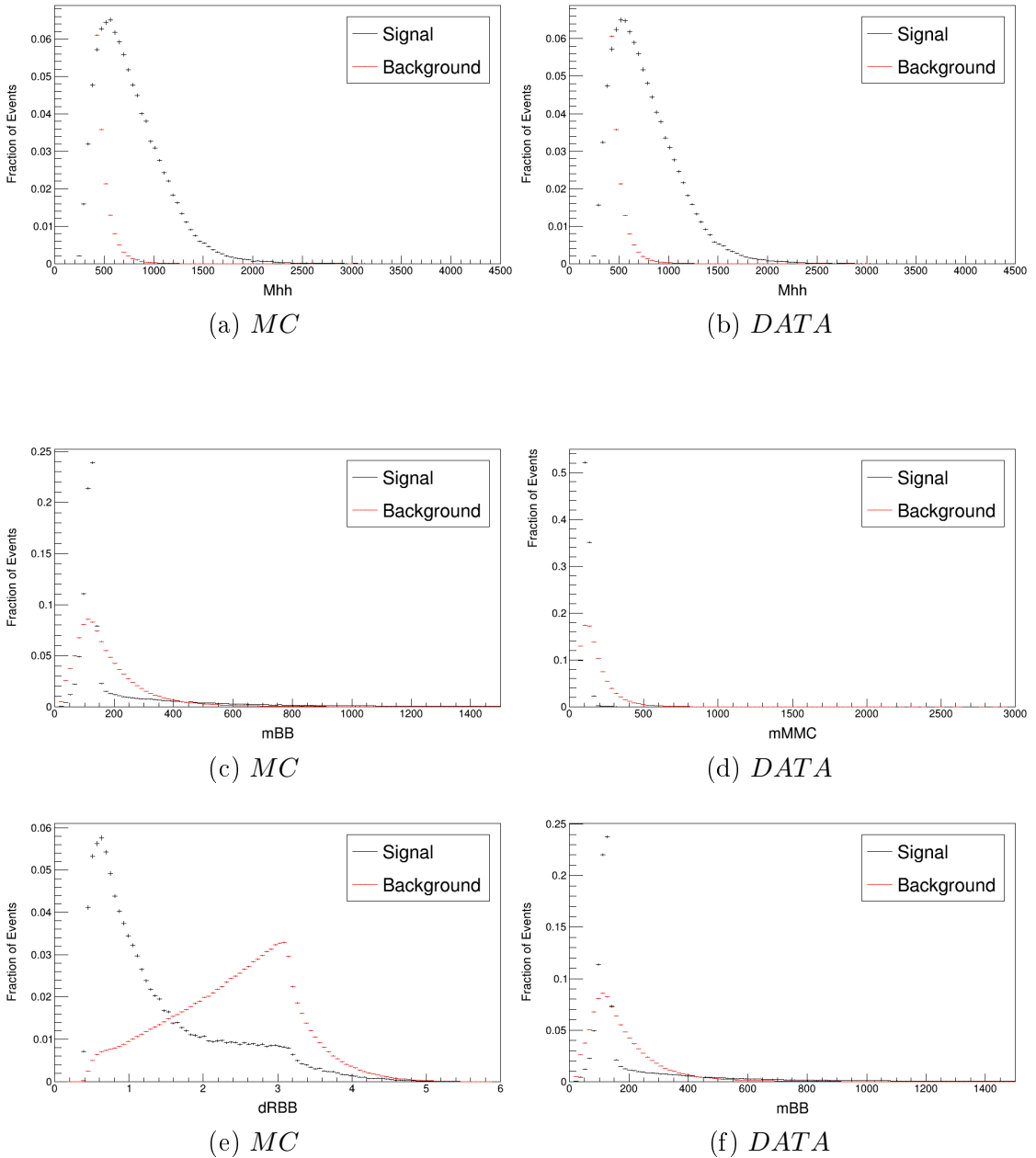


Figure 5.25: (a) MC-Input Variables (2016-17) and (b) DATA-Input Variables (2016-17)

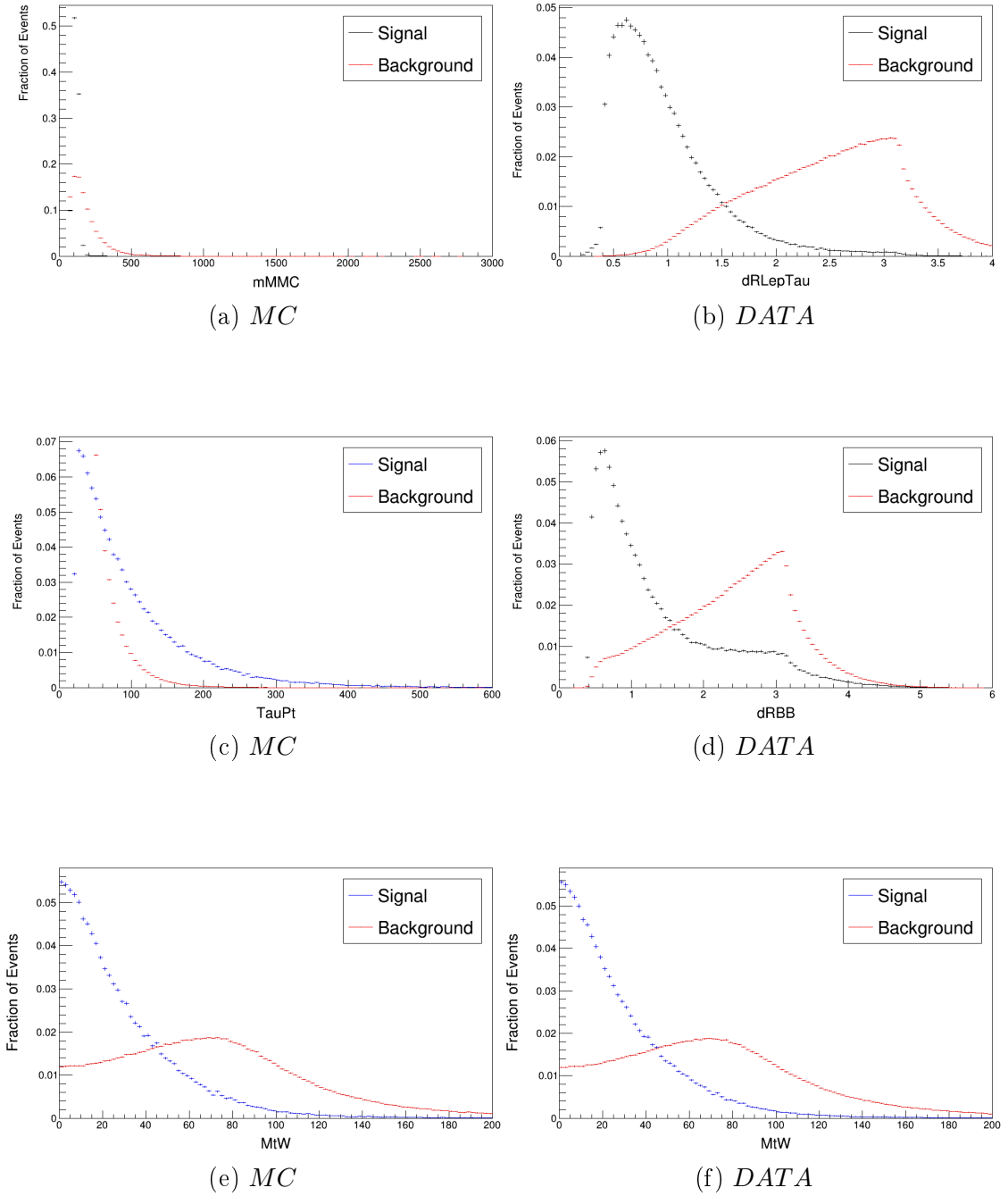


Figure 5.26: (a) MC-Input Variables (2016-17) and (b) DATA-Input Variables (2016-17)

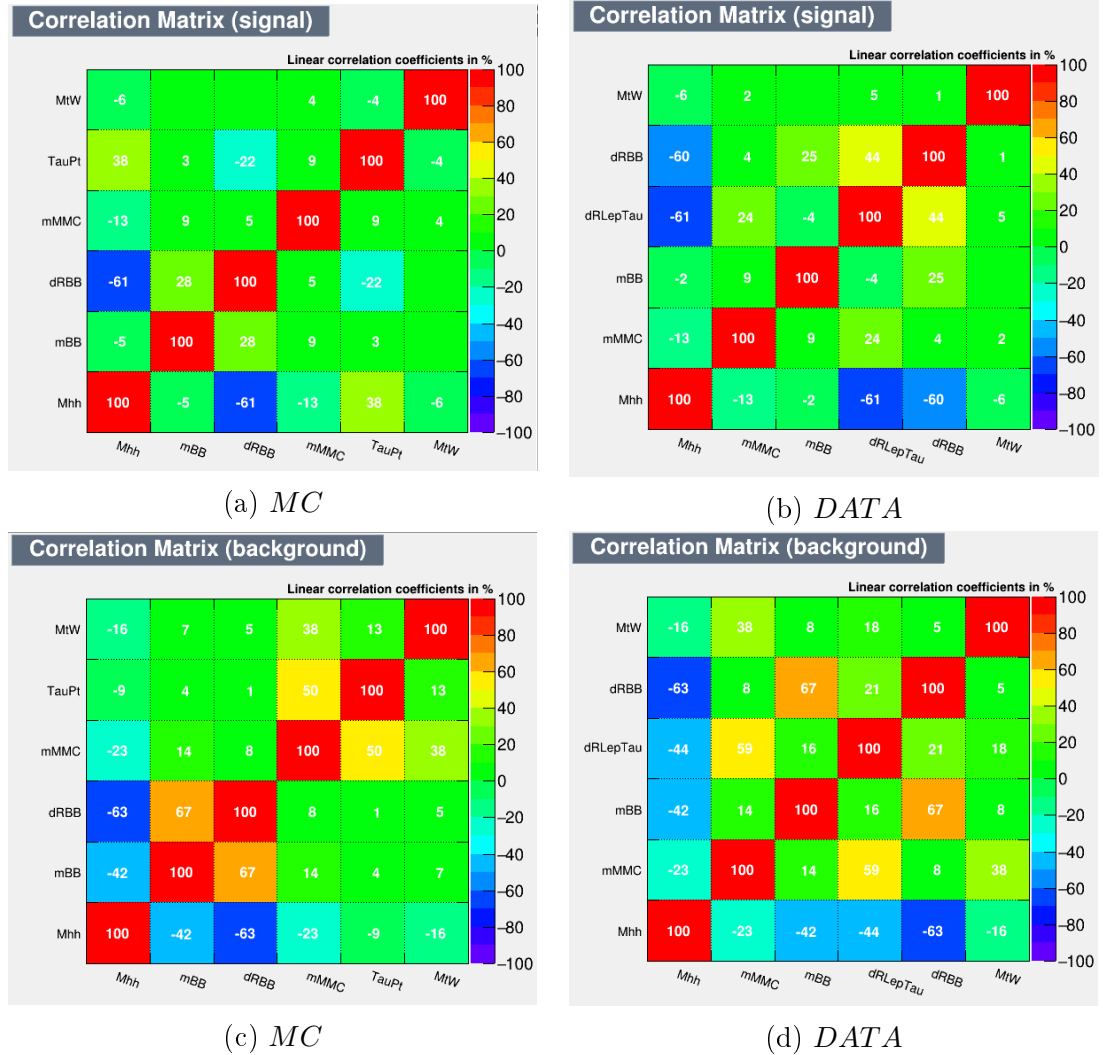


Figure 5.27: (a) Correlation matrix MC (2016-17) and (b) Correlation matrix DATA (2016-17)

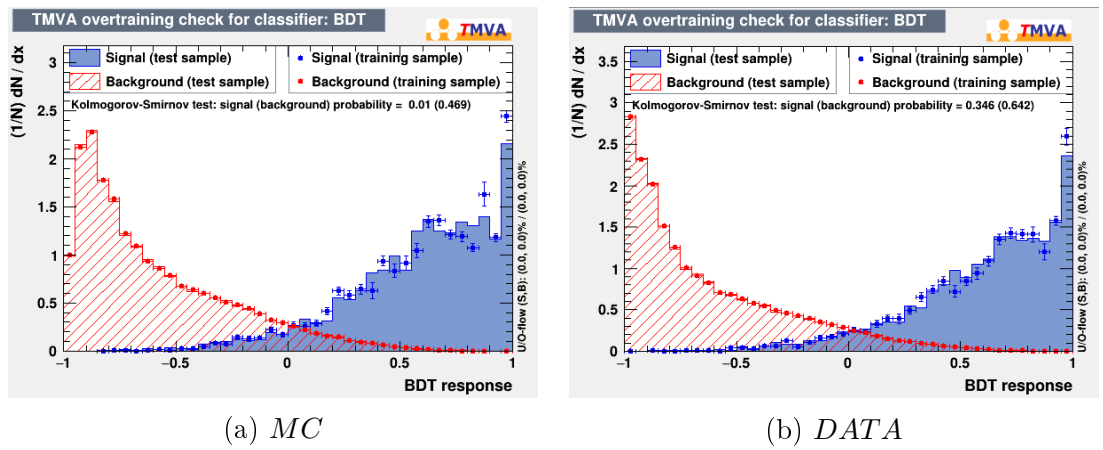


Figure 5.28: (a) MC Classifier (2016-17) and (b) DATA Classifier (2016-17)

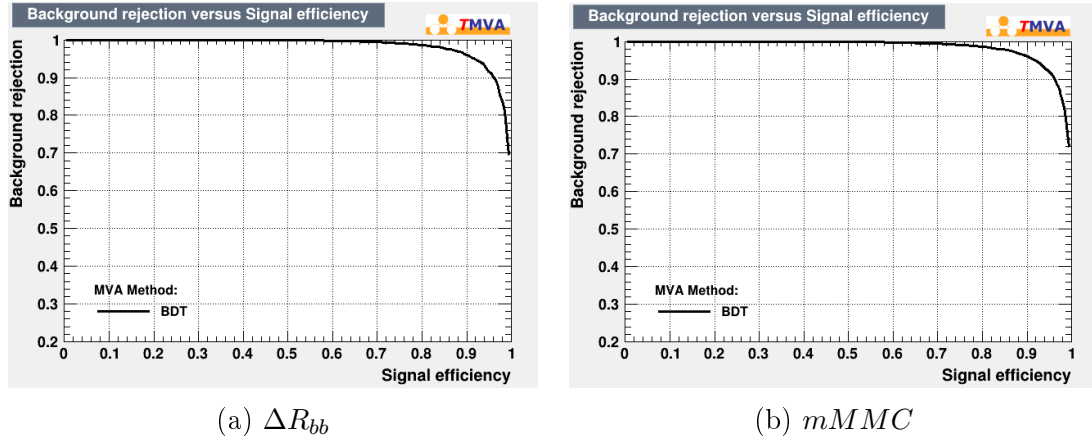


Figure 5.29: (a) ROC curve (2016-17) and (b) ROC curve (2016-17)

5.4.5 Period 2016-18

For the period of 2016-18, I've to make comparison plots for MC and DATA at integrated luminosity of 96 fb^{-1} and their overlap plots Figure 5.30, 5.31 and 5.32. Correlation between variables for signal and background in the respective of MC and DATA Figure 5.33, and 5.34. BDT classification for MC and DATA in Figure 5.35 and ROC curve Figure 5.36.

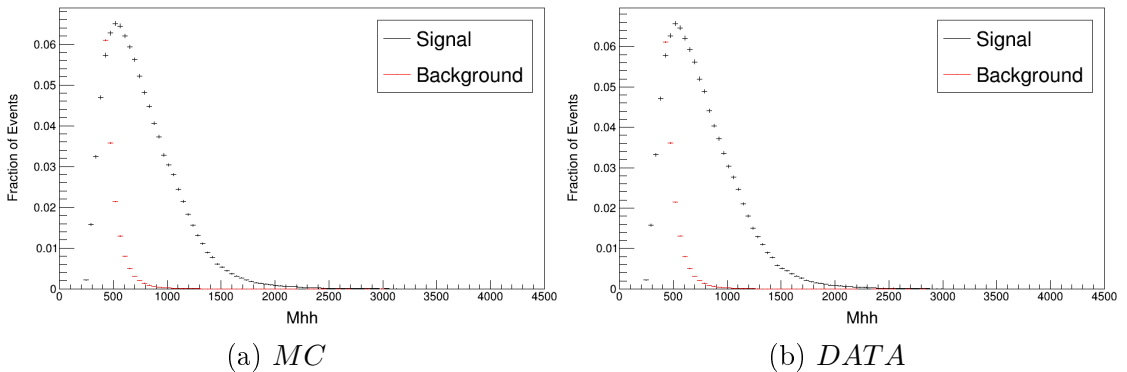


Figure 5.30: (a) MC-Input Variables (2016-18) and (b) DATA-Input Variables (2016-18)

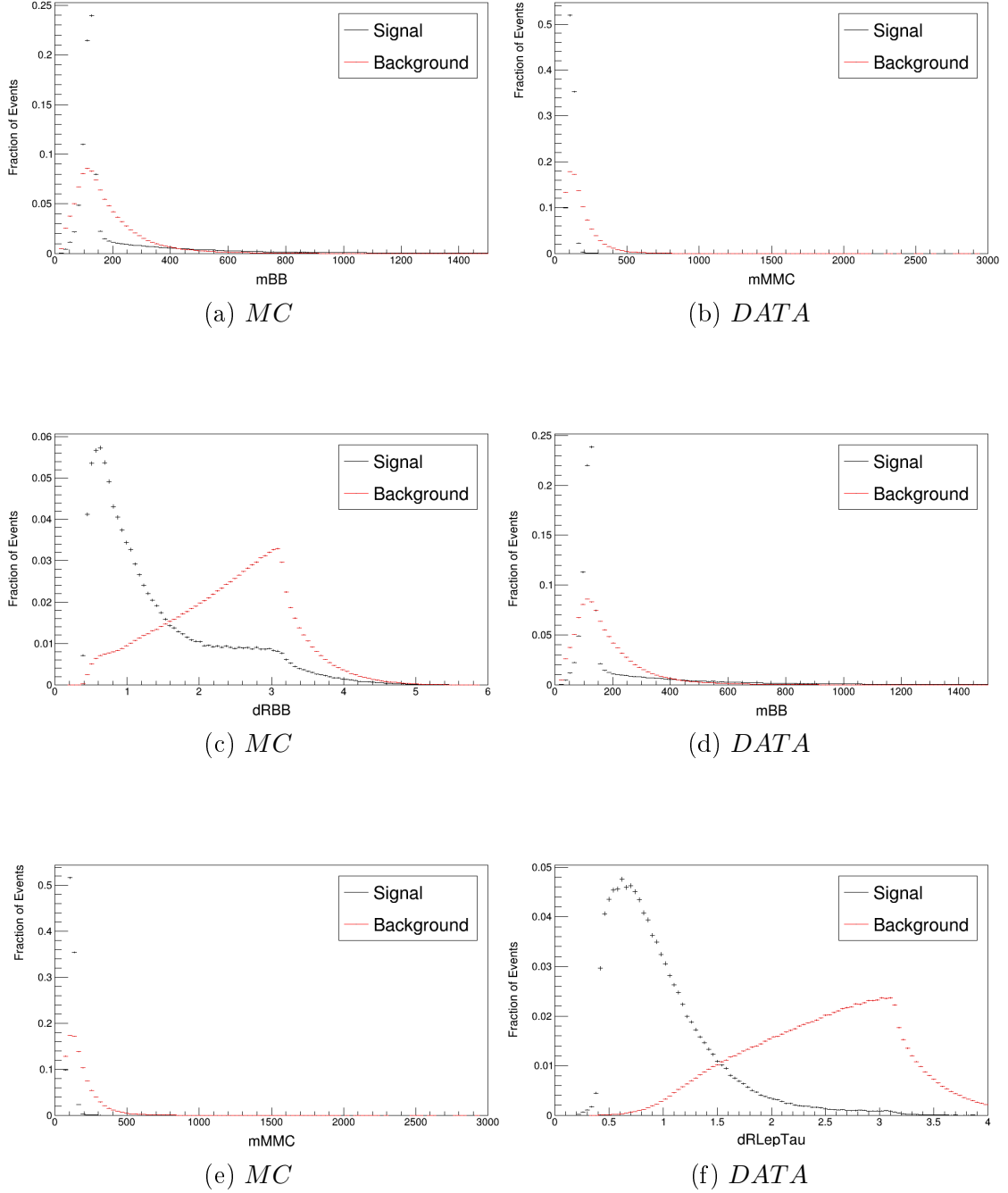


Figure 5.31: (a) MC-Input Variables (2016-18) and (b) DATA-Input Variables (2016-18)

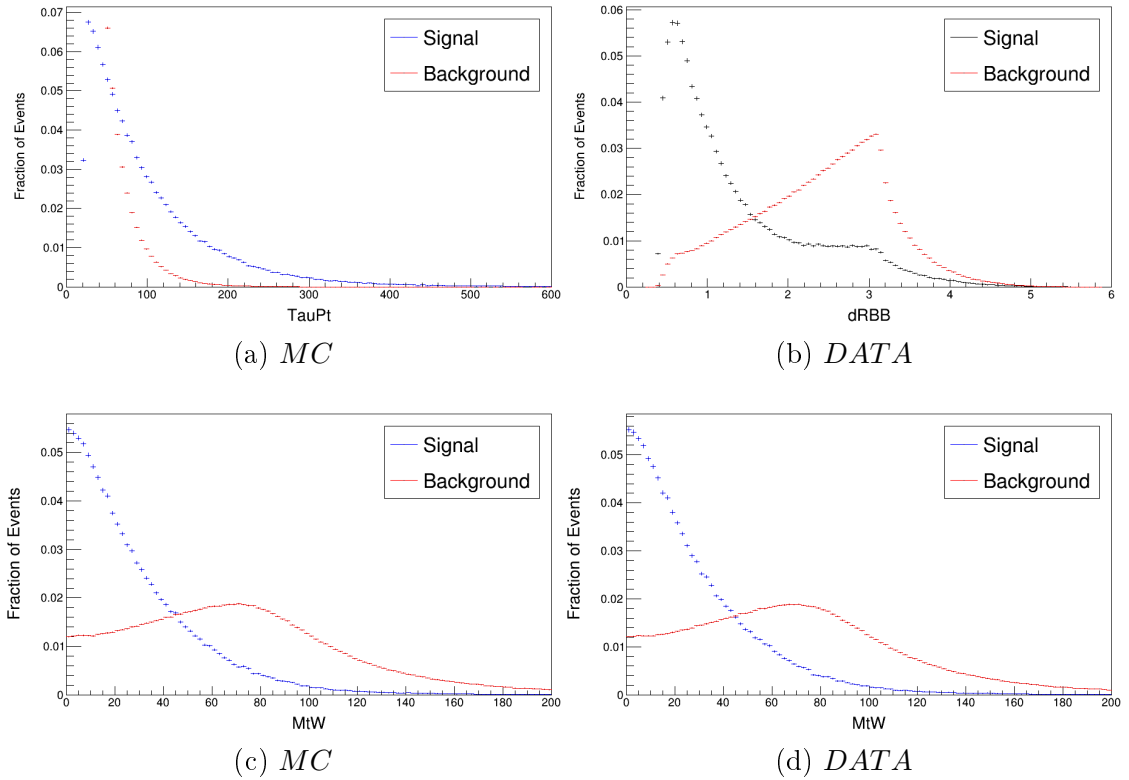


Figure 5.32: (a) MC-Input Variables (2016-18) and (b) DATA-Input Variables (2016-18)

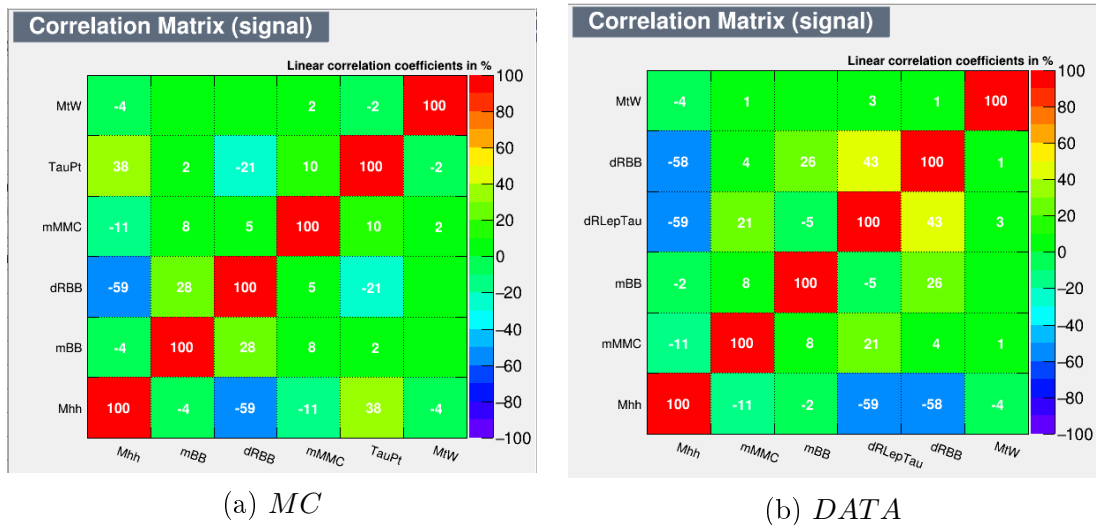


Figure 5.33: (a) Correlation matrix MC (2016-18) and (b) Correlation matrix DATA (2016-18)

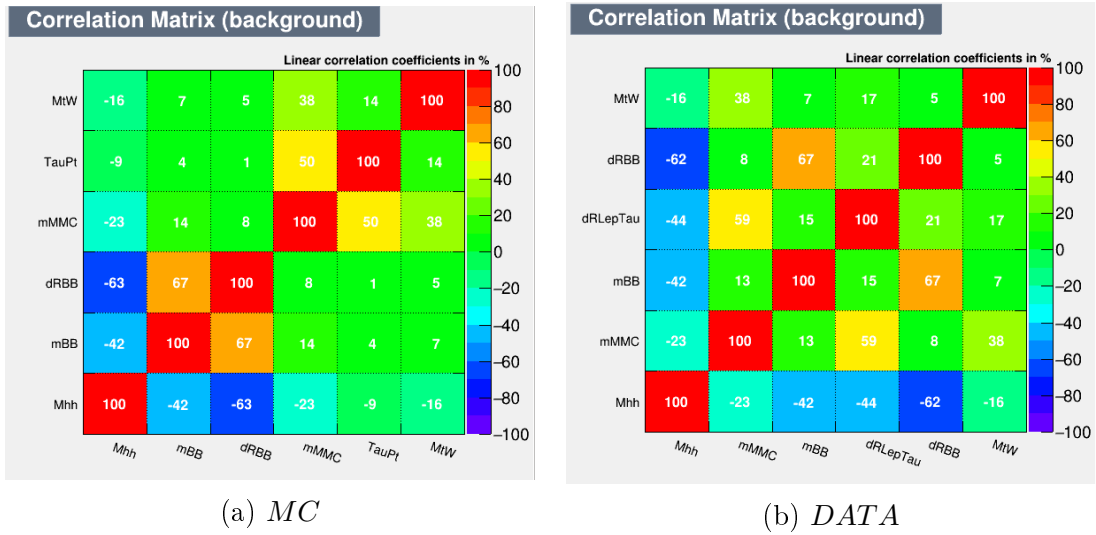


Figure 5.34: (a) Correlation matrix MC (2016-18) and (b) Correlation matrix DATA (2016-18)

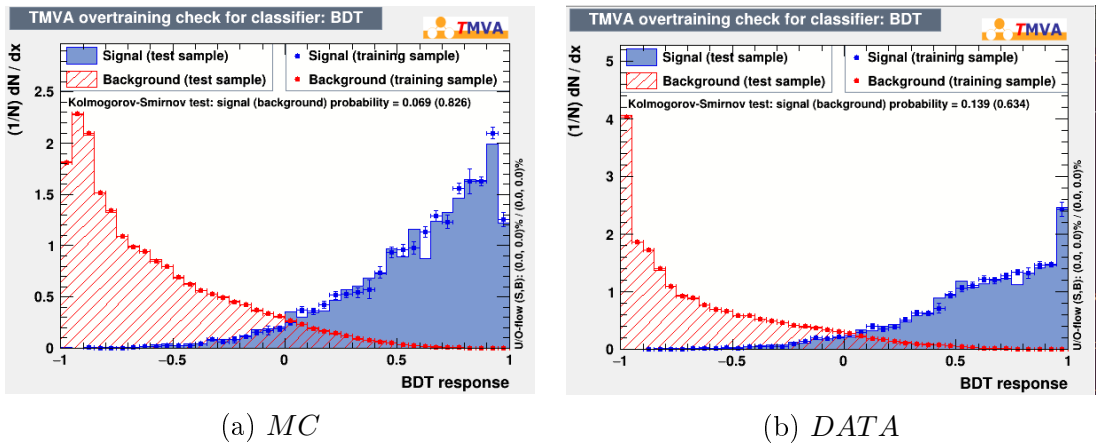


Figure 5.35: (a) MC Classifier (2016-18) and (b) DATA Classifier (2016-18)

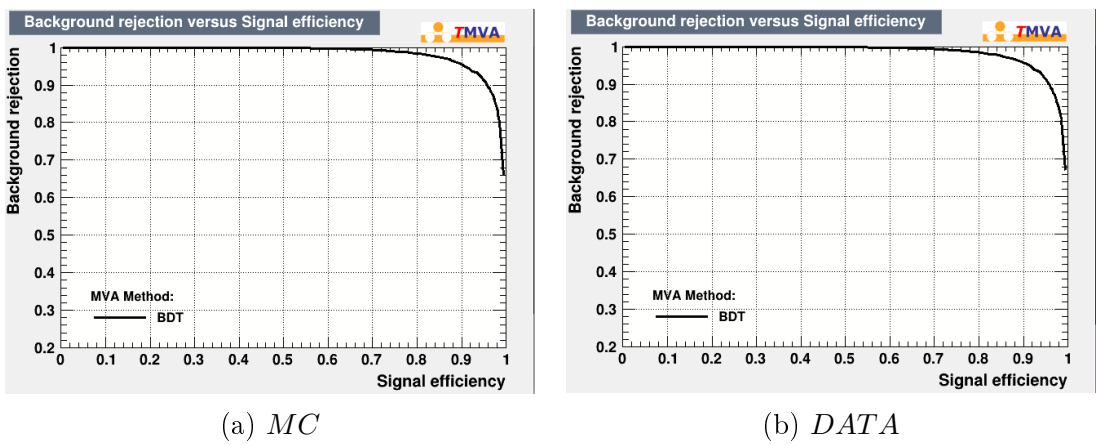


Figure 5.36: (a) ROC curve (2016-18) and (b) ROC curve (2016-18)

5.4.6 Period 2017-18

For the period of 2017-18, I've to make comparison plots for MC and DATA at integrated luminosity of 100 fb^{-1} and their overlap plots Figure 5.37, and 5.38. Correlation between variables for signal and background in the respective of MC and DATA Figure 5.39. BDT classification for MC and DATA in Figure 5.40 and ROC curve Figure 5.41.

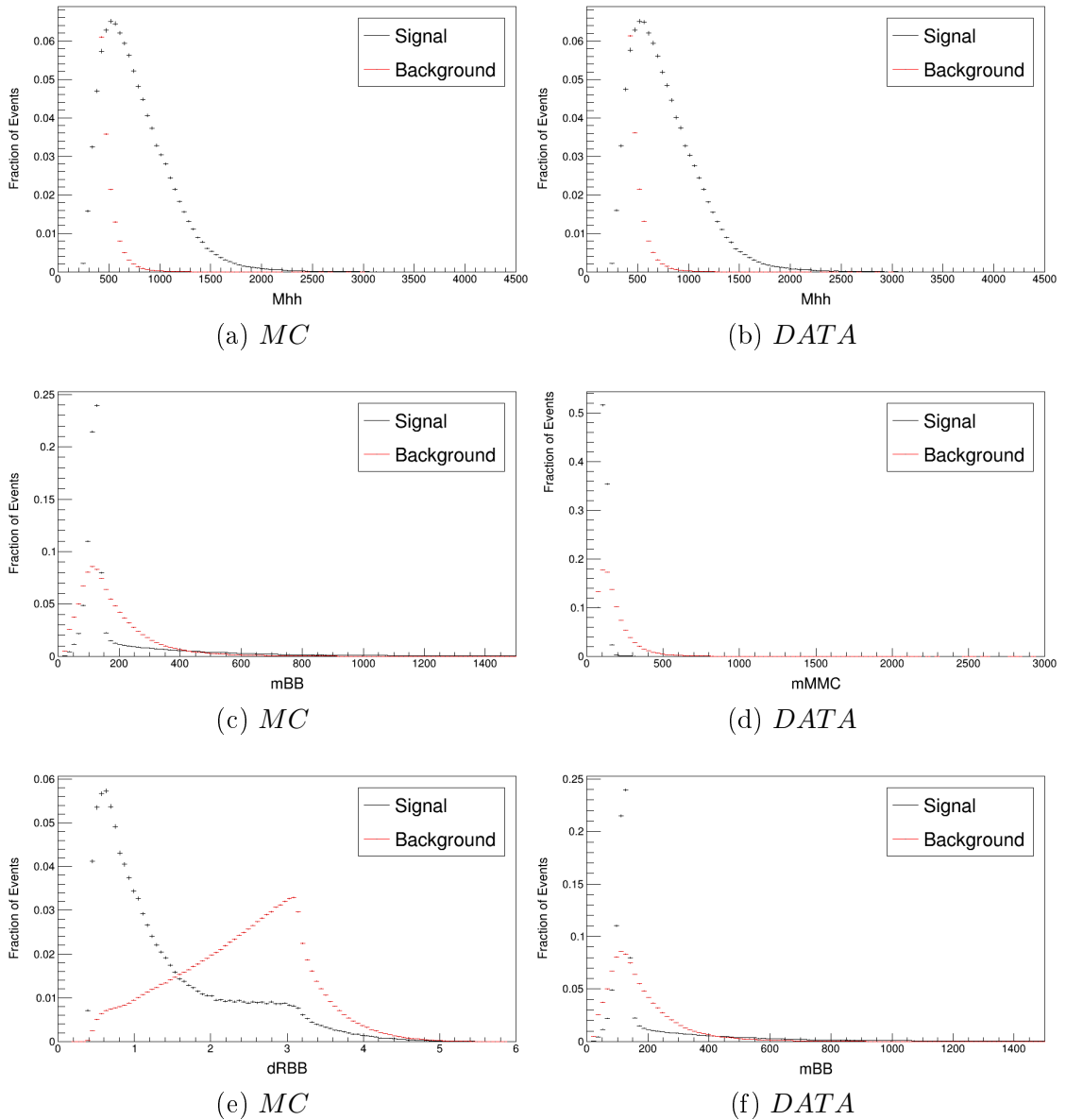


Figure 5.37: (a) MC-Input Variables (2017-18) and (b) DATA-Input Variables (2017-18)

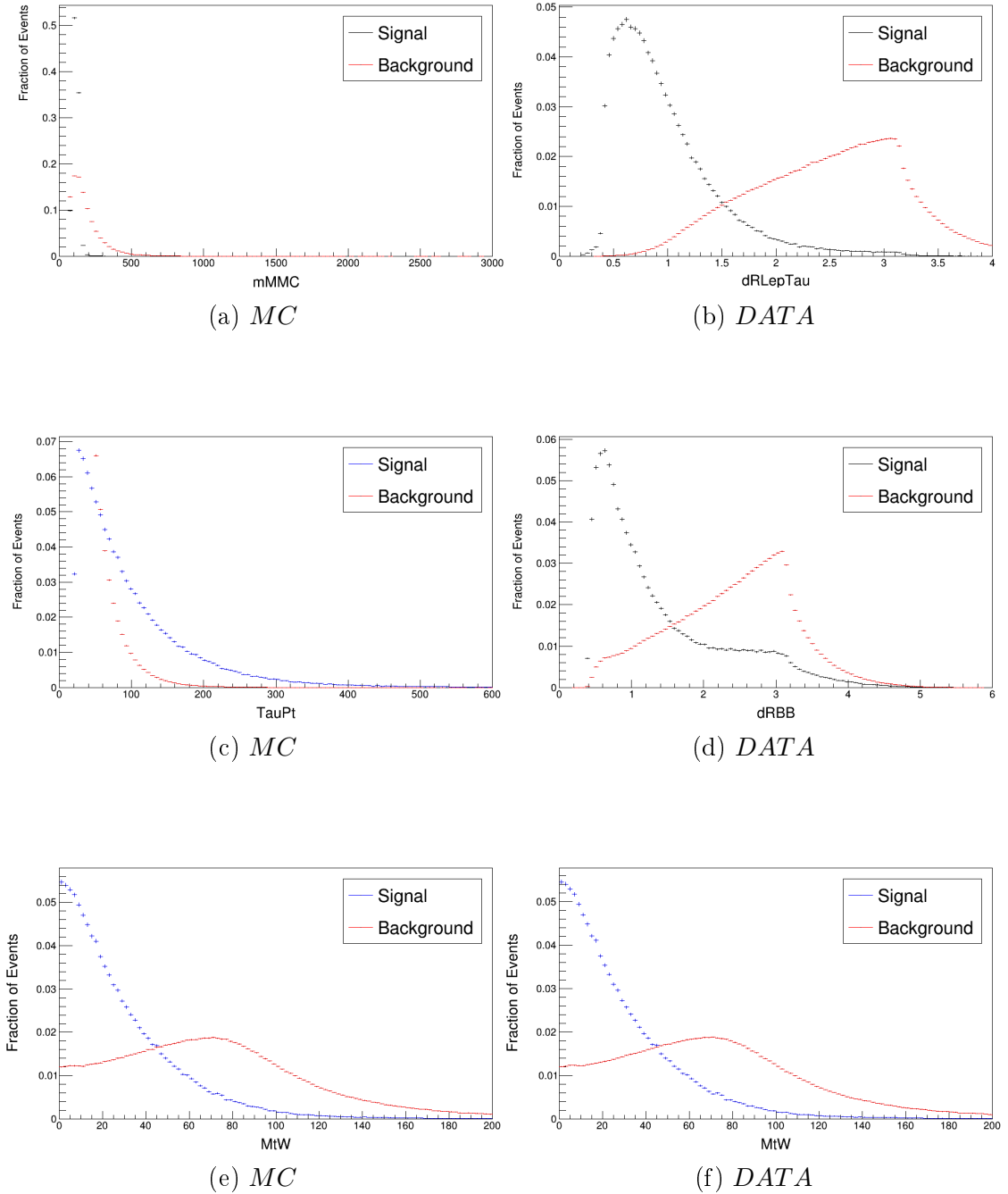


Figure 5.38: (a) MC-Input Variables (2017-18) and (b) DATA-Input Variables (2017-18)

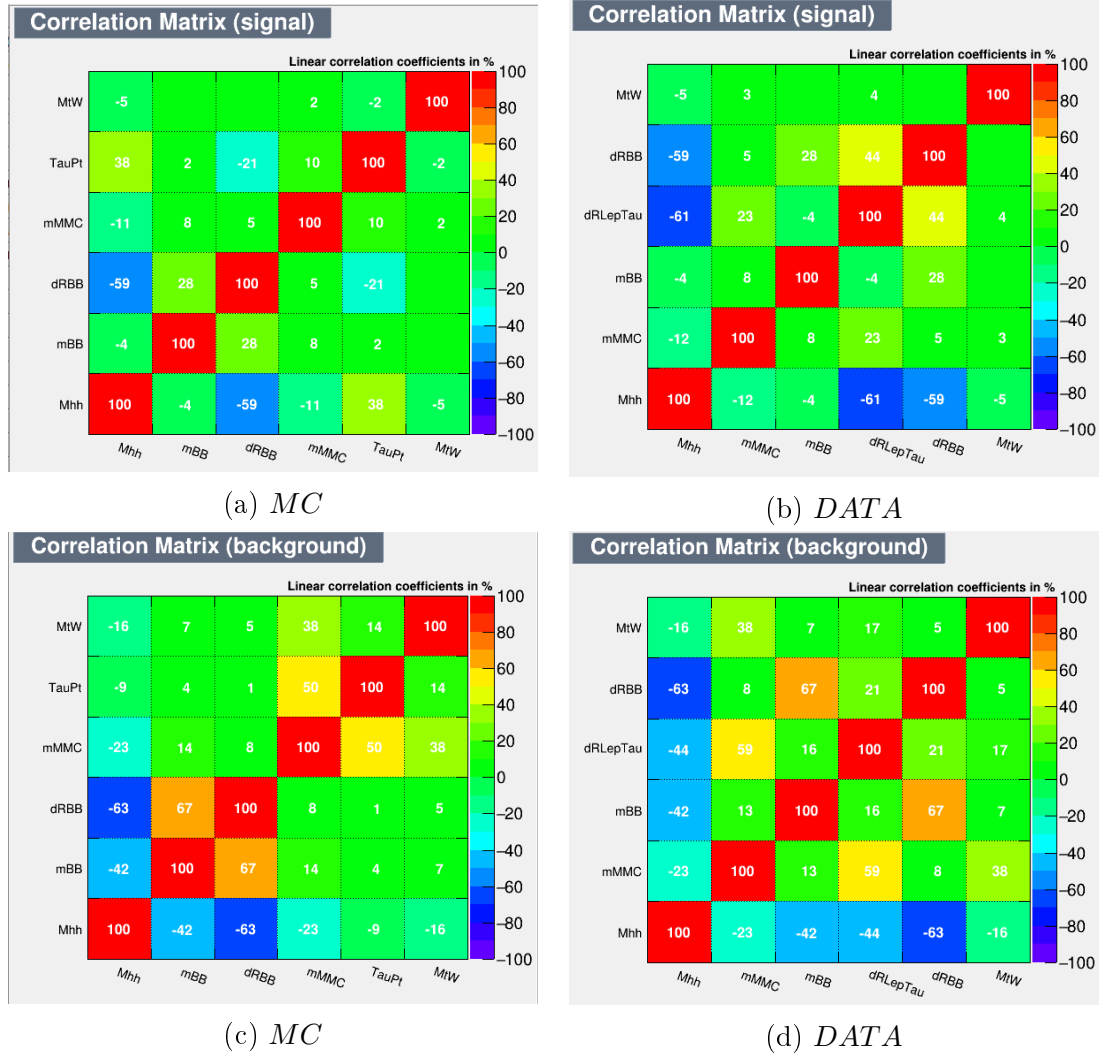


Figure 5.39: (a) Correlation matrix MC (2017-18) and (b) Correlation matrix DATA (2017-18)

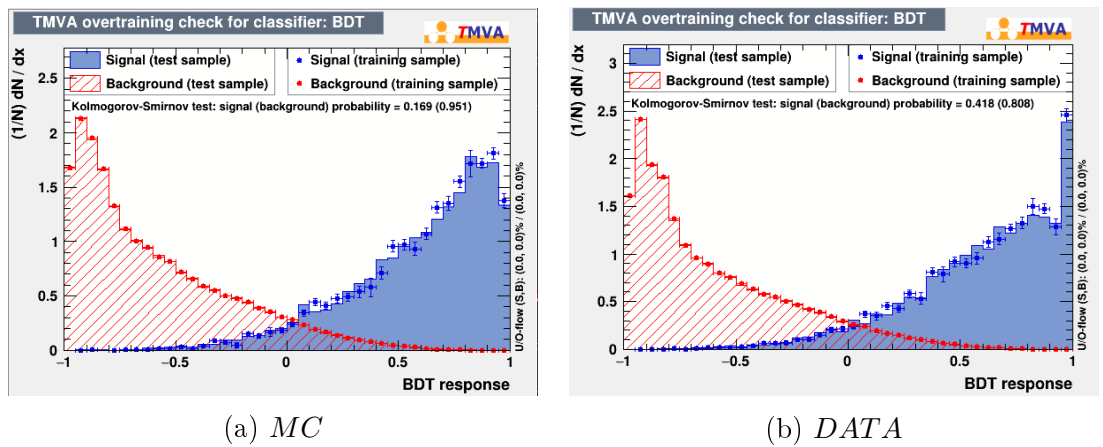


Figure 5.40: (a) MC Classifier (2017-18) and (b) DATA Classifier (2017-18)

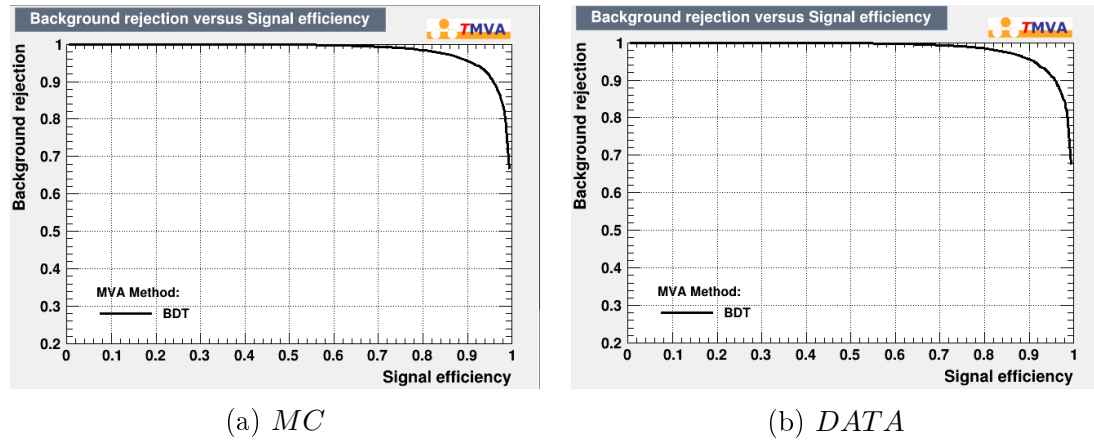


Figure 5.41: (a) ROC curve (2017-18) and (b) ROC curve (2017-18)

5.4.7 Period 2016-17-18

For the period of 2016-17-18, I've to make comparison plots for MC and DATA at integrated luminosity of 137 fb^{-1} and their overlap plots Figure 5.42, 5.43 and 5.44. Correlation between variables for signal and background in the respective of MC and DATA Figure 5.45, and 5.46. BDT classification for MC and DATA in Figure 5.47 and ROC curve Figure 5.48.

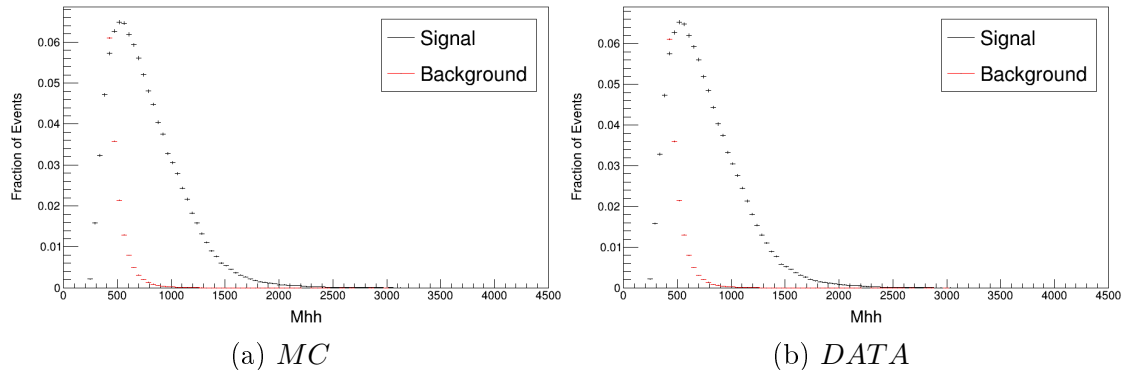


Figure 5.42: (a) MC-Input Variables (2016-17-18) and (b) DATA-Input Variables (2016-17-18)

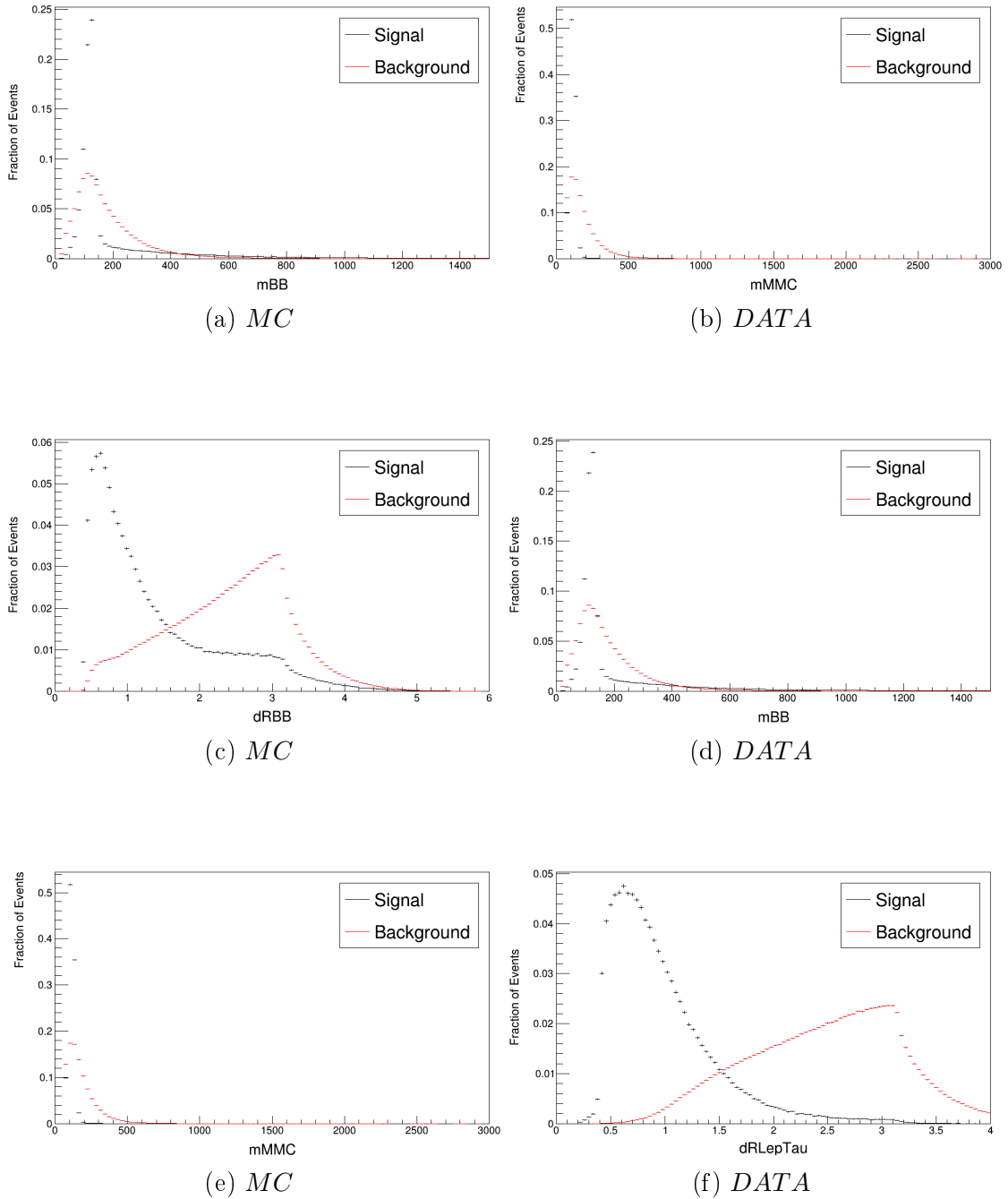


Figure 5.43: (a) MC-Input Variables (2016-17-18) and (b) DATA-Input Variables (2016-17-18)

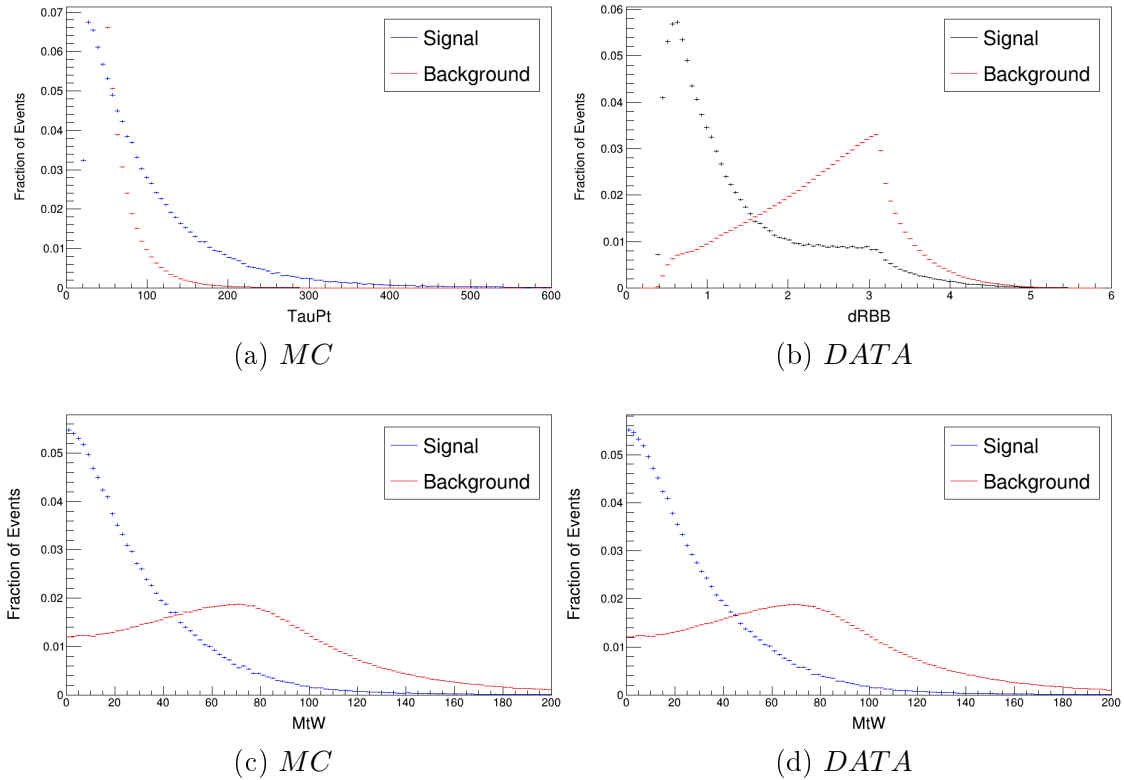


Figure 5.44: (a) MC-Input Variables (2016-17-18) and (b) DATA-Input Variables (2016-17-18)

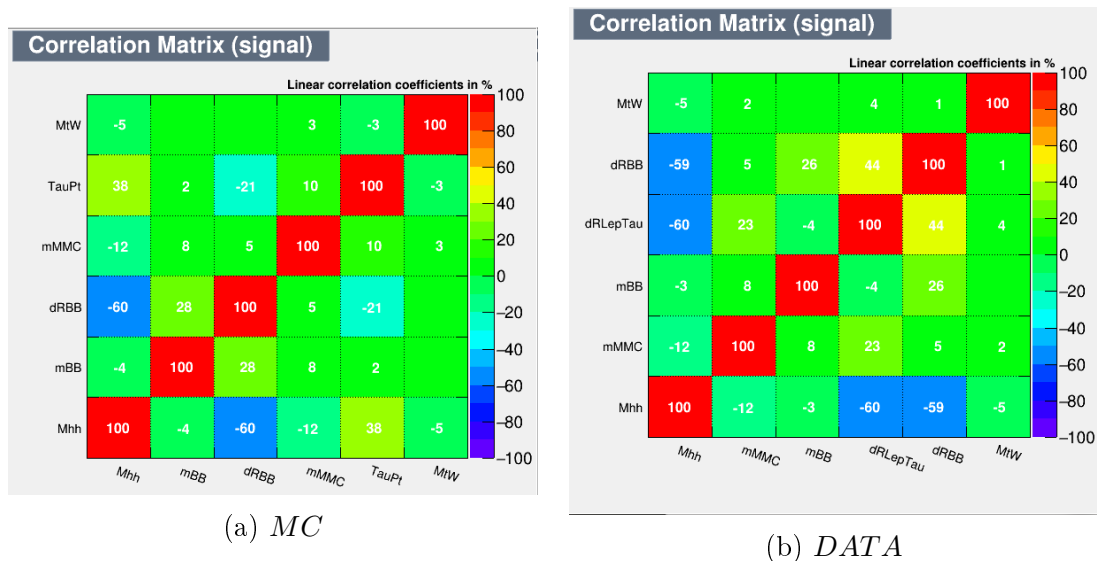


Figure 5.45: (a) Correlation matrix MC (2016-17-18) and (b) Correlation matrix DATA (2016-17-18)

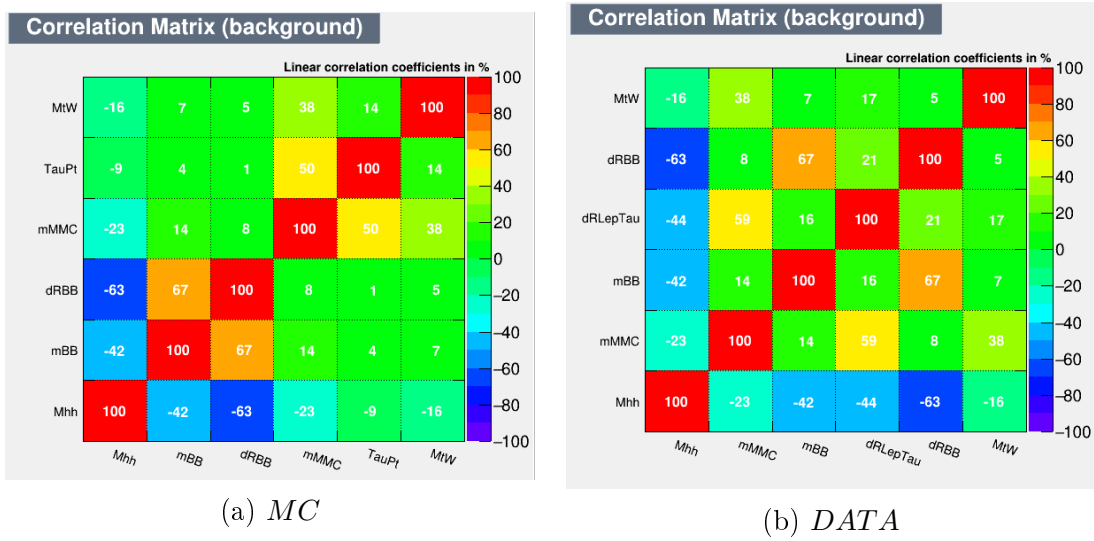


Figure 5.46: (a) Correlation matrix MC (2016-17-18) and (b) Correlation matrix DATA (2016-17-18)

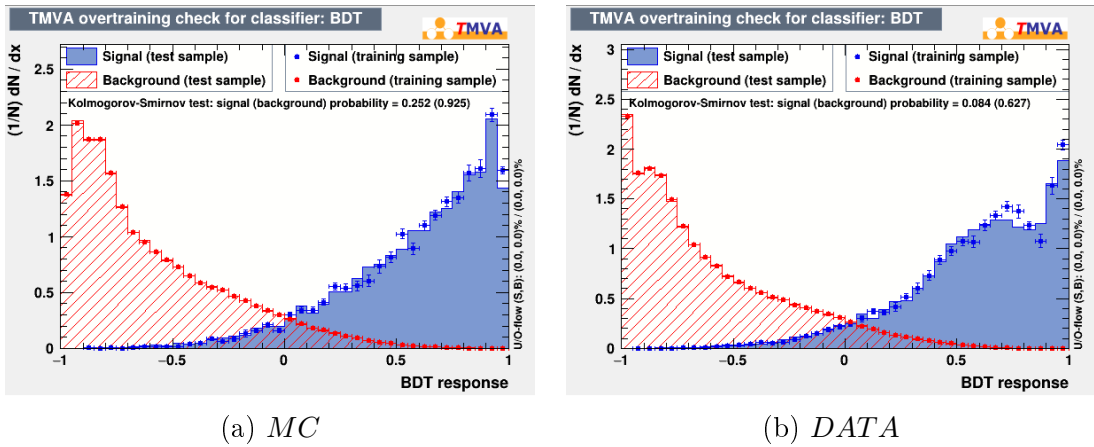


Figure 5.47: (a) MC Classifier (2016-17-18) and (b) DATA Classifier (2016-17-18)

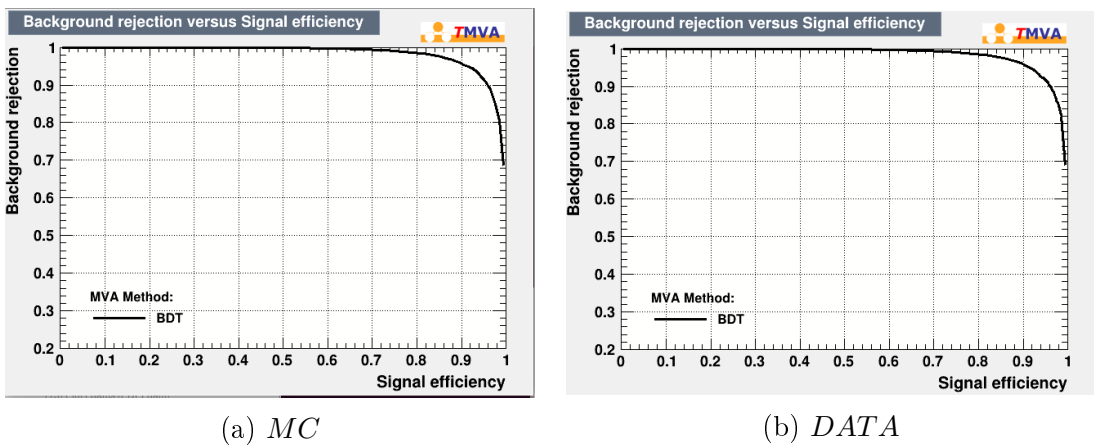


Figure 5.48: (a) ROC curve (2016-17-18) and (b) ROC curve (2016-17-18)

5.5 Data and MC Comparison

Data and MC comparison plot with their corresponding sensitivity at their respective luminosity Figure 5.49 & Figure 5.50 Data and MC agreement for period 2016 30%, 2017 15%, 2018 11%, 2016-17 21%, 2016-18 9%, 2017-18 2%, and 2016-17-18 is 4%.

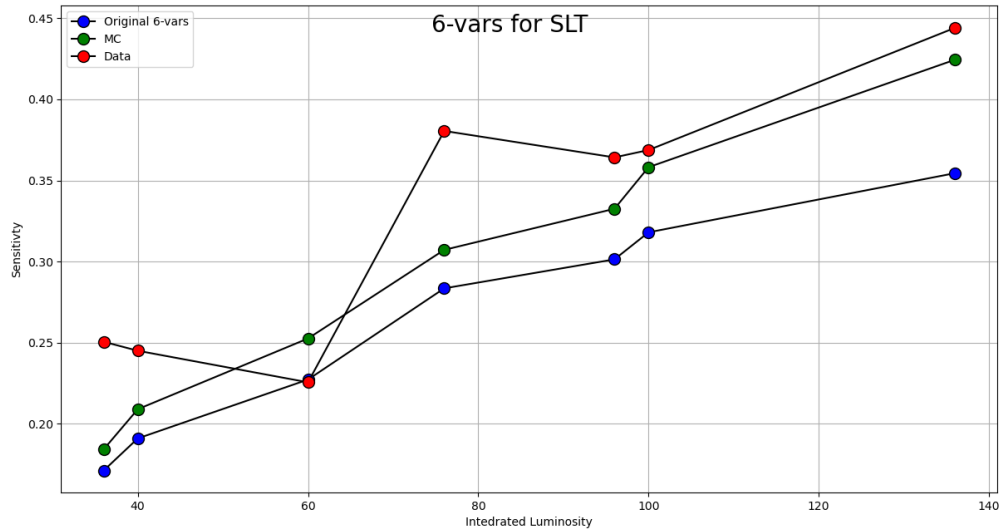


Figure 5.49: Data and MC comparison

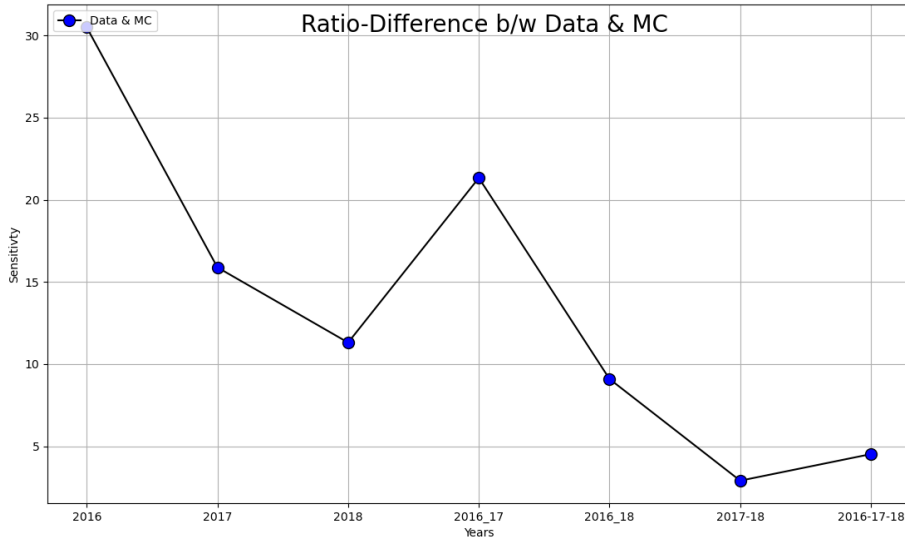


Figure 5.50: Ratio-Difference b/w Data & MC

The Figure 5.51 shows integrated luminosity for period of 2016-18.

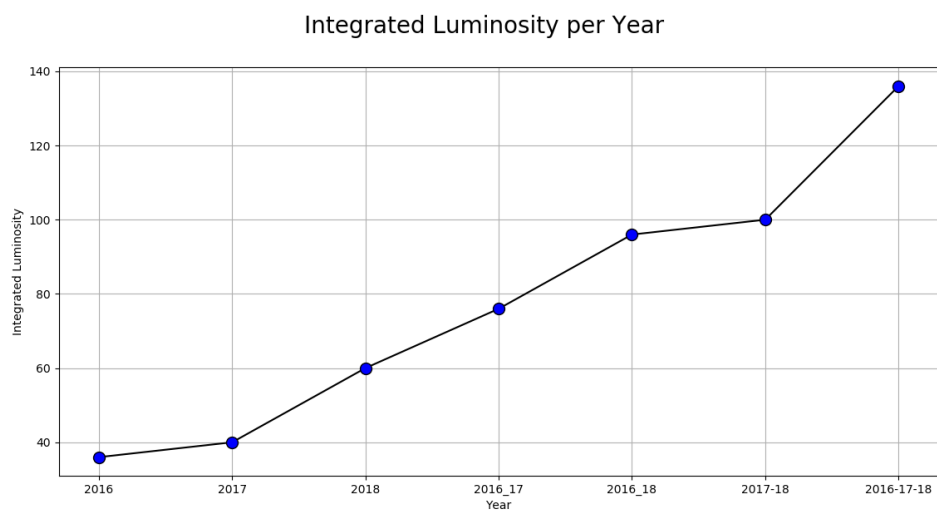


Figure 5.51: Integrated Luminosity

Chapter 6

Appendix $hh \rightarrow b\bar{b}\tau^+\tau^-$

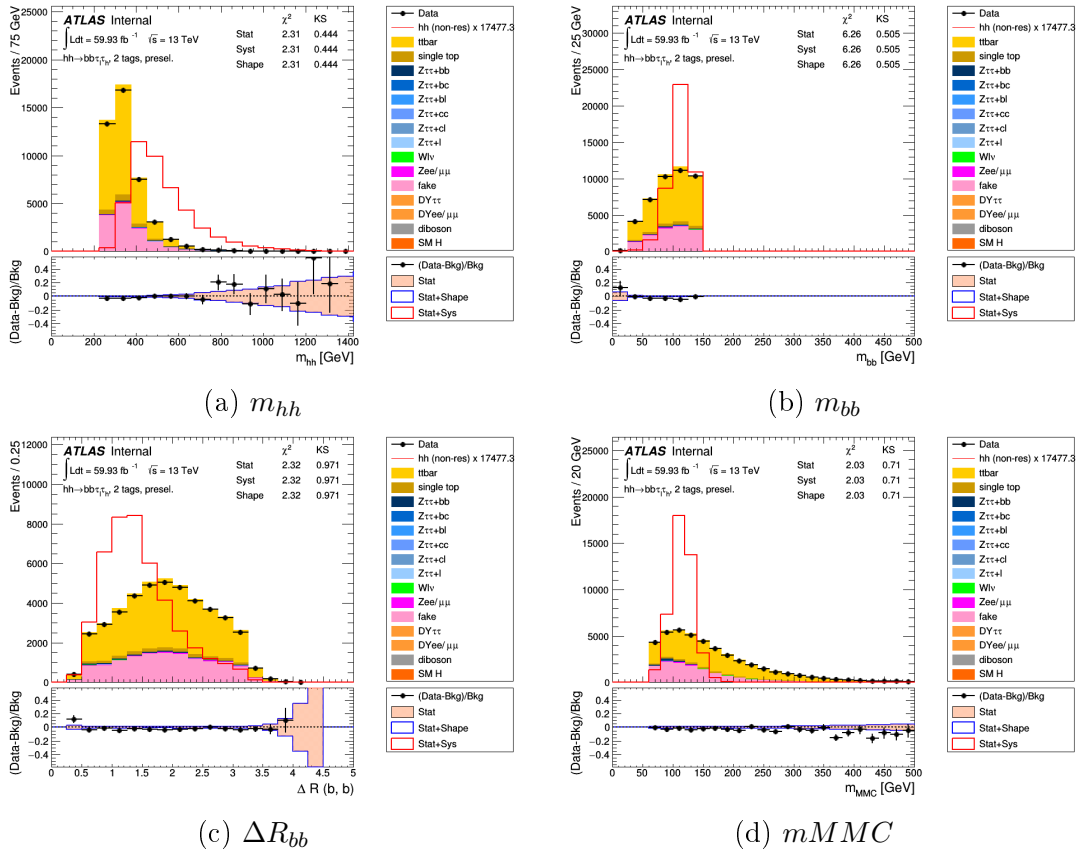


Figure 6.1

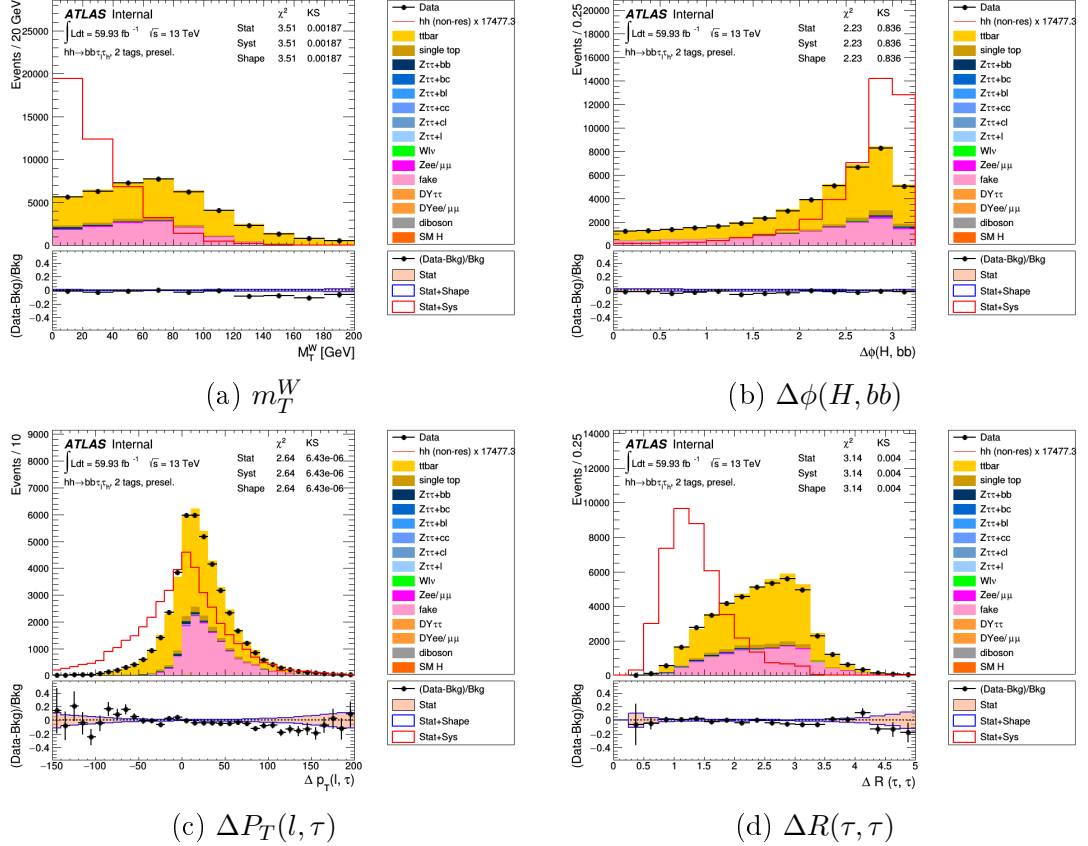
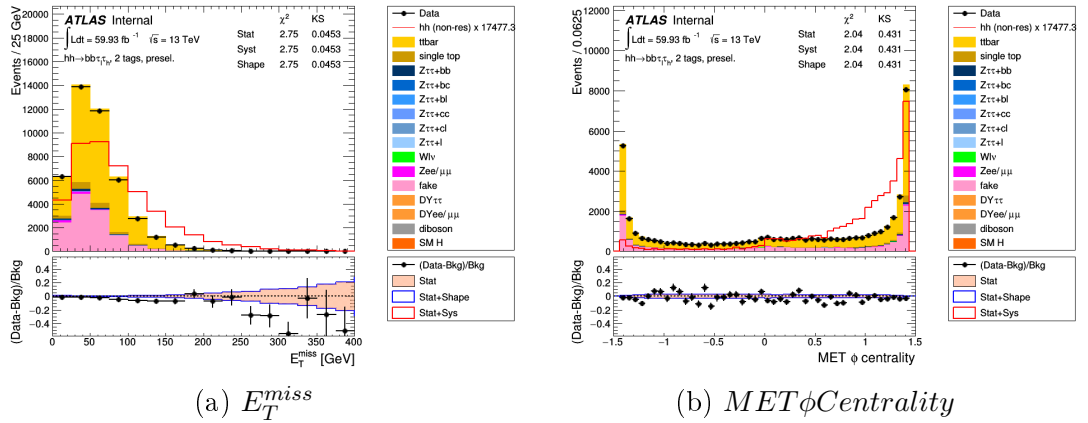


Figure 6.2



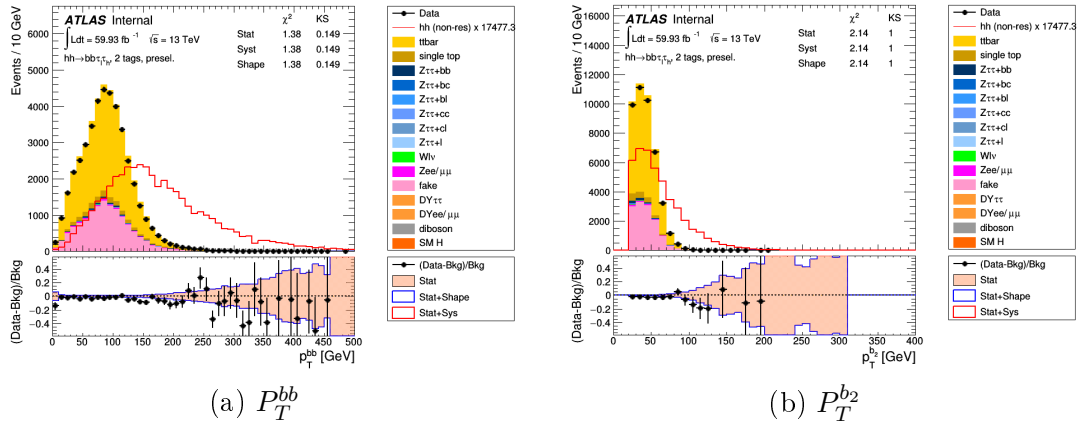


Figure 6.4

sampleName	entries	yield	error	error/integ.
httbb	69587	2.52876	0.0301178	0.0119101
ttbar	222025	28477.4	63.1697	0.00221824
stopWt	11597	1399.19	13.5949	0.00971626
stopt	1329	290.417	8.82223	0.0303778
stops	675	17.6167	0.73025	0.0414522
Zttbb	9413	440.713	13.4813	0.0305896
Zttbc	791	45.8157	5.46603	0.119305
Zttbl	529	25.4653	4.59928	0.18061
Zttcc	253	42.5018	11.0575	0.260165
Zttcl	97	16.8262	4.00884	0.238249
Zttl	56	10.1051	3.51454	0.347799
W	342	39.782	7.4978	0.188472
Wtt	32	2.46033	0.633679	0.257559
Zbb	9304	298.321	12.6811	0.0425083
Zbc	756	29.9669	4.65398	0.155304
Zbl	536	12.7013	4.32276	0.34034
Zcc	160	24.4676	9.64791	0.394313
Zcl	60	5.39211	6.69566	1.24175
Zl	20	16.6661	14.395	0.863731
Fake	392743	12860	105.885	0.00823369
DYtt	6	2.20285	1.74197	0.790782
DY	31	10.0102	3.3707	0.336729
WW	38	5.80914	1.74057	0.299626
WZ	443	26.2249	2.06875	0.0788848
ZZ	2506	37.6086	1.34046	0.0356423
tth	58987	42.95	0.233202	0.00542962
VH	42017	15.2525	0.203158	0.0133197
bkg:	754746	44195.9		
data	43074	43074.0		

Figure 6.5: This table shows about the samples, entries, yield and error for the plots

Chapter 7

Conclusion

In this thesis a search for the Standard Model (SM) Higgs-boson pair production in the $b\bar{b}\tau_{lep}^+\tau_{had}^-$ channel, where one tau-lepton decays leptonically and other tau-lepton decays hadronically, is presented. For this search, I use Monte-Carlo (MC) and DATA samples for the periods of 2016, 2017 and 2018 with integrated luminosity of 137 fb^{-1} at a centre-of-mass energy of 13 TeV.

The di-Higgs production search is performed in the non-resonant decay mode of $b\bar{b}\tau_{lep}\tau_{had}$ channel, and $t\bar{t}$ is used as the major background source. The main challenge is the optimization of signal to background separation for small signals as compared to dominated background. Optimization of signal-to-background is based on their sensitivity of kinematic variables. For this analysis, events are selected for single-lepton trigger.

Machine Learning approaches like TMVA with BDT is used for optimization of signal-to-background. Start training with using m_{hh} , one of the most discriminating variable, as the first variable Perform separate training by adding a second variable and evaluate the significance and Pick the variable that gives the highest significance. Repeat the procedure to select the 3rd, 4th, ... variables. We stop the training when we do not observe significant improve by adding more variables. BDT training is performed to find the kinematic variables with their best sensitivity to discriminate sign-to-background. The combination of our variables on the basis of their sensitivity gives us better significance through the periods. After getting the optimized variables applied on MC and Data samples which gives us better results. By increasing luminosity sensitivity of the variables also increases. At the end, comparison between the sensitivity for MC and DATA samples are plotted. The final results are agreement between the MC and Data samples which shows approximately same behaviour.

Bibliography

- [1] Tom W.B. Kibble.,The Standard Model of Particle Physics, [arXiv:1412.4094v1 \[physics.hist-ph\]](https://arxiv.org/abs/1412.4094v1), **12 Dec 2014** .
- [2] ATLAS Collaboration.,Observation of a new particle in the search for the Standard Model Higgs boson with the ATLAS detector at the LHC, [arXiv:1207.7214v2 \[hep-ex\]](https://arxiv.org/abs/1207.7214v2), **31 Aug 2012** .
- [3] CMS Collaboration.,Observation of a new boson at a mass of 125 GeV with the CMS experiment at the LHC [arXiv:1207.7235v2 \[hep-ex\]](https://arxiv.org/abs/1207.7235v2), **28 Jan 2013** .
- [4] D.Galbraith,UX:Standard Model of the Standard Model, (2012),url:<http://davidgalbraith.org/portfolio/ux-standard-model-of-the-standard-model/>.
- [5] Ellis, John,Higgs Physics, url:<https://cds.cern.ch/record/1638469/files/higgspotential.png>.
- [6] ATLAS, CMS Collaborations.,Combined Measurement of the Higgs Boson Mass in pp Collisions at $\sqrt{s}=7$ and 8 TeV with the ATLAS and CMS Experiments, **Phys. Rev. Lett.** **114** (2015) **191803**, [arXiv:1503.07589v1 \[hep-ex\]](https://arxiv.org/abs/1503.07589v1) .
- [7] ATLAS Collaboration.,Evidence for the spin-0 nature of the Higgs boson using ATLAS data, [arXiv:1307.1432v1 \[hep-ex\]](https://arxiv.org/abs/1307.1432v1), **4 Jul 2013** .
- [8] ATLAS Collaboration.,Measurements of Higgs boson production and couplings in the four-lepton channel in pp collisions at center-of-mass energies of 7 and 8 TeV with the ATLAS detector, **Phys. Rev. D** **91**, **012006**, **16 January 2015**, [arXiv:1408.5191v3 \[hep-ex\]](https://arxiv.org/abs/1408.5191v3), **11 Feb 2015**.
- [9] ATLAS Collaboration.,Measurements of Higgs boson production and couplings in diboson final states with the ATLAS detector at the LHC, [arXiv:1307.1427v2 \[hep-ex\]](https://arxiv.org/abs/1307.1427v2), **24 Oct 2014** .
- [10] ATLAS Collaboration.,Observation and measurement of Higgs boson decays to WW^* with the ATLAS detector, [arXiv:1412.2641v2 \[hep-ex\]](https://arxiv.org/abs/1412.2641v2), **21 Aug 2015**.
- [11] ATLAS Collaboration.,Observation of Higgs boson production in association with a top quark pair at the LHC with the ATLAS detector, [arXiv:1806.00425v2 \[hep-ex\]](https://arxiv.org/abs/1806.00425v2), **14 Aug 2018**.

- [12] ATLAS Collaboration., Observation of $H \rightarrow b\bar{b}$ decays and VH production with the ATLAS detector, [arXiv:1808.08238v2 \[hep-ex\]](https://arxiv.org/abs/1808.08238v2), 29 Sep 2018.
- [13] ATLAS Collaboration., Cross-section measurements of the Higgs boson decaying into a pair of tau-leptons in proton-proton collisions at $\sqrt{s}=13$ TeV with the ATLAS detector, [arXiv:1811.08856v2 \[hep-ex\]](https://arxiv.org/abs/1811.08856v2), 22 May 2019.
- [14] LHC Higgs Cross Section Working Group web page, (2016), url:<https://twiki.cern.ch/twiki/bin/view/LHCPhysics/LHCHXSWG>.
- [15] LHC Higgs Cross Section Working Group, Handbook of LHC Higgs Cross Sections: 4. Deciphering the Nature of the Higgs Sector, CERN Yellow Reports: Monographs (2016), url:<http://cds.cern.ch/record/2227475>.
- [16] Lyndon Evans and Philip Bryant .,LHC Machine, **JINST 3 (2008) S08001**
- .
- [17] G. Aad et al.,The ATLAS Experiment at the CERN Large Hadron Col-
lider,**JINST 3 (2008) S08003** .
- [18] S. Chatrchyan et al., The CMS Experiment at the CERN LHC, **JINST 3 (2008) S08004** .
- [19] K. Aamodt et al., The ALICE experiment at the CERN LHC, **JINST 3 (2008) S08002** .
- [20] A. A. Alves Jr. et al., The LHCb Detector at the LHC, **JINST 3 (2008) S08005** .
- [21] G. Anelli et al., The TOTEM experiment at the CERN Large Hadron Col-
lider, **JINST 3 (2008) S08007** .
- [22] O. Adriani et al., The LHCf detector at the CERN Large Hadron Collider,
JINST 3 (2008) S08006 .
- [23] ATLAS Collaboration., Luminosity Public Results, url:<https://twiki.cern.ch/twiki/bin/view/AtlasPublic/LuminosityPublicResultsRun2>.
- [24] Antonella Del Rosso,HL-LHC updates in Japan, url:<https://cds.cern.ch/record/1975962>.
- [25] ATLAS Collaboration, ATLAS detector and physics performance: Technical Design Report, 1,Technical Design Report ATLAS, CERN, 1999, url:<https://cds.cern.ch/record/391176>.
- [26] J. Pequenao, Computer generated image of the whole ATLAS detector,
url:<https://cds.cern.ch/record/1095924>.
- [27] ATLAS Collaboration, ATLAS magnet system : Technical Design Report, 1,url:<https://cds.cern.ch/record/338080>.
- [28] ATLAS Collaboration, ATLAS inner detector : Technical Design Report, 1,url:<https://cds.cern.ch/record/331063>.

- [29] ATLAS Collaboration,ATLAS inner detector : Technical Design Report, 2 ,url:<https://cds.cern.ch/record/331064>.
- [30] J. Pequenao, Computer generated image of the ATLAS inner detector,url:<https://cds.cern.ch/record/1095926>.
- [31] ATLAS Collaboration,ATLAS calorimeter performance : Technical Design Report,url:<https://cds.cern.ch/record/331059>.
- [32] J. Pequenao, Computer Generated image of the ATLAS calorimeter,url:<https://cds.cern.ch/record/1095927>.
- [33] ATLAS Collaboration,ATLAS muon spectrometer : Technical Design Report,url:<https://cds.cern.ch/record/331068>.
- [34] ATLAS Collaboration,Performance of the ATLAS Trigger System in 2015,url:<https://cds.cern.ch/record/2235584>.
- [35] ATLAS Collaboration.,A search for resonant and non-resonant Higgs boson pair production in the $b\bar{b}\tau^+\tau^-$ decay channel in pp collisions at $\sqrt{s} = 13$ TeV with the ATLAS detector, **arXiv:1808.00336v3 [hep-ex]**, 6 Mar 2019 .
- [36] M. Tanabashi et al.,Review of Particle Physics, 2018, **Phys. Rev. D 98 (2018) 030001** .
- [37] ATLAS Collaboration,Performance of missing transverse momentum reconstruction with the ATLAS detector using proton-proton collisions at $\sqrt{s} = 13$ TeV, **arXiv:1802.08168v2 [hep-ex]**, 13 Dec 2018 .
- [38] P.C. Bhat, Multivariate Analysis Methods in Particle Physics, **Ann.Rev.Nucl.Part.Sci. 61 (2011) 281-309** .
- [39] A. Hoecker et al., TMVA - Toolkit for Multivariate Data Analysis, **arXiv:physics/0703039v5 [physics.data-an]**, 7 Jul 2009 .
- [40] TMVA, <https://root.cern.ch/tmva>